CORE
Metadata, citation and similar papers at core.ac.uk
Provided by ScholarBank@NUS

PHOTOLUMINESCENCE BLUESHIFT MECHANISMS IN MOLECULAR BEAM EPITAXY GROWN DILUTE NITRIDE HETROSTRUCTURES

VIVEK DIXIT

NATIONAL UNIVERSITY OF SINGAPORE

2010

PHOTOLUMINESCENCE BLUESHIFT MECHANISMS IN MOLECULAR BEAM EPITAXY GROWN DILUTE NITRIDE HETROSTRUCTURES

VIVEK DIXIT
B. Tech. (Electrical Engineering)
Indian Institute of Technology, Delhi, 2004

A THESIS SUBMITTED

FOR THE DEGREE OF DOCTOR OF PHILOSOPHY

DEPARTMENT OF ELECTRICAL AND COMPUTER ENGINEERING

NATIONAL UNIVERSITY OF SINGAPORE

2010

ACKNOWLEDGEMENTS

I take this opportunity to extend my heartfelt gratitude to my teachers, friends, and well-wishers who inspired me to pursue PhD and also helped me in this endeavor by direct support, valuable advice, constructive feedback and creating healthy work environment. I have been fortunate to get nice working place, various facilities for doing experiment and simulation, different kind of endeavor in general and permission by providence to successfully complete this work.

First and foremost, I must convey my utmost gratitude to my supervisor, Dr. Xiang Ning, for her support during my research, precious guidance and insightful discussions throughout the entire duration of this work. I would also like to extend my gratitude to Dr. Liu Hongfei for his valuable help in the beginning of this research and thought provoking discussions from time to time. As my mentor, Dr. Xiang Ning, has extended her support in giving me flexibility in choosing a research topic and constructive feedback in improving the quality of research. I also would like to express my heartfelt gratitude for her patience and enabling me to attend overseas conferences.

I would like to extend my gratitude to Mr. Thwin Htoo, Ms. Musni bte Hussain, Mr. Tan Beng Hwee, and Mr. Wan Ninafeng in Centre for Optoelectronics for their support in various administrative procedures and help in using equipments. I would like to thank my other colleagues who I have been working with – Mr. Lim Poh Chong, Ms. Teo Siew Lang, Dr. Soh Chew Beng from Institute of Materials Research and Engineering. I would also like to acknowledge all of my friends and colleagues in Centre for Optoelectronics, in particular, Mr. Mantavya Sinha, Dr. Agam Prakash Vajpeyi, Mr. Huang Leihua, Mr. Tay Chuan Beng, Dr. Lin

Fen, Mr. Maoqing, Ms. Tian Feng, Ms. Yang Jing, Mr. Hu Junhao and Mr. Zhang Shaoliang. I would love to work with them again.

I dedicate this thesis to my beloved teacher and friends whose constant support has motivated and helped me in doing this work. I also thank my parents, other family members and all friends without whose good wishes this thesis wouldn’t have been completed.

TABLE OF CONTENTS

ACKNOWLEDGEMENTS I

TABLE OF CONTENTS III

ABSTRACT VI

LIST OF FIGURES VIII

LIST OF TABLES XIII

ACRONYMS XIV

PUBLICATIONS XVI

CHAPTER 1: INTRODUCTION 1

1.1 DEVELOPMENT OF TELECOMMUNICATION SYSTEMS 2

1.2 TELECOMMUNICATION LASERS AND MATERIALS 7

1.3 DILUTE NITRIDES 11

1.3.1 GaInNAs growth 16

1.3.2 Annealing and Blueshift 23

1.4 OBJECTIVES AND ORGANIZATION OF THESIS 25

CHAPTER 2: EXPERIMENTAL AND THEORETICAL TECHNIQUES 28

2.1 EXPERIMENTAL TECHNIQUES 29

2.1.1 Molecular Beam Epitaxy 29

2.1.2 Reflection High Energy Electron Diffraction 32

2.1.3 X-ray diffraction 34

2.1.4 Photoluminescence 38

2.2 THEORETICAL TECHNIQUES 41

2.2.1 K•P Model 43

2.2.2 Effect of Nitrogen 48

2.2.3 Model solid theory *51*

2.2.4 Finite difference *52*

2.2.5 Optical gain model *56*

CHAPTER 3: INDIUM SEGREGATION IN GAINNAS/GAAS QWS 58

3.1 KINETIC MODELING OF INDIUM SEGREGATION 60

3.1.1 Brief description of experiment *61*

3.1.2 Modified kinetic model *62*

3.1.3 Results and discussion *66*

3.2 EFFECT OF SEGREGATION ON SUBBANDS 73

3.2.1 The structures studied *74*

3.2.2 Muraki model *74*

3.2.3 Segregation effect on strain *75*

3.2.4 Subband energies *77*

3.2.5 Results and Discussion *79*

3.3 CONCLUSION 84

CHAPTER 4: EFFECT OF COMPOSITION DISORDER ON OPTICAL GAIN 86

4.1 QW STRUCTURE 87

4.2 STRAIN AND CARRIER CONFINEMENT PROFILE 88

4.3 BAND DISPERSION 91

4.4 EFFECT OF NITROGEN DISORDER ON TRANSITION ENERGY 92

4.5 OPTICAL GAIN 93

4.6 CONCLUSION 98

CHAPTER 5: THERMAL ANNEALING INDUCED BLUESHIFT 99

5.1 EXPERIMENT 100

5.2 LINEAR MODEL BASED APPROACH 101

5.2.1 Interdiffusion model *101*

5.2.2 Linear model *103*

5.2.3 Results and discussion *104*

5.3 Genetic algorithm based approach 106

5.3.1 Short Range Order *107*

5.3.2 Genetic algorithm *108*

5.3.3 Results and discussion *111*

5.4 Conclusion 115

CHAPTER 6: CONCLUSION AND FUTURE WORK 117

6.1 Conclusions 117

6.2 Suggested future work 118

APPENDIX A: MATERIAL PARAMETERS 120

REFERENCES 121

PHOTOLUMINESCENCE BLUESHIFT MECHANISMS IN MOLECULAR BEAM EPITAXY GROWN DILUTE NITRIDE HETROSTRUCTURES

by

VIVEK DIXIT

SUBMITTED TO THE DEPARTMENT OF ELECTRICAL AND COMPUTER ENGINEERING FOR THE DEGREE OF DOCTOR OF PHILOSOPHY NATIONAL UNIVERSITY OF SINGAPORE

ABSTRACT

Low cost access to optical communication networks is the backbone of modern day optical communication systems for high speed internet data transmission. Cost effective light sources in the low loss window, 1.2-1.6 μm, are required for large scale deployment of high performance communication network systems.

Dilute nitrides have been identified as promising material at 1.3 and 1.55 μm emission wavelengths for commercial applications in telecommunications. They have attracted considerable experimental and theoretical interest due to their unusual physical properties and great potential in optoelectronic devices for telecommunication. They exhibit a large reduction in bandgap energy due to the addition of small amounts of Nitrogen in GaInAs to form GaInNAs. GaInNAs offers several advantages, e.g. type-I band lineup, effective electron confinement, higher electron effective mass and lattice matched (pseudomorphic) growth on GaAs substrate allowing one to take advantage of mature DBR technology and easy monolithic integration with GaAs electronics to provide low-cost, high speed electrical drivers for lasers in high speed networks.

In this work, GaInNAs/GaAs quantum structures are investigated for their structural and optical properties. GaInNAs/GaAs quantum wells (QWs) are grown using plasma assisted molecular beam epitaxy. Theoretical modeling is performed to estimate the effects of Indium segregation,

short range order and interdiffusion on photoluminescence blueshift in GaInNAs/GaAs QWs. A kinetic model is presented to explain the observed Indium segregation trend in GaInNAs due to the incorporation of Nitrogen. Theoretical results are presented for the effect of composition disorder, resulting from Indium segregation and non-uniform Nitrogen composition on band structure and TE and TM mode optical gain of the GaInNAs/GaAs QWs. The presence of composition disorder of Indium and Nitrogen in the quantum wells can cause blueshift in transition energy, but Indium segregation plays the major role. The transition energy blueshift due to Indium segregation is significant only for segregation efficiencies greater than 0.6. Composition disorder also tends to increase the threshold current density for GaInNAs/GaAs QW lasers.

Rapid thermal annealing is performed to improve the optical and crystalline qualities of as-grown GaInNAs material by overcoming crystal defects arising from plasma damage or interstitial incorporation of Nitrogen. The undesirable blueshift resulting from annealing is studied and explained in terms of two responsible mechanisms: rearrangement of local Nitrogen bond configurations $N\text{-}Ga_mIn_{4-m}$ ($0 \leq m \leq 4$), also known as short-range order (SRO), and Gallium/Indium atom interdiffusion across the QW/barrier interface. The individual contributions from both mechanisms are calculated using an original approach based on a genetic algorithm. The activation energies for SRO and interdiffusion are estimated to be 2.3 eV and 3.25 eV respectively, indicating the important role played by SRO at low temperature and at the beginning of annealing process.

Keywords: GaInNAs, Molecular Beam Epitaxy, High resolution X-ray diffraction, Photoluminescence, Rapid thermal annealing, Indium segregation, Interdiffusion, Short-range-order, Genetic algorithm

Thesis Advisors:

1. Asst Professor Dr. Xiang Ning, NUS.

LIST OF FIGURES

Figure 1-1: Wavelength windows in silica based optical fiber (taken from David R. Goff 2002). 3

Figure 1-2: Increasing Bandwidth usage in Japan [http://www.jpix.ad.jp/en/techncal/traffic.html] 6

Figure 1-3: The relationship between bandgap energy and lattice constant for nitride-arsenide and arsenide-phosphide alloys for long wavelength emission (Henini 2005) 9

Figure 2-1: MBE system at the Centre for Optoelectronics. 30

Figure 2-2: 2×4 surface reconstruction RHEED patterns of a (100) GaAs surface: (a) along $[\mathbf{1\bar{1}0}]$, (b) along $[\mathbf{110}]$. 33

Figure 2-3: RHEED intensity oscillation with growth time for GaAs buffer layer growth 34

Figure 2-4: (a) HRXRD system at the Centre for Optoelectronics, (b) Schematic diagram showing the angle and axis conventions. 35

Figure 2-5: Photoluminescence characteristic of GaInNAs/GaAs qunatum well for as-grown and annealed samples. 41

Figure 2-6: For 6-band k•p heavy hole, light hole and spin split-off bands in double degeneracy are of interest and called as class A. All other bands are denoted as class B. 46

Figure 3-1: Schematic structure of samples A, B and C (each with Indium = 33.5%). 62

Figure 3-2: Schematic diagram showing the exchange process between surface and bulk Indium and Gallium atoms. 63

Figure 3-3: Calculated Indium composition profiles at substrate temperature 460 ^{0}C and a growth rate of GaAs 0.57 ML/s. Nominal widths of $Ga_{0.665}In_{0.335}As$ QW and GaAs barrier are 20 ML

and 15 ML, respectively. Segregation length is obtained from decay length at the upper heterointerface as shown in inset. 66

Figure 3-4: Segregation length vs. Nitrogen composition for $Ga_{0.665}In_{0.335}N_yAs_{1-y}$ QW at growth temperature of 460 ^{0}C for calculated (L_C) and experimental deduced (L_{SIMS}) segregation lengths. 67

Figure 3-5: The difference between forward and backward exchange rate constants (R_1-R_2) and the segregation energy (Es) vs. the Nitrogen composition for $Ga_{0.665}In_{0.335}N_yAs_{1-y}$ QW at growth temperature of 460 ^{0}C. 69

Figure 3-6: The equilibrium exchange rate vs. Nitrogen composition curves for $Ga_{0.665}In_{0.335}N_yAs_{1-y}$ QW at various growth temperatures. Two horizontal lines correspond to GaAs growth rate, Vg = 0.57 ML/s and 1 ML/s. 70

Figure 3-7: Nitrogen composition vs. growth temperature showing the kinetically limited and equilibrium regions for $Ga_{0.665}In_{0.335}$NAs QW with GaAs growth rate = 0.57 ML/s. 71

Figure 3-8: Calculated Indium segregation length variation with Nitrogen content in the $Ga_{0.665}In_{0.335}$NAs/GaAs QW for GaAs growth rate (a) growth rate = 0.57 ML/s and (b) growth rate = 1 ML/s, at different growth temperatures. 72

Figure 3-9: Schematic of GaAs/GaInNAs/GaAs QW structures for 1.3 and 1.55 um emission wavelength. 74

Figure 3-10: Effect of compressive and tensile strain on the conduction and valence band-edges. 77

Figure 3-11: Indium segregation profile of $Ga_{0.65}In_{0.35}N_{0.015}As_{0.985}$ / GaAs single QW with different segregation efficiencies. 79

Figure 3-12: In-plane strain profile of $Ga_{0.65}In_{0.35}N_{0.015}As_{0.985}$ / GaAs QW with various Indium segregation efficiencies. 80

Figure 3-13: In-plane strain at the regions close to the QW / barrier interfaces as a function of segregation efficiency. 81

Figure 3-14: Confinement potentials of electrons in the conduction band, heavy holes and light holes in the valence band of the $Ga_{0.65}In_{0.35}N_{0.015}As_{0.985}$ / GaAs QW (λ~1.3 μm) with various segregation efficiencies of Indium atoms. 82

Figure 3-15: Transition energies of e_1-Hh_1 and e_1-Lh_1 in (A) $Ga_{0.65}In_{0.35}N_{0.015}As_{0.985}$ / GaAs and (B) $Ga_{0.61}In_{0.39}N_{0.03}As_{0.97}$ / GaAs QW structures as a function of Indium segregation efficiency. 83

Figure 4-1: Indium and Nitrogen composition profiles for a 7-nm-thick $Ga_{0.59}In_{0.41}N_{0.038}As_{0.962}$/GaAs QW without disorder (structure A, nominal structure with uniform compositions and ideal interfaces) and with disorder (structure B, taken from the experimental results reported in (Luna 2007) with author's permission). 87

Figure 4-2: In-plane strain profiles of a 7-nm-thick $Ga_{0.59}In_{0.41}N_{0.038}As_{0.962}$/GaAs QW for structures A and B. 88

Figure 4-3: Confinement potentials of electrons in the conduction band, heavy holes and light holes in the valence band for structures A and B. 89

Figure 4-4: Confinement potentials of electrons in the conduction band, heavy holes and light holes in the valence band of the $Ga_{0.65}In_{0.35}N_{0.015}As_{0.985}$ / GaAs QW with various segregation efficiencies of Indium atoms without considering Nitrogen disorder. 90

Figure 4-5: Energy dispersion curves for conduction and valence subbands along [100] and [110] crystal directions for structures A and B. 91

Figure 4-6: The increase of electron-heavy hole (C1-HH1) transition energies (blueshift) as a function of Indium segregation efficiency for structures A and B. 93

Figure 4-7: Optical gain spectra of the TE mode of the $Ga_{0.59}In_{0.41}N_{0.038}As_{0.962}/GaAs$ QW as a function of photon energy for structures A and B. 94

Figure 4-8: Optical gain spectra of the TM mode of the $Ga_{0.59}In_{0.41}N_{0.038}As_{0.962}/GaAs$ QW as a function of photon energy for structures A and B. 94

Figure 4-9: Optical gain peak of the TE modes of the $Ga_{0.59}In_{0.41}N_{0.038}As_{0.962}/GaAs$ QW as a function of the injected carrier concentration for structures A and B.. 95

Figure 4-10: Optical gain peak of the TM modes of the $Ga_{0.59}In_{0.41}N_{0.038}As_{0.962}/GaAs$ QW as a function of the injected carrier concentration for structures A and B.. 96

Figure 4-11: Optical gain peak of the TE modes of the $Ga_{0.59}In_{0.41}N_{0.038}As_{0.962}/GaAs$ QW as a function of the radiative current density for structures A and B... 97

Figure 4-12: Optical gain peak of the TM modes of the $Ga_{0.59}In_{0.41}N_{0.038}As_{0.962}/GaAs$ QW as a function of the radiative current density for structures A and B... 97

Figure 5-1: Numerically calculated transition energy between the first confined states of electron and heavy-hole (a) as a function of diffusion length, and (b) as a function of squared-diffusion-length, the solid-line is a linear fitting for the calculated data.. 103

Figure 5-2: Photoluminescence peak energy as a function of annealing time annealed at 680 ^{0}C (a), 700 ^{0}C (b), 750 ^{0}C (c), and 800 ^{0}C (d). The solid lines are the best fittings by using $E_{PL} = \Delta E_{SRO} + E_0 + A \times D\, t$, with E_0 = 0.9145 eV and A = 0.032 eV/nm^2. 104

Figure 5-3: An Arrhenius plot of GaInNAs / GaAs interdiffusion coefficients for temperatures between 680 and 800 ^{0}C. 106

Figure 5-4: Blueshift in transition energy, Ee1-Hh1, of an 8-nm $Ga_{0.628}In_{0.372}N_{0.015}As_{0.985}$ / GaAs QW as a function of diffusion length for different Nitrogen-bonding configurations (N-In_0Ga_4 (□), N-In_1Ga_3 (○), N-In_2Ga_2 (△), N-In_3Ga_1 (▼), and N-In_4Ga_0 (◊)). 108

Figure 5-5: Transition energy, Ee1-Hh1, of an 8-nm $Ga_{0.628}In_{0.372}N_{0.015}As_{0.985}$ / GaAs QW as a function of Nitrogen-bonding configuration. 111

Figure 5-6: Photoluminescence peak energy as a function of annealing time, with annealing performed at (a) 680 ^{0}C, (b) 700 ^{0}C, (c) 750 ^{0}C, and (d) 800 ^{0}C. The solid lines are best fits over calculated transition energies with blueshifts due to interdiffusion (dotted lines) and SRO (dashed lines). 113

Figure 5-7: An Arrhenius plot of GaInNAs/GaAs SRO time constants (τ) for temperature range between 680 – 800 ^{0}C. 115

LIST OF TABLES

Table 1-1: Standardized optical bands for modern day communication 4

Table 1-2: Typical characteristics of different generations of optical fiber transmission systems (Viswanathan 2004) 5

Table 1-3: Problem, cause and solutions of RF-plasma cell in the MBE growth of dilute nitrides 18

Table 2-1: Comparison of 6-band, 8-band and 10-band **k·p** models for dilute nitride material... 49

Table 2-2: General form of the expanded m-band Matrix. Each point in real-space, along the quantized z-axis corresponds to an m-row block in this matrix. 55

Table 5-1: The best fitting values of the diffusion coefficient D and the SRO effect ΔE_{SRO} for the photoluminescence energy blueshifts. 105

Table 5-2: The best fitting values of ΔE_{SRO} and τ for different annealing temperatures............ 114

ACRONYMS

APD	Avalanche photodiode
BEP	Beam equivalent pressure
BS	Blueshift
CBE	Chemical beam epitaxy
DBR	Distributed Bragg Reflector
DC	Direct current
DFB	Distributed feedback (type of laser)
DMHy	Dimethyl hydrazine
DQW	Double QW
DWDM	Dense WDM
EA	Electro absorptive
EEL	Edge emitting laser
FDM	Finite difference method
FP	Fabry perot
FWHM	Full width half maximum
GA	Genetic algorithm
GSMBE	Gas-source MBE
HBT	Heterojunction bipolar transistor
HFET	Heterojunction field effect transistor
HRXRD	High resolution X-ray diffraction
K-cell	Knudsen effusion cell
K·P	k <dot> p model for band structure calculation
LAN	Local area network
LED	Light emitting diode
MAN	Metro area network
MBE	Molecular Beam Epitaxy
MOVPE	Metal organic vapor phase epitaxy
MQW	Multi quantum well
MZ	Mach-zehnder
PL	Photoluminescence
OEIC	Optoelectronic integrated circuits

QW	Quantum well
RF	Radio frequency
RHEED	Reflection high energy electron diffraction
RTA	Rapid thermal annealing
SCL	Strain compensation Layer
SEM	Scanning electron microscopy
SIMS	Secondary ion mass spectroscopy
SL	Superlattice
SRO	Short Range Order
SSMBE	Solid-source MBE
TE	Transverse electric
TEM	Transmission electron microscopy
TM	Transverse magnetic
UHV	Ultra high vacuum
VCSEL	Vertical cavity surface emitting laser
WDM	Wavelength division multiplexing
XRD	X-ray diffraction

PUBLICATIONS

JOURNAL PUBLICATIONS:

1. V. Dixit, H. F. Liu and N. Xiang, “Effect of Composition Disorders on Band Structure and Optical Gain Spectra of GaInNAs/GaAs Quantum Wells,” **Japanese Journal of Applied Physics**, Vol. 48, pp. 081101 (2009).

2. V. Dixit, H. F. Liu and N. Xiang, “Analysing the thermal-annealing-induced photoluminescence blueshifts for GaInNAs/GaAs quantum wells: a genetic algorithm based approach”, **Journal of Physics D: Applied Physics**, Vol. 41, pp. 115103 (2008).

3. V. Dixit, H. F. Liu, and N. Xiang, “Study of thermal-anneal-induced rearrangement of N-bonding configurations in GaInNAs/GaAs quantum well” **Advanced Materials Research**, Vol. 31, pp. 209 (2008).

4. H.F. Liu, V. Dixit and N. Xiang, "Effect of Indium segregation on optical and structural properties of GaInNAs /GaAs quantum wells at emission wavelength of 1.3 micron", **Journal of Applied Physics**, Vol. 100, pp. 083518 (2006).

5. V. Dixit, H. F. Liu and N. Xiang, "Effect of In-segregation on subbands in GaInNAs/GaAs quantum wells emission around 1.3 and 1.55 micron", **Optical and Quantum Electronics**, Vol. 38, pp. 963 (2006).

6. H.F. Liu, V. Dixit and N. Xiang, "Anneal-induced interdiffusion in 1.3-µm GaInNAs/GaAs quantum well structures grown by molecular-beam epitaxy”, **Journal of Applied Physics**, Vol. 99, pp. 013503 (2006).

CONFERENCE PRESENTATIONS:

1. V. Dixit, H. F. Liu and N. Xiang, "Analyzing the Thermal-Annealing-Induced Photoluminescence Blueshifts for GaInNAs/GaAs Quantum Wells capped with dielectric films", **The 5th International conference on materials for advanced technologies (ICMAT2009)** at Singapore, 28 June-3 July 2009.

2. V. Dixit, H. F. Liu and N. Xiang, "Study of Indium Segregation in GaInNAs/GaAs Quantum Wells", **The 5th International conference on materials for advanced technologies (ICMAT2009)** at Singapore, 28 June-3 July 2009.

3. V. Dixit, H. F. Liu and N. Xiang, "Effect of Nitrogen on Indium Segregation in GaInNAs/GaAs Quantum Wells", **IEEE PhotonicsGlobal** at Singapore, 9-11 December 2008.

4. V. Dixit, H. F. Liu and N. Xiang, "Kinetic modeling of Indium Segregation in GaInNAs/GaAs Quantum Wells", invited talk at **Advanced Heterostructures and Nanostructures Workshop (ANHW)** at Hawaii, USA, 7-12 December 2008.

5. V. Dixit, H. F. Liu and N. Xiang, "Optical Gain of Segregated GaInNAs/GaAs Quantum Wells at Emission Wavelength of 1.3 micron," **IEEE International Nanoelectronics Conference (INEC2008)** at Shanghai, China, 24-27 March 2008.

6. V. Dixit, H. F. Liu and N. Xiang, "Study of thermal-anneal-induced rearrangement of N-bonding configurations in GaInNAs/GaAs quantum well", **The 4th International conference on materials for advanced technologies (ICMAT2007)** at Singapore, 1-6 July 2007.

7. V. Dixit, H.F. Liu and N. Xiang, "Effect of In-Segregation on subbands in GaInNAs/GaAs quantum wells for 1.3 and 1.55 micron operation wavelength", **The 6th International conference on numerical simulation of optoelectronic devices (NUSOD-06)** at Singapore, 11 - 14 September 2006.

8. H. F. Liu, D. Vivek and N. Xiang, "Interdiffusion and rearrangement of local Nitrogen bonding configurations in GaInNAs / GaAs quantum wells grown by molecular beam

epitaxy", **The 3rd Asian Conference on Crystal Growth and Crystal Technology (CGCT-3)** at Beijing, China, 16-19 October 2005.

9. N. Xiang, H. F. Liu, J. Kong, V. Dixit and D. Y. Tang, "Dilute nitride semiconductor saturable absorber mirror for modelocking Nd:$Gd_{0.64}Y_{0.36}VO_4$ solid state laser", **The 33rd International Symposium on Compound Semiconductors (ISCS-33)** at Vancouver, Canada, 13-17 August 2006.

10. V. Dixit, H. F. Liu and N. Xiang, "Study of Thermal-Anneal-Induced Rearrangement of N-Bonding Configurations in GaInNAs/GaAs Quantum Wells," **National University of Singapore – National Taiwan University Optoelectronics Student Exchange Workshop** at Singapore, 27 June 2007.

Chapter 1: Introduction

The development of lasers has played a significant role in the journey of fiber-optic communication systems and continues to hold a great potential for its future. III-V compound semiconductors are considered indispensable for their optoelectronic properties and the most suitable candidates for light sources in modern telecommunication industry. GaAs, InP, GaInAsP, GaInAs and GaInNAs are some of the prominent materials used in the fabrication of telecom laser sources. The development of the dilute nitride semiconductor family, during the 1990s, has opened a new opportunity in bandgap engineering capabilities of III-V compound semiconductors. Since the early demonstration of dilute nitride lasers (Kondow 1996), they have been identified as promising material for optoelectronic applications. Dilute nitrides have attracted considerable research interest for their potential emission in strategic wavelength window (1.2-1.6 μm) for telecommunication, unusual physical properties and promising integration with low cost GaAs technology. This chapter explains the importance of dilute nitrides in the big picture of telecommunication systems, constituting components and their performance requirements. The development of telecommunication systems through various technological milestones is described in section 1.1. The role of III-V semiconductors employed as telecom lasers is discussed in the section 1.2. Section 1.3 elucidates the prospects and challenges of dilute nitrides, which is considered a relatively new class of materials. Motivation for this research, research objectives and methodology adopted to meet these goals is described in section 1.4. Section 1.5 summarizes the organization of this thesis.

1.1 Development of telecommunication systems

A reliable long distance communication system is a human necessity and a backbone of modern civilization. Beginning from the early days of long distance communications, using smoke signals and drums, telecommunication systems have developed, through various stages, to modern day ultra-high speed optical communications. As communication systems improved, certain fundamental limitations presented themselves. The invention of the telephone, by Alexander Bell in 1876, was a major breakthrough which led to inter-city communication and formation of telephone exchange centers. The telephone networks used electrical carrier signals and were limited by their small repeater spacing (the distance that a signal can propagate before attenuation requires the signal to be amplified). In December 1901, the invention of wireless communication by Guglielmo Marconi set forth the foundation for first wireless communication between Britain and Newfoundland, earning him the 1909 Nobel Prize in physics. Later developments in wireless communication led to operation in microwave frequency, where bit rate was limited by their carrier frequency.

In the second half of the twentieth century, it was realized that an optical carrier of information would have a significant advantage over the existing electrical and microwave carrier signals. The first problem in using an optical carrier was the lack of a suitable light source. The development of lasers in 1960s helped to overcome the problem of light sources for optical carriers. The second problem was related to the development of high-quality optical fiber to guide the optical signal to travel from source to destination. In 1966 Kao and Hockham proposed optical fibers at Standard Telecommunication Laboratories, when they showed that losses in existing glass were due to contaminants, which could potentially be removed.

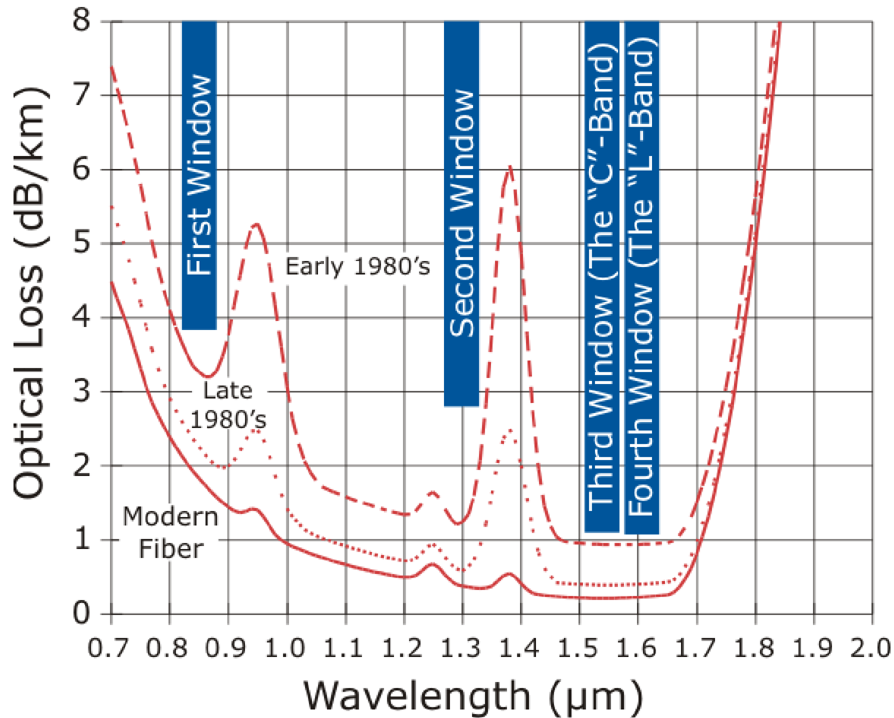

Figure 1-1: Wavelength windows in silica based optical fiber (taken from David R. Goff 2002).

Figure 1-1 shows the wavelength windows of fiber attenuation for commercial silica based optical fiber. The Figure shows the wavelengths, with a local minimum at 0.85, 1.3 and 1.55 μm. In the first window, at 0.85 μm, the losses are high and therefore it is mostly used for short-distance communications. The second window, around 1.3 μm, has much lower losses and corresponds to zero dispersion. The third window, around 1.55 μm, is most widely used due to the lowest attenuation losses, resulting in the ability to achieve the longest transmission range. The fourth window, 1.565-1.625 nm, has been standardized due to the recent advances in optical fibers which effectively extend the third window. A source emission wavelength around 1.55 μm corresponds to a fiber absorption minimum and matches the gain of fiber amplifiers but is limited by undesirable chromatic dispersion (Saleh 1991). Thus the third window requires the use of dispersion compensators. Currently commercial silica based optical fibers, in use for long haul communication, extend the low loss window from 1.26 to 1.68 μm. The wavelength

window favorable for transmission has been standardized for the current technology and is shown in the Table 1-1. As shown in this table, the current technology has bridged the second and third windows (Rüdiger Paschotta 2008). This is due to advanced fibers with low OH content which do not exhibit the peak at 1.4 µm as shown in Figure 1-1.

Table 1-1: Standardized optical bands for modern day communication

Band	Description	Wavelength range
O-band	original	1.26-1.36 µm
E-band	Extended	1.36-1.46 µm
S-band	Short wavelengths	1.46-1.53 µm
C-band	Conventional (Er-window)	1.53-1.565 µm
L-band	Long wavelengths	1.565-1.625 µm
U-band	Ultralong wavelengths	1.625-1.675 µm

The first generation of commercial fiber-optic communication systems came through concurrent development of low attenuation optical fiber and compact GaAs semiconductor lasers. In 1978, the first generation fiber-optic system was commercially deployed. The first generation commercial fiber-optic communication system operated at a wavelength around 0.8 µm with a bit rate of 45 Mb/s with repeater spacing of up to 10 km (Agrawal 1997). In the early 1980s, further development of fiber-optic communication led to use of GaInAsP semiconductor laser as light source for 1.3 µm wavelength. In 1981, the invention of single-mode fiber helped to overcome the limitation due to dispersion to boost system performance. By 1987, these systems were operating at bit rates of up to 1.7 Gb/s with repeater spacing up to 50 km. The development of dispersion-shifted fibers, which were designed to have minimum dispersion at 1.55 micron, eventually allowed fiber-optic systems to be operated at 1.55 µm. These systems had 0.2 dB/km loss for commercial 2.5 Gb/s system with repeater spacing in excess of 100 km. In the year 1988, the first transatlantic optical fiber based telephone cable, TAT-8, came into operation, forming a first undersea 5600 km fiber optic link between the United States and Europe.

Increasing demands of high bandwidth and low cost led to the use of optical amplification and wavelength-division multiplexing (WDM). Optical amplification reduced the need for repeaters and WDM increased the capacity of fiber by allowing data transmission at multiple wavelengths. The generic long-haul dense WDM (DWDM) optical communications system consists of multiple individually modulated sources with slightly different emission wavelengths and optically multiplexed onto a single fiber, which has enabled information transport capacity of 1 Tb/s per fiber in commercial systems. These two developments, since 1992, have revolutionized the telecommunication industry by increasing the system capacity to a bit rate of 10 Tb/s in 2001. Recently, bit-rates of up to 14 Tbit/s have been reached over a single 160 km line using optical amplifiers. The development of fiber-optic communication systems can be divided into various generations, which are summarized in the Table 1-2.

Table 1-2: Typical characteristics of different generations of optical fiber transmission systems (Viswanathan 2004)

Generation	Typical maximum speed distance product (Mbps-km)	Operating wavelength (μm)	Type of fiber	Loss (dB/km)
I	45 150	0.85	Multimode Graded index	3 1
II	500 10,000	1.3	Multimode Graded index	<1 <0.3
III	> 10,000	1.3	Single-mode	< 0.01
IV		1.55	Single-mode	
V		2.0	Infrared fibre	

Through the years 1995-2001, the fiber-optic communication industry became associated with the dot-com bubble and vast increases in demand for communications bandwidth were predicted due to increased use of the Internet and commercialization of various bandwidth-intensive consumer services. The constantly increasing demand of bandwidth and speed of optical networks (e.g., local (LAN), wide (WAN), metro (MAN) and storage (SAN) area

network) for Internet and data transmission is increasing exponentially. The bandwidth usage (in Japan), from year 1999-2009, is shown as an example in Figure 1-2 (Bit rate (Gb/s) vs. Year).

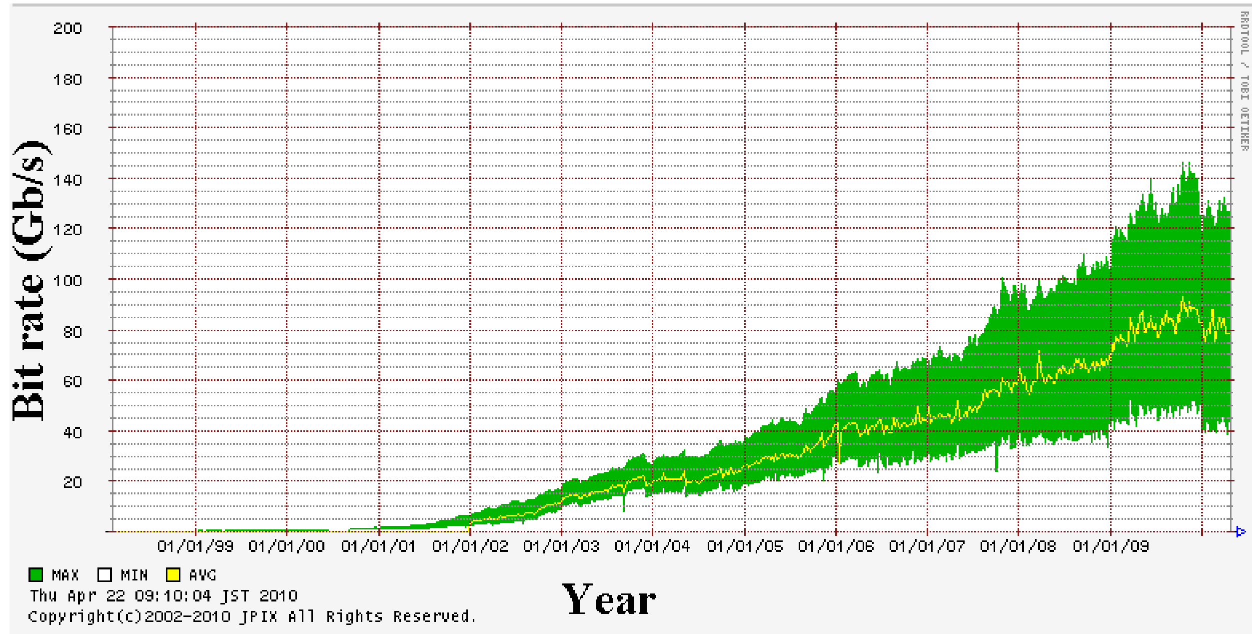

Figure 1-2: Increasing Bandwidth usage in Japan [http://www.jpix.ad.jp/en/techncal/traffic.html]

The performance of an optical network is limited by various issues related to high switching speed, bandwidth requirements and data transmission rate. Recent development of fiber-optic communication focuses on extending the wavelength range over which a WDM system can operate. The conventional wavelength window, known as the C band, covers the wavelength range 1.53-1.57 μm, and the new dry fiber has a low-loss window promising an extension of that range to 1.3-1.6 μm (Huang 2008). The development of cost-effective techniques for laser manufacturing and their integration is essential to fulfill the requirement for high-speed direct access. Therefore it is at the heart of the system to have reliable optical devices at low loss operation wavelength regime. Wavelengths of 1.3 μm and 1.55 μm are particularly important for commercial optical silica fibers as they offer zero dispersion and minimum loss respectively (Gambin 2002).

1.2 Telecommunication lasers and materials

Fiber-optic communication systems consist of four basic entities: (1) a modulated light source, (2) an optical fiber to transmit the modulated light, (3) optical amplifiers to compensate for the attenuation of transmission fiber, and (4) a photoreceiver for conversion of optical to electrical signals (Agrawal 1997). In such systems, source modulation rate, optical fiber length and type, need for optical amplification, and component cost are the prime forces that shape laser source performance requirements, such as laser emission wavelength, modulation rate, wavelength chirp, and temperature sensitivity.

Laser sources are needed for two extremes of telecommunication requirements: long-haul systems and short-reach systems. Long-haul systems are designed for information transportation between major cities with fiber spans typically 100 km to 3000 km and aggregate data rates in the range of l00 Gb/s to 1 Tb/s in a single fiber, which require high performance and high speed laser design. On the other hand, short reach systems are designed for information transmission across a building or an office complex, where focus shifts to lower cost above laser performance. Compared to these two extremes for a metropolitan system, laser cost is still of prime concern but performance requirements are similar to a long-haul system.

Telecom lasers are specialized variants of semiconductor lasers specially adapted to produce powerful, high-speed optical signals that faithfully transmit voice, data, and video signals via optical fiber. The optical system requires additional components such as optical modulators, amplifiers, spot size converters, and detectors to monolithically integrate telecom lasers for enhancing the functionality along with cost reduction. To avoid signal transmission degradation, lasers are designed to produce a single pure output wavelength with minimal

spectral width (Ogawa 1982). The need to transport data at high signaling rates requires rapid laser modulation of the order of 10 Gb/s. To achieve the extremely high data rates demanded by modern optical transmission systems, separate modulators are required (Kaminow and Koch 1997). Signaling at data rates in excess of 40 GB/s is possible using external modulators. For systems employing fiber spans of 200 km and longer an extremely low-frequency chirp is required. This objective is achieved by the use of external modulators such as electro-absorptive (EA) element (Suzuki 1987) or a Mach-Zehnder (MZ) interferometer (Pollock 1995) on a CW-operated laser source. Modulation is achieved through voltage control of the relative phase shift of two recombined signals. EA modulators are smaller and require lower drive voltages than MZ modulators. They lend themselves to monolithic integration, which tends to reduce manufacturing costs. However, MZ modulators provide better modulation characteristics than EA components (for example, chirp control). In practice, both external modulation schemes are employed to meet the various specific needs of long-haul optical communication systems.

Compound semiconductors, especially III-V compounds, are indispensable for the realization of modern optoelectronic devices such as lasers and light emitting diodes (LEDs) used in optical communication systems. They offer potential enhancement to the optical network by offering technically viable options for the devices employed, i.e., lasers, optical amplifiers, repeaters, photodetectors and modulators. However, these structures require heterostructures tailoring for desirable bandgaps and bandedge lineups (also known as "bandstructure engineering") by controlling the composition, thickness and stacking of layers of heterostructure, which is largely dependent on the miscibility of binary III-V constituents and lattice parameters mismatch. GaAs and InP are the two commonly used substrate materials for fabricating heterostructures for optoelectronics applications. Figure 1-3 shows the bandgap energy and

lattice constants of arsenide-nitride and arsenide-phosphide alloys for long wavelength emission. Shaded region below GaAs shows that certain combinations of Indium and N compositions can form a GaInNAs layer which is lattice matched to GaAs.

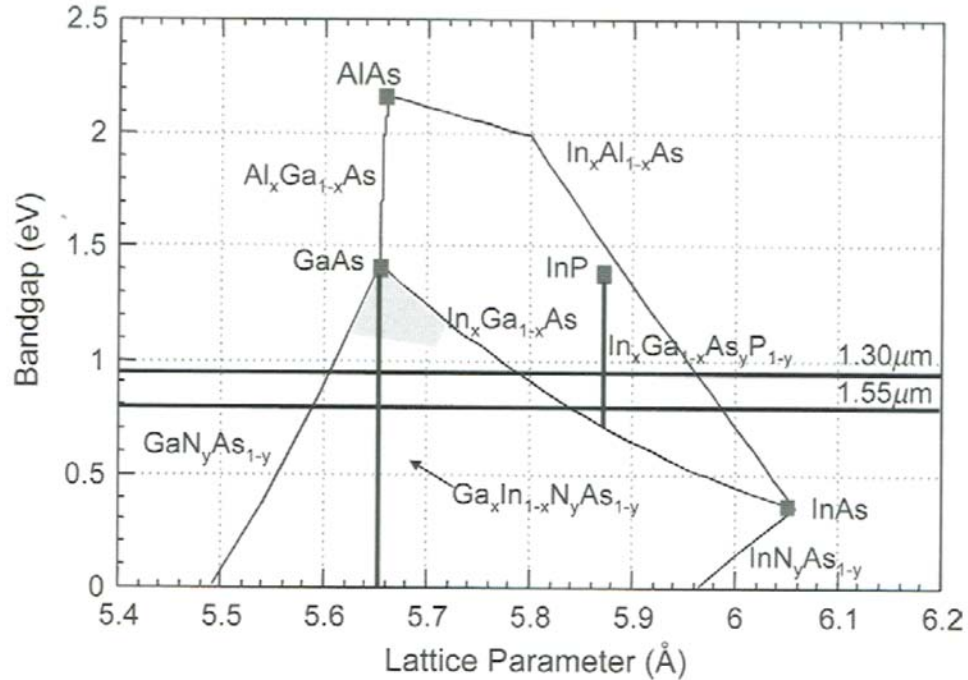

Figure 1-3: The relationship between bandgap energy and lattice constant for nitride-arsenide and arsenide-phosphide alloys for long wavelength emission (Henini 2005)

Currently InP-based uncooled 1.31 μm laser sources can produce more than 20 mW power at 85°C and can be directly modulated at up to 10 Gb/s. The improvements in laser manufacturing technology have brought down the cost even for distributed feedback (DFB) lasers, which makes them popular light sources for short-reach applications. The performance of lasers tends to degrade at high operating temperatures resulting in low output power and poor modulation characteristics (Bhat 1994). Thus it requires careful optimization of the active region quantum well structure. Heat dissipation can be addressed by minimizing device series resistance and employing proper heat sinking. A multi-quantum well structure is usually adopted to increase the optical confinement factor and reduce laser threshold currents at high temperature

(Zory 1993). However, the number of quantum wells is limited by carrier transport problems through the quantum well stack and its ability to support single fundamental optical mode.

Another class of lasers, vertical cavity surface emitting lasers (VCSELs), emits light in a cylindrical beam vertically from the surface of a fabricated wafer, and offer significant advantages when compared to edge-emitting lasers currently used in the majority of fiber optic communications devices. VCSELs can also be manufactured using single step epitaxy. They offer advantages of wavelength-tunability, on wafer testing and possibility of forming multiple wavelength arrays on patterned substrates (Yuen 1997). A VCSEL consists of two oppositely-doped distributed Bragg reflectors (DBR) with a cavity layer in between which consists of an active region with multiple quantum wells. Current is injected into the active region via a current guiding structure. The choice of DBR material is critical for the optimization of VCSEL performance. Using a GaAs substrate, the typical GaAs/AlGaAs DBRs used for commercial 850 nm VCSELs, by adjusting their thickness, can be applied for 1.3-1.6 micron emission. Lateral current confinement can be provided using an oxide aperture or proton implant, both well established for 850 nm VCSELs. Hence, DBR design and VCSEL processing are all proven. The most challenging task is to extend the wavelength of a new active material.

GaAs based systems have shown good performing VCSEL lasers with high speed up to 10 Gbps but only for a small range. GaAs-based devices are very attractive for optoelectronics applications due to cheaper wafer material and mature processing technology as compared to InP-based devices. However, devices based on GaInAs/GaAs material systems can extend device operation wavelength only up to 1.20 μm (Sato 1999). In contrast to GaInAs/GaAs based devices, long-wavelength VCSEL on an InP substrate using conventional InGaAs or InGaAlAs

strained QWs as active region can operate up to 2.1 μm with well understood gain region and minimum reliability concern. However, InP-based devices suffer from poor thermal stability (lowering of efficiency with increase in temperature) and poor refractive index contrast in InP-based DBRs. The commonly adopted solution for poor refractive index contrast is to increase the number of layers for high reflectivity DBR but it results in high series resistance retarding efficient device operation. Various solutions to these problems have been investigated, including wafer fusion of DBR to the active layer (Patriarche 1997), metamorphic growth (Goldstein 1998) and dielectric growth (Uchiyama 1995). However, these solutions complicate the fabrication process, increase cost and may result in unreliable devices (Dudley 1994). Current and optical confinements are also major issues to be resolved to reduce the excessive heat generated at the active junction. Much of the engineering for 1.55-μm VCSEL has focused on these issues. In an attempt to increase the wavelength of conventional GaInAs/GaAs, typical 1.3 micron emission can be obtained with 1.5-2% Nitrogen added into GaInAs with 35-38 % Indium. Since dilute nitrides are the focus of this thesis, their advantages, challenges and development are discussed in the following section.

1.3 Dilute Nitrides

Incorporation of a few percent of Nitrogen as a group V element into GaAs or GaInAs, i.e. by creating the so-called “dilute nitrides”, has been reported as potential candidate to overcome some of the limitations faced by conventional GaInAsP/InP lasers. Initial reports from (Weyers 1992) and (Kondow 1996; Kondow 1996[1]; Kondow 1996[2]) provided early breakthrough in dilute nitrides research for commercial applications in telecommunication. Before Kondow's discovery, it was widely believed that GaInAsP lattice matched to InP was the only alloy series that could meet telecommunications requirements. The discovery that

communication wavelength lasers could be fabricated on GaAs inspired several research groups to initiate work on GaInNAs because of the tremendous processing advantages offered by GaAs over InP.

The incorporation of Nitrogen reduces the bandgap and decreases the lattice constant simultaneously, unlike the addition of Ga, In, P, As, Sb where a reduction (increase) in bandgap energy is achieved by increasing (decreasing) the lattice constant. This behavior of Nitrogen not only reduces the bandgap but also offers opportunity for tailoring band alignments. Both of these effects have opened up a new dimension of bandgap engineering. Initially the incorporation of Nitrogen was thought as unsuitable for alloying as Nitrogen forms a strong perturbation in the GaAs matrix material. Since the last decade, there has been increased interest of researchers in this material due to its many advantages. However Nitrogen-induced defects pose several technical issues which prevent us from exploiting their potential capabilities in telecommunication applications (Buyanova 2004). Potential advantages and recent progress in GaInNAs research has created a wide spread interest in this material; which is indicated by various reviews for this material (Ustinov 2000; Ager 2002). The potential advantages and the limitations of dilute nitrides are listed below.

Advantages

GaInNAs can be closely lattice matched to GaAs and offer a type-1 direct band gap in the range of telecommunications wavelengths (1.25-1.65 μm) making it an attractive alternative for laser materials used in local- and metro-area (LAN, MAN) communications networks. GaInNAs/GaAs heterostructures offer increased conduction band offset as compared with InP-based heterostructures (Knodow 1996), which leads to a more efficient electron confinement,

especially at high temperature. Therefore, the thermal stability of these long wavelength lasers is expected to improve with higher values of characteristic temperature and with a higher maximum operating temperature than common InP-based lasers. The possible high temperature operation can help to remove thermoelectric cooler used to stabilize the laser, thus facilitating low-cost emitters for optical communication and interconnection systems. Moreover, GaInNAs has a larger electron effective mass (Hetterich 2000; Hai 2000). This provides a better match of the valence and conduction band densities of states leading to higher efficiency and higher output power (Knodow 1996).

Compositional control and uniformity of GaInNAs grown by molecular beam epitaxy (MBE) is relatively easy compared to metal organic vapor phase epitaxy (MOVPE) growth or to As/P control in InGaAsP (LaPierre 1996). This will translate into better yield and far easier scale up to larger wafers for lower cost (Henini 2005).

The larger refractive index difference for lattice matched alloys allows GalnAsN active layer to be monolithically combined with high reflectivity GaAs/A1As Bragg mirrors, making this material system attractive for the realization of long wavelength VCSELs. VCSELs can be straightforwardly fabricated using a well-developed GaAs/AlAs mirror and highly selective oxidation of AlAs to form $A1O_x$ for current and optical aperture confinement. The energy band engineering, used to minimize heterojunction voltage drops, use intermediate graded layers of $Al_xGa_{1-x}As$ or A1As/GaAs superlattices. $Al_xGa_{1-x}As$, being lattice matched to GaAs, do not require difficult compositional control over both column III and column V constituents in a quaternary layer, such as GaInAsP, to maintain lattice match (Harris 2002). Thus, GaInNAs on GaAs provides easy monolithic integration with GaAs electronics, which will be essential to

provide low-cost, high-speed integrated electrical drivers for direct laser modulation in high-speed networks. This new development of long wavelength lasers on GaAs substrates can fully take advantage of well-matured GaAs technology and its higher fabrication yield due to the largest size of available GaAs substrates (6-8 inch) as compared with InP (4-6 inch).

The GaInNAs alloy can also be grown on InP substrates in order to extend the emission wavelength range as compared to the conventional GaInAsP alloy. Thus, the whole C- and L-band emission can be covered using tensile strained GaInAsN/(Ga)In(As)P QWs while the emission wavelength range can be further extended far into the infrared, using compressive strained QWs structure (Gokhale 1999; Serries 2002). The use of surfactant Sb to form quinternary GaInNAsSb has shown some benefits in heterointerface quality with respect to GaInNAs and has reached longer wavelengths in MBE-grown QWs (Ha 2002).

Apart from advantages in laser fabrication, GaInNAs material can be used in solar cell applications and electronic devices. The alloy $Ga_{1-x}In_xN_yAs_{1-y}$ is exactly lattice matched to GaAs when y = 0.35x and is required in this form for thick epilayers as the third junction in next-generation solar cells (Friedman 1998). For electronic devices, such as heterojunction bipolar transistors (HBTs) and heterojunction field effect transistors (HFETs), dilute nitrides offer increased design flexibility as a result of greater freedom in band gap engineering and lattice matching (Welty 2004). In terms of lattice-matched structures on silicon, it may be possible to grow optical devices based on GaNAs quantum wells (QWs) in GaP barriers (Kondow 1996[3]). The introduction of InNSb multiple QWs to InSb-based LEDs and detector structures are promising to extend the wavelength of III-V-based emitters and detectors (Johnson 2000; Ashlay 2003).

Limitations

GaInNAs also faces some challenges to utilize its potential. First of all, GaInNAs is a challenging material to grow because the end alloy constituents have different crystal structure: InGaN is wurtzite (hexagonal) and InGaAs is zinc-blende (cubic), which results in a large miscibility gap in the alloys and potential origin of phase separation. The equilibrium solubility of Nitrogen in GaAs is extremely low (Ho 1997). Thus, growing useful material requires that growth be carried out under metastable conditions accessible only to advanced growth techniques such as MBE and MOVPE. Moreover, group V elements have large differences in ionic radii (0.75 Å for Nitrogen as compared to 1.2 Å for Arsenic) and electro-negativities (Phillipsin 1973).

Compositional analysis of this quaternary material is complex especially due to challenging quantitative measurement of Nitrogen content. There have been very few reports of a quaternary composition with no net strain because it is difficult to incorporate sufficient Nitrogen in substitutional lattice sites. Therefore, the dilute nitride epilayer thicknesses employed in dilute nitride devices are limited by critical thickness considerations (Henini 2005).

Although growth by MBE, in comparison to MOVPE, has proven to be easier to fabricate better quality devices suitable over a greater range of wavelengths, there are very significant challenges to achieve good epitaxy and high optical quality material. One of the issues with dilute nitrides is the difficulty associated with the control of the growth parameters to achieve good material quality. MOVPE is the preferred technique for large scale production of optoelectronic devices. The current challenge is a suitable growth technique to choose an

appropriate N-based growth precursor and to optimize specific growth conditions of N-containing alloys.

1.3.1 GaInNAs growth

To overcome limitations due to Nitrogen solubility, GaInNAs is grown under metastable conditions which are achievable only by advanced growth techniques such as solid or gas-source MBE (SSMBE, GSMBE) or MOVPE. MBE and MOVPE can operate far from thermodynamic equilibrium and improve Nitrogen incorporation. The most important improvements in N-containing material quality as well as in laser performance have been mainly obtained by MBE, while MOVPE-grown structures appeared to be a step behind (Illek 2002). There is a large interest to determine if MOVPE, which is currently the mainstream for production of InP-based lasers for telecommunication applications, can also be efficient to grow high performance long wavelength GaInAsN-based lasers. The advances made in the growth of dilute nitrides using MBE and MOVPE growth are described here.

MBE growth of GaInNAs

Nitrogen in normal form is a stable N_2 molecule. The use of Nitrogen, in normal form, during MBE growth leads to a very small incorporation of Nitrogen interstitials in the Ga(In)As matrix. Therefore Nitrogen has to be used in its reactive form such as N-atoms or N* radical. Dissociation energy of Nitrogen molecule, 9.76 eV, is very high as compared with dissociation energies for Arsenic (3.96 eV) and phosphorous (5.03 eV) molecules (Brewer 1996). Nitrogen bond strength happens to be too high for vacuum cracking methods therefore plasma sources

such as direct current (DC) plasma or radio frequency (RF) plasma are used for dilute nitride growth.

During the early development of GaInNAs, RF plasma cells normally used for growing GaN were adapted for the growth of dilute nitride alloys. The RF plasma is preferred over DC plasma because of its low ion count and high atomic dissociation yield (Kirchner 1998), which minimizes the ion or electron damage to the epitaxial films from the plasma source during the growth of dilute nitrides. The main advantage of RF plasma is the generation of atomic Nitrogen, subject to plasma stability. The amount of atomic and excited Nitrogen in the plasma is a function of Nitrogen flow, plasma power, and the numbers and diameter of holes in the plasma source front cover plate (Henini 2005). In any system, plasma conditions are optimized to produce a maximum amount of atomic Nitrogen versus molecular Nitrogen through the emission spectrum of the plasma by comparing the ratio of the integrated intensities of atomic N present in the plasma (Spruytte 2001).

MBE growth using RF plasma sources encounters various problems such as plasma stability, ion or electron damage to epitaxial films and plasma degradation; these necessitate optimizing growth conditions more frequently and lead to differences in growth conditions. The issues related to plasma sources and their solutions are summarized in Table 1-3 (Spruytte 1999; Spruytte 2001[1]; Henini 2005).

Table 1-3: Problem, cause and solutions of RF-plasma cell in the MBE growth of dilute nitrides

Problems	Consequences	Cause of the problem	Solution
Plasma stability: (a) Short term (b) Long term	(1) Difference between wafers grown in the same system (2) Differences in growth under similar conditions	(1) Difficult maintenance of stable flow of injected gas at low flow rates (2) Difficult reproducibility due to thermal and power instability (3) Difficulty in igniting and maintaining consistent plasma over time	(1) Improved RF shielding of matching network and components (2) Minimizing the duration of plasma operation (3) Replace the plasma crucible
Contamination due to Arsenic cell	Cell contamination or coating the outside of the crucible, which reduces RF coupling into the plasma	During growth when the plasma cell is off, the cell is not heated and Arsenic can condense in or on the cell	Gate valve to isolate the cell from the rest of the chamber when N is not needed
Temperature and power to stabilization time	(1) Relatively heavy N "doping" (2) Increased trap density and non-radiative recombination rate	Larger N leakage than for normal evaporative sources	(1) Pre-running cell before the wafer is loaded and growth is started. (2) Better shutter designs (3) Placing the source behind a differentially-pumped gate valve

Incorporation of N into GaAs differs from crystal growth of other III-V semiconductors (such as arsenides, phosphides, or antimonides) as N does not compete for the group-V lattice site. The Arsenic and Phosphorous atoms compete for group-V sites in complex ways depending upon the growth rate and substrate temperature, therefore they requires many calibration samples to know the exact composition obtained during growth. The N incorporation can be controlled by varying flow rate or RF power. However, varying power or flow rate can greatly modify plasma characteristics and change material quality (Yuen 2004). During dilute nitride-arsenide growth, N has been reported to be independent of the Arsenic flux and substrate temperature and shown to have inverse dependence on the group-III growth rate (Spruytte 2001). However, the

mechanism for this dependence is not well known. The N incorporation is also independent of substrate temperature up to temperatures close to normal GaAs growth temperatures of 580^0 C (Yuen 2004[1]). At very high temperatures, phase segregation occurs and the incorporation kinetics is drastically altered.

The non-radiative recombination has been one of the biggest challenges for all dilute nitrides because of the crystal defects arising from low growth temperature and ion induced damage from the use of plasma source. The luminescence properties of GalnNAs deteriorate rapidly with increasing N composition (Spruytte 2001[1]; Harris 2002). The impact of ion or electron damage from the N plasma source on poor luminescence has been reported by several authors (Pan 2001; Li 2001[2]; Wistey 2003). The incorporation of N into Ga(In)As also deteriorates the crystal quality because of the enormous miscibility gap in this material system (Ho 1997). Incorporation of Nitrogen into GaInAs causes various defects such as Nitrogen interstitials, Gallium vacancies, and some other complexes. The possible N configurations in Ga(In)As matrix grown by molecular beam epitaxy (MBE) are: (1) substitutional N_{As} (i.e., replacing Arsenic sublattices with N atoms), (2) a split interstitial N–As complex (i.e., a Nitrogen and an Arsenic atoms on a single Arsenic sublattices site), (3) a split interstitial N–N complex (i.e., two Nitrogen atoms on a single Arsenic sublattices site), and (4) an interstitial isolated N (Li 2001[1]; Fan 2002).

These defects lead to poor material quality and limit the Nitrogen mole fraction of GaInNAs layer. In order to extend the wavelength of this material system, a large Indium composition is needed. For example, about 35% Indium is required in a 7-nm GaInNAs/GaAs QW to reach 1.3 μm emissions. The large Indium composition causes high compressive strain in

the GaInNAs/GaAs QW. Researchers have employed a tensile strained GaNAs layers adjacent to the QW to further extend the wavelength. The insertion of tensile strained GaNAs layer compensates for the compressive strain at the QW/barrier interfaces and thus allows greater Indium incorporation in the QW for larger wavelength (Kitatani 2000; Li 2001; Pavelescu 2002; Liu 2003). However, detailed studies of the GaNAs strain-compensation layer (SCL) effect on the optical and structural properties of GaInNAs/GaAs QW upon annealing show a larger blueshift in the QWs with strain compensated layers. This larger annealing induced blueshift is believed due to the larger vacancy concentration from the GaNAs strain compensation layer (Liu 2006[2]).

The epitaxial growth of GaInNAs based structures with abrupt interfaces and high optical quality is still a challenge. The abrupt interfaces are hindered by Indium segregation and Nitrogen disorder. The incorporation of Indium and Nitrogen is dependent on the growth method employed. For plasma-assisted MBE growth, it is reported that the N incorporation is not affected by Indium content. However, the influence of N on the incorporation of Indium is widely neglected, although strong Indium surface segregation on the growth front has been reported in $Ga_{0.85}In_{0.15}As$/GaAs QWs grown at 460 °C (Martini 2002; Martini 2003), a typical temperature used for the growth of GaInNAs by MBE. This segregation prevents us from obtaining abrupt interfaces leading to asymmetrical composition profile in the QW. The Indium segregation results from the partial incorporation of the Indium in the epilayer, which is believed to result from exchange mechanism of Indium and Gallium atoms during the MBE growth (Dehaese 1995). Segregation phenomenon has been reported in various systems in the past, such as GaInAs, AlGaAs, and InGaP on InP and GaInAs, AlGaAs on GaAs (Muraki 1992). Our research group has reported the Indium segregation in the GaInNAs multi-quantum wells by *in*

situ reflective high-energy electron diffraction (RHEED), *ex situ* secondary-ion-mass spectroscopy (SIMS), and high resolution X-ray diffraction (HRXRD) methods, which reveal that enhanced Indium surface segregation can lead to a suppression of the overall Indium incorporation (Liu 2006[4]). In this dissertation, we have suggested a possible mechanism for enhancement of Indium segregation due to incorporation of Nitrogen.

MOVPE growth of GaInNAs

The MOVPE growth of high quality N-containing III-V alloys is quite complex. It requires very specific growth conditions that are far from the conditions used for conventional GaAs or InP-based semiconductors. To optimize the MOVPE growth conditions for dilute nitrides on GaAs substrates, a general growth strategy is adopted: (i) growth of GaNAs to study the N incorporation in GaAs, (ii) Optimize the growth conditions for highly strained GaInAs/GaAs QW to get the maximum wavelength around 1.2 μm achievable without strain relaxation, and (iii) incorporate the minimum N-content required to achieve 1.3 or 1.55 μm emission. Typical values of Indium and Nitrogen compositions to attain 1.3 μm emissions are around 0.35 and 0.01 respectively. However, the growth control is not straightforward since the GaInNAs alloy, group-III and group-V compositions, as well as the growth rate are dependent on growth temperature and gas phase composition. This complicates the relation between Indium and N in GaInNAs alloys by the selection of metal organic sources (Bhat 1998; Friedman 1998[1]; Zhou 2003).

The MOVPE growth requires an efficient N source with, (i) high vapour pressure (> 10 Torr) at room temperature, (ii) low pyrolysis temperature (< 400 ^{0}C) with good stability at ambient temperature and (iii) excellent purity and safety. The molecules such as Nitrogen (N_2) or

ammonia (NH_3) have a high thermal stability and cannot be used in the case of a low growth temperature regime except using a plasma-cracked gas source (Weyers and Sato 1993). Since a Nitrogen plasma source can be only operated at a very low growth pressure it can not be used in MOVPE. More complex molecules such as unsymmetrical di-methyl-hydrazine (u-DMHy) offer the advantage of a much lower pyrolysis temperature and fit most of the required source specifications. DMHy is a liquid source at room temperature with a sufficient vapour pressure of 130 Torr (Bourret-Courchesne 2000). DMHy has a low dissociation temperature of 420 ^{0}C (Lee 1999) making this N precursor as the most commonly used in epitaxial techniques using all-gaseous sources such as MOVPE and chemical beam epitaxy (CBE). This chemical compound is highly hygroscopic and advanced purification techniques have to be addressed to reduce the water content which has been identified as the major impurity of this precursor (Odera 2000). A new N source, NF_3, has been demonstrated as a more efficient N source as compared with DMHy, resulting in a higher N incorporation in GaAs while using lower N precursor concentration in the gas phase (Ptak 2002). But NF_3 is an oxidizer (contrary to N_2, NH_3 or DMHy), which presents some hazards during its use in a strongly reducing hydrogen-based growth atmosphere that is typical of MOVPE (Kurtz 2002). Due to safety reasons, the commercial use of NF_3 is limited as compared to DMHy.

It is known that metastable layers, without crystal defects in spite of greater lattice strain, beyond the equilibrium critical thickness can be produced at low growth temperature. Therefore, to extend the wavelength, the growth of strained GaInNAs/GaAs QWs is carried out at low temperature, 470-530 ^{0}C (Ougazzaden 1997), as compared with the standard growth temperature for arsenide or phosphides (above 650 ^{0}C). In the low temperature regime N incorporation is controlled only by the fractional flow of DMHy. At higher temperatures the incorporation rate of

Nitrogen decreases due to desorption of volatile N-containing species from the surface, which can be compensated by increasing the V/Ill ratio. The increase in V/III ratio also improves the PL properties of GaInNAs/GaAs QWs by increasing PL intensity and reducing full width half maximum (FWHM), as reported by Asplund *et al.* (Asplund 2000), with a lower thermal sensitivity of the PL emission wavelength on growth temperature. A very rich DMHy gas phase composition is required to attain a long wavelength emission of GaInNAs QWs, which is achieved by increasing the DMHy flow rate as well as by reducing the Arsenic precursor injected flow.

The dependence of N incorporation in GaAs on the growth rate is quite opposite in MOVPE and MBE techniques. As the growth rate is lowered, the N-content decreases in the case of MOVPE-grown layers using DMHy source and it increases for MBE- or CBE-grown alloys using atomic N (Hohnsdorf 1998; Kitani 2000). Such opposite behaviors can be explained by an increased desorption of N-based species from the layer surface in the first case and by a constant N incorporation rate such as a doping element in the second one. The low growth rate is helpful to compensate the reduced surface mobility of N at low temperature and to favor H desorption from the surface.

In this dissertation we study the GaInNAs/GaAs QWs grown using the MBE system. Therefore we will be focusing on the qualities of MBE-grown GaInNAs material.

1.3.2 Annealing and Blueshift

In spite of the advanced growth techniques such as MBE or MOVPE, it is difficult to obtain excellent crystal quality of as-grown dilute nitrides. This is due to III-N-As alloys such as GaInNAs and GaNAs are thermodynamically metastable or unstable. The ion damage from the

use of Nitrogen plasma source also degrades the crystal quality. Post-growth thermal annealing such as rapid thermal annealing (RTA) is effective in improving the crystalline and optical qualities of III-N-As, by overcoming the crystal defects arising from plasma damage or interstitial incorporation of Nitrogen. Thermal annealing supplies the required heat energy to place the atoms to proper lattice sites. Although annealing greatly increases PL intensity it also blueshifts the PL peak wavelength. For example, GaInNAs/GaAs (30% Indium and 1 % N) emitting 1.3 μm wavelength shows about 50 meV blueshift due to annealing, whereas the redshift gained from alloying with Nitrogen is about 150 meV (Kitatani 2000). Since blueshift cancels almost one-third of the redshift gained from the inclusion of Nitrogen, therefore this issue is very significant.

Thermal annealing to improve crystalline quality results in undesirable blueshift and has been extensively reviewed but the causes have not been clearly elucidated. The increase in intensity has been attributed to both the out-diffusion of point defects and an improvement in the crystalline quality of the quantum well material. The wavelength shift is large and could be due to either or both N out-diffusion and Gallium/Indium interdiffusion (Harmand 2000; Riechert 2000; Spruytte 2001[1]; Krispin 2001). The PL blueshift caused by atom interdiffusion is theoretically obtained from the one dimensional Schrödinger equation using a potential derived from Fick's diffusion equation (Chan 2001; Dang 2005; Ng 2005). However, the fitting of the experimental PL blueshift data by just the theoretical $Ee1-\mathrm{Hh1}$ transition (Ng 2005) may overestimate the diffusion, especially for low temperature and short-time duration of annealing, resulting in considerably smaller activation energy of diffusion (0.6 eV) as compared to those of the conventional interdiffusion in GaInAs/GaAs and GaAs/AlGaAs QWs (2.55–3.7 eV) (Gillin 1993; Wee 1997; Li 1998).

Klar *et al.* attributed the thermal anneal induced blueshift to reorganization of N-bonding configuration (Klar 2001). They explained that the rearrangement of Nitrogen-bonding configuration forms five discrete sets of bandgap corresponding to N-In_0Ga_4, N-In_1Ga_3, N-In_2Ga_2, N-In_3Ga_1, and N-In_4Ga_0 phases in GaInNAs. Blueshift is now accepted to be largely due to local atomic reorganization of Nitrogen-bonding configuration, N-In_mGa_{4-m} ($0 \leq m \leq 4$), in short range order (SRO) clusters (Duboz 2002). Similar conclusions were reported by Tournie *et al.*(Tournie 2002), where post-annealing PL measurements from GaInAs and GaAsN did not show any blueshift but from GaInNAs it showed a blueshift of 67 meV. In his experiments, X-ray diffraction (XRD) measurements and transmission electron microscopy (TEM) did not show any compositional change in GaInNAs indicating the reorganization of N-bonding configuration. Liu *et al.* reported that SRO is a dominant mechanism for short time annealing and Gallium/Indium interdiffusion is a dominant mechanism for long time annealing (Liu 2006).

Although there are several reports suggesting various mechanisms for blueshift, such as Gallium/Indium interdiffusion, N-out diffusion, atomic relaxation (Knodow 2004), and SRO there is some consensus over the Gallium/Indium interdiffusion and SRO. However, mostly reports study only one phenomenon and neglect others. Also, there is no study into the time evolution of blueshift due to SRO. In this study we analyze Gallium/Indium interdiffusion and SRO for their individual contribution to the blueshift.

1.4 Objectives and Organization of Thesis

The objective of this research is to understand the structural and optical properties of MBE grown GaInNAs/GaAs QWs and mechanisms responsible for blueshift. The unusual

structural and optical properties arising from the incorporation of small and highly electronegative Nitrogen necessitates the investigation of GaInNAs based heterostructures.

This thesis contains six chapters. The 1st chapter reviews the development of optical communication systems, laser materials and the current development of GaInNAs growth, processing and its application. Chapter 2 describes the experimental and theoretical techniques used in this work. The experimental techniques consist of MBE growth and characterization techniques such as X-ray diffraction, reflection high energy electron diffraction and photoluminescence. The theoretical techniques deal with band structure modeling, specifically the multi-band **k·p** method and computational techniques which were used for modeling and simulating the device characteristics. The work carried out in this study has been divided into three parts consisting of chapters 3, 4 and 5.

Chapter 3 deals with the analysis of the impact of Nitrogen on the structural quality of plasma-assisted MBE grown GaInNAs material. The incorporation of Nitrogen degrades the optical quality of material and therefore we need to understand and optimize the effect of Nitrogen on the growth of dilute nitrides. We have modelled Indium segregation and predict the effect of Nitrogen on Indium segregation. In this chapter we also study the effect of Indium segregation on the band structure and transition energies of the GaInNAs/GaAs quantum wells.

In chapter 4, we investigate the effect of Indium segregation on the optical properties and gain characteristic of GaInNAs/GaAs QWs. Various computational techniques have been employed to understand the effect of composition disorder (non-uniform composition profile of Indium and Nitrogen) on band structure and optical gain properties of GaInNAs/GaAs QWs. In

this chapter, the effect of composition disorder on band dispersion and optical gain is calculated using a 10-band **k·p** model and a many body optical gain model.

Chapter 5 presents analysis of the effect of post-growth annealing on the photoluminescence blueshift. This study is motivated by the fact that as-grown materials tend to show poor photoluminescence properties due to crystalline defects which can be removed by RTA. However, this annealing results in undesirable photoluminescence blueshift. There have been various controversial reports proposing different mechanisms responsible for such blueshift. Here, we apply a novel computational technique to assess the individual contributions of different mechanism towards blueshift.

Chapter 6 concludes the thesis and proposes future work. In this work several computational procedures have been developed using MATLAB, a programming language, to model and study observed phenomena such as Indium segregation and photoluminescence blueshift.

Chapter 2: Experimental and Theoretical Techniques

In this work, GaInNAs-based quantum wells (QWs) were grown by a RIBER 32P III-V molecular beam epitaxy (MBE) system. The GaInNAs quantum wells were grown on a GaAs (100) substrate. Section 2.1 will present the growth and characterization techniques used for the GaInNAs QW samples, including MBE (section 2.1.1), reflection high energy electron diffraction (RHEED) (section 2.1.2), X-ray diffraction (XRD) (section 2.1.3) and photoluminescence (PL) (section 2.1.4). The RHEED technique is used for *in situ* monitoring of the epitaxial film during the MBE growth. The XRD characterization technique is employed to know the composition and thickness of the GaInNAs/GaAs QWs. The PL technique is used to determine the emission properties of the quantum well samples.

The theoretical simulations were used to explain the experimentally measured photoluminescence characteristics of the as-grown QWs and the origin of blueshift resulting from post-growth annealing. Various phenomena such as Indium segregation (appearance of non-abrupt QW/barrier interfaces), interdiffusion and atomic rearrangements were considered in the theoretical modeling to explain the observed photoluminescence characteristics. The bandstructure and transition energy calculations, for the structures studied, were performed using the multiband **k•p** model. Section 2.2 will describe the theoretical techniques used in the bandstructure and optical gain calculation of the dilute nitride QWs, including the **k•p** bandstructure (section 2.2.1). The effect of Nitrogen is described in section 2.2.2. This section explains that conventional 6-band and 8-band **k•p** models are inadequate to explain the strong

bandgap bowing in GaInNAs. Thus, band-anticrossing and 10-band **k•p** model should be used. The detailed description of 10-band **k•p** model is also presented therein. Section 2.2.3 explains the use of model solid theory to calculate the band edges, which is particularly useful at interfaces. In the section 2.2.4, finite difference (FD) method is explained, which is used to calculate bandstructure by solving the 10-band **k•p** model. Finally, section 2.2.5 explains the many-body optical gain model to calculate the optical gain spectrum of the QW structures.

2.1 Experimental Techniques

2.1.1 Molecular Beam Epitaxy

The MBE growth is highly precise and widely employed crystal growth technique, which was developed in early 1970s as a means of growing high-purity epitaxial layers of compound semiconductors. MBE is an ultra high vacuum (UHV) deposition technique evolved from a surface study tool, allows controlling the thickness up to few Angstroms (Bell 1994). Advances in MBE technology have lead to a new era of growth concepts and device technologies, such as bandgap engineering, quantum size structures, quantum phenomena, delta doping, superlattices and strained layer structures. Nowadays MBE is not confined to research field but has got a wide use in industries as well.

MBE growth of epitaxial structures is carried out in an ultra-high vacuum chamber on a substrate heated to an elevated temperature. In a solid source MBE system (Cho 1979), the constituents of growth material are evaporated by the appropriate solid sources in effusion cells. Ultra pure elemental sources are used in the effusion cells to maintain high purity of the epitaxial layer. Effusion beam fluxes are controlled by the temperature of the sources in the Knudsen

effusion cells (K-cells) to control the constituent elemental composition or carrier doping level in the layer grown.

We use a RIBER 32P III-V solid-source molecular-beam epitaxy (SSMBE) system for epitaxial growth. The RIBER 32P III-V SSMBE has a modular configuration, i.e. growth chamber, sample exchange load-lock and loading chamber. These three chambers in the MBE system are connected by a UHV transfer tube. A base pressure of 10^{-10} Torr is maintained by using an ion pump and a cryogenic helium closed cycle pump as well as a liquid Nitrogen-cooled shroud. Figure 2-1 shows the picture of MBE at the Centre for Optoelectronics.

Figure 2-1: MBE system at the Centre for Optoelectronics.

The growth chamber has eight ports, with Ga, In, Al, Be, Si K-cells sources, Arsenic (As) cracker source, and Nitrogen RF plasma source. The As-cracker provides good controllability and reproducibility of the flux in controlling the Arsenic composition (Miller 1990). Similarly, the RF-Nitrogen source offers better incorporation of Nitrogen due to a low ion count and a high atomic dissociation yield (Kirchner 1998). The substrate is placed in a special holder, which

faces the K-cells. There is a heater behind the holder to control the temperature for epitaxial growth. The growth temperature is monitored by a thermocouple. The MBE system is equipped with a RHEED apparatus, quadrupole mass spectrometer for leak detection, and a movable ion gauge. A computer remote control is also available to automate the complex growth procedures. This system was used to grow dilute nitride QWs.

The ion gauge used in the growth chamber is essentially a density monitor, the relative average velocities of each species must be taken into account when comparing beam equivalent pressure (BEP), and the relative fluxes may be calculated from the relative BEP according to (Parker 1985)

$$\left(J_x/J_y\right) = \left(P_x/P_y\right)\left(\eta_y/\eta_x\right)\left[\frac{T_x/M_x}{T_y/M_y}\right]^{1/2} \quad (2\text{-}1)$$

where J_x, P_x, T_x and M_x denote flux, BEP, absolute temperature and molecular weight for species X, respectively. η is the ionization efficiency relative to Nitrogen and is given by

$$\left(\eta/\eta_{N_2}\right) = (0.4\,Z/14) + 0.6 \quad (2\text{-}2)$$

where Z is the atomic number (Williams 1985). By substituting these parameters the flux ratios can be measured for species like Gallium, Indium etc.

Sample preparation

A clean substrate surface is an important prerequisite for epitaxial growth, since contaminants from the atmosphere or other sources can be easily introduced leading to crystal defects or degradation of the optical and electrical characteristics of the epitaxial layer.

The substrate holders made of molybdenum do not decompose or outgas impurities even when heated to 1400°C, thus avoiding contamination. Normally substrates require cleaning before MBE growth. However, we use commercial epiready GaAs (100) substrates, which can directly be loaded into the MBE loading chamber without any chemical cleaning. The chamber is pumped down to ~10^{-6} Torr after the substrate is loaded. In order to get rid of water molecules or particulate contaminants the substrate is heated to 300°C for at least 30 minutes in the loading chamber before it is transferred to the growth chamber.

GaAs has a native oxide layer on the surface. After the GaAs substrate is transferred into the growth chamber, the chamber is pumped down to 10^{-9} Torr and the substrate is heated to about 620 ^{0}C under the Arsenic overpressure. This desorbs the oxide and makes the surface atomically clean. Substrate quality is measured by RHEED with the electron beam focused at a low angle to the substrate surface. We also grow a buffer GaAs layer (at 580^{0}C) before the heterostructure. In the heterostructure, dilute nitride films are grown at low temperature (460^{0}C) to improve the incorporation of Nitrogen and provide suitable growth conditions.

2.1.2 Reflection High Energy Electron Diffraction

A reflection high energy electron diffraction (RHEED) apparatus is used for *in situ* monitoring of epitaxial film quality, to know the surface cleanliness and surface reconstruction. It is also used to measure the growth rate of the film. Surface quality can be determined from RHEED pattern; a clean surface shows a streaky profile whereas surface with roughness shows a spotty pattern. RHEED uses high energy electron beam in the range of 5-40 KeV with incidence angle at 1-2 degree to the substrate surface, with diffraction pattern forming on the screen opposite to source side (Cho 1983). This lower incidence angle makes it surface sensitive.

During the growth of the GaAs layer we can observe the surface reconstruction patterns to know the status of our growth. Surface reconstruction changes with the Arsenic overpressure. Under optimum GaAs growth conditions the surface shows Arsenic terminated (2×4) reconstruction. Figure 2-2 shows the (2×4) surface reconstruction pattern during the growth of GaAs buffer layer. If we decrease Arsenic overpressure it shifts to (4×2) reconstructed surface.

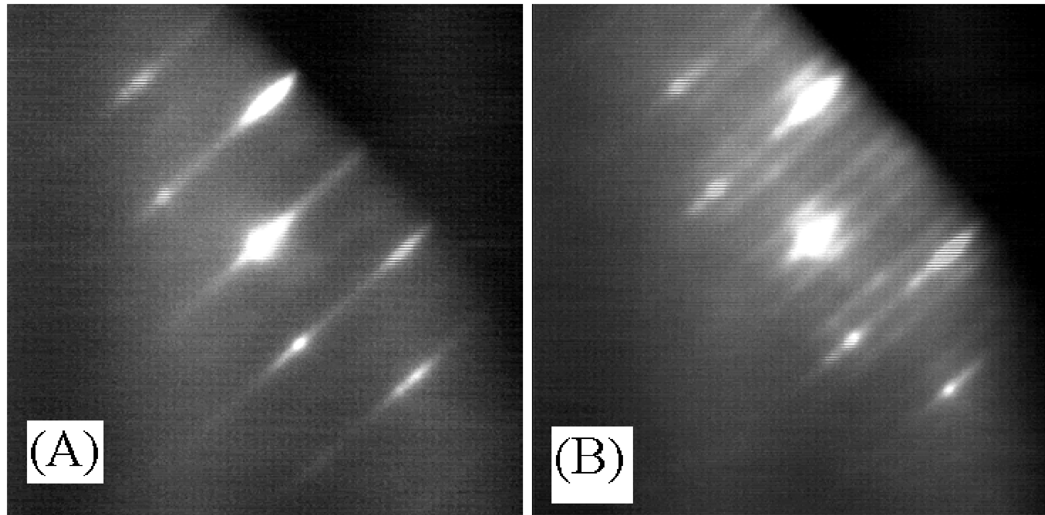

Figure 2-2: 2×4 surface reconstruction RHEED patterns of a (100) GaAs surface: (a) along $[1\bar{1}0]$, (b) along $[110]$.

RHEED intensity oscillation with time can be used to determine the growth rate. Figure 2-3 shows the change in RHEED intensity during the growth of GaAs buffer layer. The RHEED intensity pattern completes one cycle with the completion of every monolayer (ML) due to the change in surface coverage. On the layer with increasing surface coverage, the intensity drops from maximum to minimum till half surface coverage; then the intensities again increases to maximum until full surface coverage. We can get such a cycle to keep repeating for every monolayer. From the RHEED oscillation intensity plot, we can determine the GaAs growth rate. Figure 2-3, for example, shows that it takes about 14 seconds to complete 11 monolayers, so growth rate ≈ 0.8 ML/s.

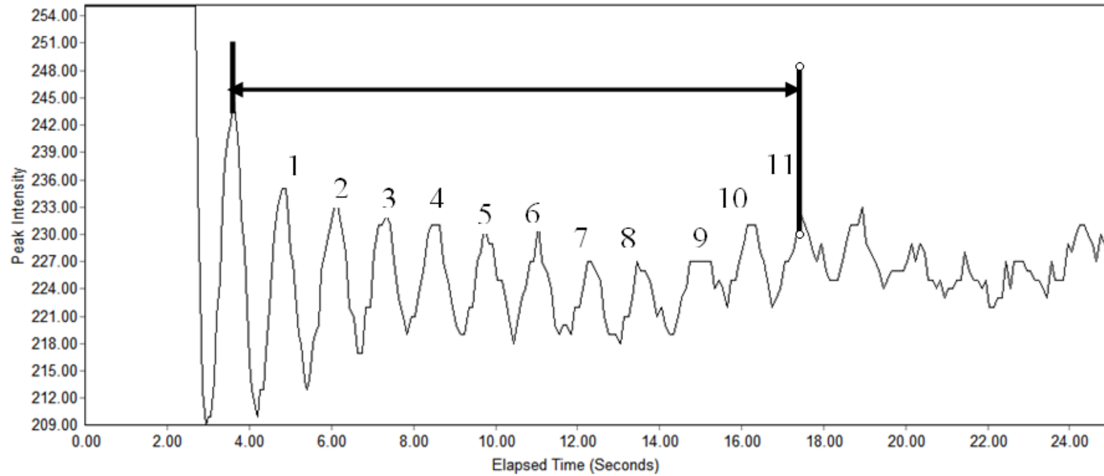

Figure 2-3: RHEED intensity oscillation with growth time for GaAs buffer layer growth

2.1.3 X-ray diffraction

High resolution X-ray diffraction (HRXRD) is a quick and non-destructive analysis tool for epitaxial films. HRXRD analyses have been widely applied for the structural characterization of various strained material systems. The information is obtained from the diffraction pattern resulting from constructive interference. Diffraction patterns of hetroepitaxial structures contain information about their compositions and uniformities, their thicknesses, and the built-in strain and strain relaxation. For a full interpretation, simulations based on dynamical scattering theory have to be used (Ryang Wie 1994). The diffraction peak is determined by the Bragg law expressed as follows

$$n\lambda = 2d_{hkl} \sin\theta \quad (2\text{-}3)$$

where λ is the wavelength of the X-ray, θ is the scattering angle for the nth order diffraction pattern, and d_{hkl} is the spacing between (hkl) planes. For a cubic crystal with lattice constant of a, the spacing between (hkl) planes d_{hkl}, is given by

$$(1/d_{hkl}^2) = (h^2 + k^2 + l^2)/a^2 \quad (2\text{-}4)$$

The XRD system used in this study is a Philips X'Pert MRD-high resolution double crystal X-ray diffractometer. Figure 2-4 shows the double crystal XRD system (a) and schematic diagram of axis and angle convention for XRD measurements (b). In Figure 2-4 (b), Ω is the angle between the incoming X-ray from the source and the substrate plane, 2Θ is the angle between the extended line of incoming X-ray source and the diffracted X-ray, Φ is rotation angle around the surface normal of the substrate, and Ψ is the rotation angle about X-axis. Rocking curve measurements are done by rocking the sample about the Bragg angle and changing the source and detector angle with respect to the sample surface.

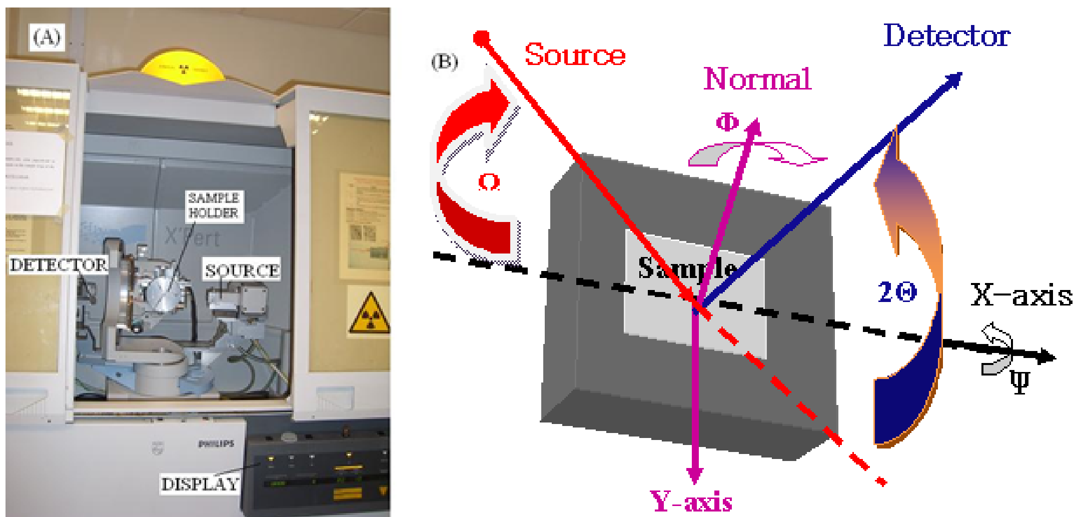

Figure 2-4: (a) HRXRD system at the Centre for Optoelectronics, (b) Schematic diagram showing the angle and axis conventions.

For GaAs (001)-based structures, a rocking curve (Ω-2Θ) scan along (004) plane is the most useful and quite commonly performed X-ray diffraction measurement. The layered structure results in different peaks for different lattice mismatches. The crystal quality can be easily determined by studying the diffraction peaks. A narrow peak indicates good crystal quality. The broadening of peaks occurs mainly due to intrinsic full width half maximum

(FWHM) of crystal, monochromator convolution, sample curvature and defect arising from poor crystal quality.

For a sample with single hetroepitaxial layer, the layer thickness can be determined from the Pendellösung fringe spacing. The peak separation between substrate and layer is given by, $\Delta\Theta = \Delta\theta_B + \Delta\Phi \pm \Omega s$, where $\Delta\theta_B = -\left(\frac{\Delta d}{d}\right)\tan\theta_B = -(\varepsilon_{\|}\sin 2\Phi + \varepsilon_{\perp}\cos 2\Phi)\tan\theta_B$ is due to the difference in lattice d_{hkl} spacing, $\Delta\Phi = -(\varepsilon_{\perp} - \varepsilon_{\|})\sin\Phi\cos\Phi$ is due to difference in the [hkl] directions, and Ωs is the differences in surface orientations. Here, θ_B is the bragg angle, $\varepsilon_{\|}$ is the in-plane strain, and $\varepsilon_{\perp}$ is the out of plane strain.

However if the lattice plane is parallel to the sample surface (Φ=0) or epilayer is fully strain relaxed ($\varepsilon_{\perp} = \varepsilon_{\|}$) then ΔΦ=0. The difference between substrate and epilayer surface orientation, Ωs, arises during growth due to particular arrangement of arriving atoms to minimize surface energy. Perpendicular mismatch can be found from two symmetric reflections $\varepsilon_{\perp} = -average(\Delta\theta)\cot\theta_B$.

Parallel mismatch can be found from two asymmetric reflections such as 115, 224 or 333. From the perpendicular mismatch and the two in-plane mismatches we can find the misfit between cubic cells by $\varepsilon_f = [\nu\varepsilon_{||}[110] + \nu\varepsilon_{||}[\bar{1}10] + (1-\nu)\varepsilon_{\perp}]/(1+\nu)$, where ν is the Poisson ratio of the epilayer. From this we can get ternary layer composition by using Vegard's law (Vegard 1921). This is accurate for lattice matched layers or pseudomorphically grown layers, i.e., ($\varepsilon_{\|} = 0$). However as in-plane strain increase there is significant deviation due to partial strain relaxation. This effect is known as the Fewster-Curling-Wie effect. The shifting of the Bragg peak separation due to the interference effect for a very thin, lattice matched

hetroepitaxial layer is found to be dependent on the product of the layer thickness and the lattice mismatch. However, peak shifting is found to be independent of sample crystal, X-ray wavelength, and the lattice plane (hkl).Therefore in this case we can not use simple peak separation but dynamical theory which accounts for the interference effect.

Similar analysis can be applied to superlattices (SLs) and multiple quantum wells (MQW), the period thickness can be found from the spacing of principle interference fringe peaks. Fringe peaks follows a periodic trend of fringe pattern. The Nth order SL peaks occur at $\phi_p=n\pi$. The SL periodicity p is determined from angular spacing (δθ) of principle SL peaks, by $p=(|\gamma_k|\lambda)/(\delta\theta\sin 2\theta_B)$, where, $|\gamma_h| = \sin(\theta_B+\phi)$, ϕ is the angle between the sample surface and the lattice plane (hkl), δθ is the peak separation and θ_B is the Bragg angle. The principle SL peaks are the thickness fringes corresponding to one period of MQW. In between the two neighboring principle peaks there are N-2 secondary peaks, which are thickness fringes corresponding to the total SL thickness. There, 0th order satellite is related to the average lattice parameter of the MQW period, .i.e., average content

$$\langle x\rangle = \left(x_w L_w/(L_w + L_b)\right) \tag{2-5}$$

If layer thicknesses are in the ratio of m: n (both integer) then every $(m+n)^{th}$ SL peak intensity will be zero.

Any interface present also affects the angular position of the zero order SL peak and the envelop function profile. The angular split, T, between any pair of satellites is due to the total thickness of the MQW. The split T_p between adjacent main (more intense) satellites arises from the period thickness, L_p.

Sometimes asymmetric broadening of the substrate peak is observed, which is due to the tensile strained GaAs layer capping the MQW/SL. However, relaxed superlattice in relation to substrate leads to wide satellites and to the absence of thickness fringes. The in-plane relaxation, R, can be determined by comparing the position of the 0th order harmonic in symmetric and asymmetric reflections, $R = \frac{a_{\|} - a_s}{a_L - a_{\|}}$, where $a_{\|}$ is the in-plane lattice parameter of the well-layer, a_s is the substrate lattice parameter and a_L is the bulk lattice parameter of the well-layer. Analysis performed with XRD can also be compared with other measurements such as secondary mass spectroscopy (SIMS).

XRD analysis of a quaternary material system (GaInAsN) is more difficult. To analyze composition and thickness, we need to have a ternary material (GaInAs) grown under the same conditions to characterize a quaternary material. In the case of GaAs, if we add Indium (Nitrogen) lattice constant will increase (decrease) but wavelength will increase due to band gap narrowing. So, unique characterization will necessitate having another ternary sample GaInAs grown under the same conditions.

2.1.4 Photoluminescence

Photoluminescence (PL) is a widely employed nondestructive optical characterization technique for understanding various dynamical processes in semiconductors. Dilute nitrides are direct band gap semiconductors, thus a PL spectrum is extremely useful in studying their optical properties. When photons of higher energy are used to optically excite a smaller band gap semiconductor conductor ($h\nu > E_g$), it results in the excitation of electrons from the valence band to the conduction band generating a non-equilibrium concentration of holes and electrons. An

optically excited semiconductor generates photons resulting from electron-hole pair recombination. This process is termed photoluminescence, i.e., radiative recombination of electron-hole pairs from an optically excited semiconductor. The quality of PL depends on the amount of radiative recombination compared to non-radiative recombination. Directional and surface state dependence may cause the actual PL intensity to decrease. Accounting for various such processes, PL intensity Φ_{PL} has been reported to follow the following expression (Hovel 1992)

$$\Phi_{PL} = (\Phi(1-R)cos\theta/\pi n(n+1)^2)(L/\tau_{rad}\, s_\tau) \quad (2\text{-}6)$$

where Φ is the incident photon flux density, R is the reflectivity, θ is the emission angle, n is the refractive index, L is the minority carrier diffusion length, τ_{rad} is the radiative life time, and s_τ is the surface recombination velocity. This equation shows the inverse dependence of PL intensity with surface recombination.

Radiative recombinations have been classified into five most commonly observed radiative recombination mechanisms (Tajima 1997) i.e., (a) band to band recombination or free carrier recombination, (b) free exciton recombination, (c) bound exciton recombination, (d) free-to-bound recombination, and (e) donor-acceptor-pair (DAP) recombination.

Band to band recombination is dominant at room temperature but shows weak characteristic (due to exciton recombination being dominant) at low temperature particularly for material with small effective masses due to large electron orbital radii. When a free electron and hole bound together via Coulombic attraction they form a free exciton. Coulombic attraction results in exciton binding energy which reduces the photon energy of free exciton recombination

slightly less than free carrier recombination. Sometimes an exciton may become bound at impurities (donors or accepters). They give rise to sub bandgap radiation i.e. donor to valence band or conduction band to acceptor. They show smaller photon energy than the bandgap. The transition from donor level to acceptor level is sensitive to the spatial arrangement of the donor and acceptor impurity pair, i.e.,

$$h\nu = E_g - (E_A + E_D) - (q^2/\varepsilon_r \varepsilon_0 r) \quad (2\text{-}7)$$

where E_g is the bandgap energy, E_A is the acceptor energy level, E_D is the donor energy level, q is the charge of the impurity pair with separation r, and $\varepsilon_0\varepsilon_r$ is the permittivity of the material. Photoluminescence spectroscopy is a useful technique to determine various properties of an optically active semiconductor. PL can be used to determine bandgap and recombination mechanism of any unknown semiconductor. The free carrier recombination between conduction band and valence band corresponds to bandgap of the semiconductor. The PL intensity profile due to free carrier recombination shows asymmetry towards high energy side. Different types of recombination mechanisms show a characteristic dependence of PL intensity (I) on excitation power (P). Exciton recombination follows a linear dependence of PL intensity over excitation power, i.e., $I \propto P^1$ and for free carrier recombination it follows a square dependence, i.e., $I \propto P^2$, whereas for other type of recombination it shows a power between 1 and 2.

Nonradiative centers degrade optical quality of the crystal. These nonradiative centers widen the FWHM of the PL spectrum. Thus, the FWHM of the PL emission spectrum gives an indication of material quality. Figure 2-5, for example, shows the PL curves for a typical GaInNAs/GaAs QW sample. As we can see that the PL curve for an as-grown sample has smaller intensity and larger FWHM, whereas the annealed sample has a better PL characteristic.

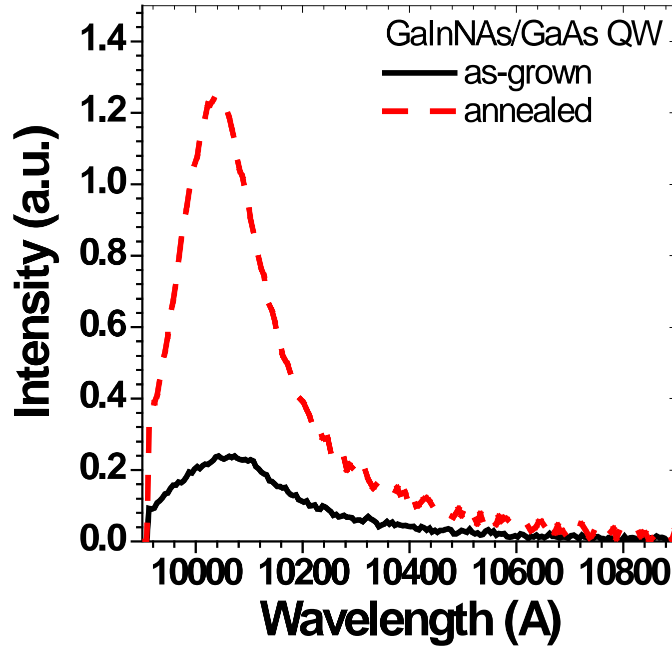

Figure 2-5: Photoluminescence characteristic of GaInNAs/GaAs qunatum well for as-grown and annealed samples.

PL emission energy is affected by the change in crystal symmetry resulting from strain effects in the crystal. Strain splits the degeneracy of the valence band and increases PL emission energy in case of compressive strain and vice versa in case of tensile strain. The shift in PL emission energy (ΔE) tells us about the nature and amount of strain (σ), i.e., $\Delta E = \sigma$ k. where k is the strain coefficient.

2.2 Theoretical Techniques

During the growth and post-growth annealing of GaInNAs/GaAs QWs, issues such as Indium segregation and photoluminescence blueshift were identified. In order to understand the optical properties, such as absorption or gain due to electronic transitions in the presence of an optical wave, we have to know the bandstructure, including energy band and the corresponding wave functions. There are several models for calculating the energy band structure of semiconductors, e.g., multiband **k•p** (Bardeen 1938; Seitz 1940), empirical tight-binding (Slater

1954), and pseudopotential (Phillips 1959) models. Multiband **k•p** is the most straightforward and widely used model for calculating energy bandgap and dispersion for direct bandgap semiconductors near the Brillouin zone center in the effective mass approximation. The generalized multiband **k•p** model includes the effects of strain through the Pikus-Bir Hamiltonian (Pikus 1974). Conventionally a 6-band **k•p** model is used for calculating the valence band structure where coupling with the conduction band is negligible. The 8-band **k•p** model takes into account the coupling between the conduction and valence band and is therefore useful for narrow bandgap semiconductors. Section 2.2.1 describes the governing theory of the **k•p** model.

For GaAs, a 6-band **k•p** model is sufficient for bandstructure calculation as the conduction band and valence band at Γ valley are decoupled. Inclusion of Indium reduces the bandgap and thus for higher Indium compositions an 8-band **k•p** model is used. Dilute nitride, GaInNAs, consists of a GaInAs host material with a small amount of Nitrogen resulting in a large bandgap bowing. Nitrogen is a small and highly electronegative element which forms an impurity band in the host structure. The interaction of Nitrogen with the host bandstructure is described using a band-anticrossing model. The band anticrossing effect is combined with the 8-band **k•p** model, by adding two extra bands corresponding to the N-band, forming the 10-band Hamiltonian **k•p** model. Section 2.2.2 describes the effect of Nitrogen on bandstructure using band anticrossing model along with the description of the 10-band **k•p** model. Section 2.2.3 describes the model solid theory as used in calculating the band edges especially at the interface of the heterostructures. Section 2.2.4 describes the finite difference method that is employed in solving the Schrödinger equation under an envelop function scheme. Finally, section 2.2.5

explains the many-body optical gain model which is used for calculating the optical gain spectrum of the GaInNAs QWs.

2.2.1 K•P Model

Multiband $\mathbf{k \cdot p}$ is based upon time-independent perturbation theory. This method is particularly useful for analyzing the band structure near a particular wave vector ($\mathbf{k}_0$), especially when it is near an extremum of the band structure. The energy is calculated near a band extremum by considering the wave number (measured from the extremum) as a perturbation. This method is most reliable in the vicinity of conduction band and valence band edges ($\boldsymbol{k}_0 =0$ for most III-V direct bandgap semiconductors) which govern most optical and electronic phenomena and therefore particularly convenient for interpreting optical spectra. One can obtain the analytic expressions for band dispersion and effective masses around high-symmetry points, particularly for decoupled conduction and valence bands.

An electron in a crystal sees a periodic potential due to the ions present at each lattice site. Using Bloch's theorem, the electron wave functions for the periodic lattice potential are expressed as $\psi_{nk}(\boldsymbol{r}) = e^{i.\boldsymbol{k}.\boldsymbol{r}}u_{nk}(\boldsymbol{r})$, where $\boldsymbol{r}$ is the position vector, $u_{nk}(\boldsymbol{r}+\boldsymbol{R}) = u_{nk}(\boldsymbol{r})$ is a periodic function with the band index n and wave vector $\boldsymbol{k}$. The translation vector $\boldsymbol{R}=n_1\boldsymbol{a}_1+n_2\boldsymbol{a}_2+n_3\boldsymbol{a}_3$, where $\boldsymbol{a}_1$, $\boldsymbol{a}_2$, and $\boldsymbol{a}_3$ are the unit lattice vectors and n_1, n_2, and n_3 are integers. The electron wave function satisfies the Schrödinger equation. Therefore, the functions $u_{nk}(\mathbf{r})$ solve the unit cell Schrödinger equation, which includes the spin-orbit interaction

$$\left[H_0 + \frac{\hbar^2 k^2}{2m_0} + \frac{\hbar}{4m_0^2c^2}\nabla V \times \boldsymbol{p}.\boldsymbol{\sigma} + \frac{\hbar}{m_0}\boldsymbol{k}\cdot\boldsymbol{p} + \frac{\hbar^2}{4m_0^2c^2}\nabla V \times \boldsymbol{k}.\boldsymbol{\sigma}\right]u_{nk}(\boldsymbol{r}) = E_n(\boldsymbol{k})u_{nk}(\boldsymbol{r}) \qquad (2\text{-}8)$$

Here, V is the atomic potential; σ is the Pauli spin matrix and $H_0 = \frac{p^2}{2m_0} + V(r)$ is the free particle Hamiltonian. The last term on the left hand side is a $\boldsymbol{k}$-dependent spin-orbit interaction, which is small compared to other terms, because the crystal momentum, $\hbar\boldsymbol{k}$, is very small as compared with the atomic momentum, $\boldsymbol{p}$. The electron velocity in the atomic orbit is much larger than the velocity of the wave packet with the wave vectors in the vicinity of $\boldsymbol{k}_0$ (=0). Thus, only the first four terms are considered on the left-hand side

$$\left[H_0 + \frac{\hbar^2 k^2}{2m_0} + \frac{\hbar}{4m_0^2 c^2}\nabla V \times \boldsymbol{p}.\boldsymbol{\sigma} + \frac{\hbar}{m_0}\boldsymbol{k}\cdot\boldsymbol{p}\right]u_{nk}(\boldsymbol{r}) = E_n(\boldsymbol{k})u_{nk}(\boldsymbol{r}) \qquad (2\text{-}9)$$

At the zone center, $\boldsymbol{k}$=0 and $u_{n0}(\boldsymbol{r})$ satisfies the simpler equation

$$\left[H_0 + \frac{\hbar}{4m_0^2 c^2}\nabla V \times \boldsymbol{p}.\boldsymbol{\sigma}\right]u_{n\boldsymbol{0}}(\boldsymbol{r}) = E_n(\boldsymbol{0})u_{n\boldsymbol{0}}(\boldsymbol{r}) \qquad (2\text{-}10)$$

For zinc blende materials, e.g., GaInNAs, it is convenient to work with the basis functions of definite total angular momentum. By convention, the top of the valence band of the unstrained quantum well is set as the zero of energy. The electron wave functions are *p*-like near the top of the valence band and *s*-like near the bottom of the conduction band. For the electron in the conduction band, the basis functions of the lowest energy bands are given by

$$\left|\frac{1}{2}, \frac{\pm 1}{2}\right\rangle = \left|iS, \frac{\pm 1}{2}\right\rangle \qquad (2\text{-}11)$$

with energy E_g, where |S> = S(r) is spherically symmetric.

For the valence band, the lowest bands are

$$\left|\frac{3}{2},\frac{\pm 3}{2}\right\rangle = \frac{\mp 1}{\sqrt{2}}\left|X \pm iY, \frac{\pm 1}{2}\right\rangle$$
$$\left|\frac{3}{2},\frac{\pm 1}{2}\right\rangle = \frac{\mp 1}{\sqrt{6}}\left|X \pm iY, \frac{\mp 1}{2}\right\rangle + \sqrt{\frac{2}{3}}\left|Z, \frac{\mp 1}{2}\right\rangle \quad (2\text{-}12)$$
$$\left|\frac{1}{2},\frac{\pm 1}{2}\right\rangle = \frac{1}{\sqrt{3}}\left|X \pm iY, \frac{\mp 1}{2}\right\rangle \pm \frac{1}{\sqrt{3}}\left|Z, \frac{\pm 1}{2}\right\rangle$$

for heavy, light and split-off holes, respectively. The energy is $E_0 + \Delta/3=0$ for the heavy and light holes and $-\Delta$ for the split-off holes, where E_0 is the eigenenergy of the degenerate eigenfunctions of H_0. The split-off energy, Δ, is defined as

$$\Delta = \frac{3\hbar i}{4m_0^2c^2}\left\langle X \mid \frac{\partial V}{\partial x} p_y - \frac{\partial V}{\partial y} p_x \mid Y \right\rangle \quad (2\text{-}13)$$

This Δ is determined experimentally (Chuang 1995). The spin-orbit coupling splits the six-fold degeneracy into four-fold degenerate **J**=3/2 bands (heavy and light hole) and two-fold degenerate **J**=1/2 bands (split-off hole).

6-band K•P

The 6-band **k•p** deals with the six valence bands (heavy-hole, light-hole and spin-orbit split-off bands, all doubly degenerate).

These six valence bands are classified as class A. All other bands are denoted as class B. Luttinger-Kohen’s model takes into account the effect of bands in class A on the bands in class B. Figure 2-6 shows a pictorial representation of the classification of bands into class A and class B. Luttinger-Kohen’s model can also be generalized to include both the conduction bands in class A, especially for narrow bandgap semiconductors.

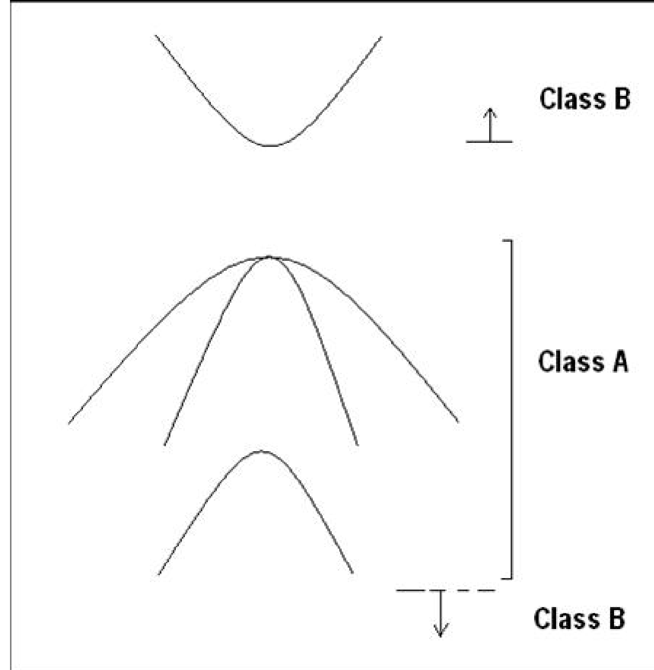

Figure 2-6: For 6-band k•p heavy hole, light hole and spin split-off bands in double degeneracy are of interest and called as class A. All other bands are denoted as class B.

For $\mathbf{k} \neq 0$, the wave functions $u_{nk}(\mathbf{r})$ are expanded as a linear superposition of the $\mathbf{k}=0$ basis eigenfunctions with the valence band wave functions. The effective Hamiltonian is determined by considering the band mixing among states of class A along with the perturbative influence of class B states. The mixing of the eigenfunctions is caused precisely by the $\mathbf{k} \cdot \mathbf{p}$ term and thus explains the model's name.

For the (100) oriented grown cubic semiconductors, the strain tensor elements are given by

$$\begin{aligned} \varepsilon_{xx} &= \varepsilon_{yy} = \frac{a_0 - a}{a} \\ \varepsilon_{zz} &= -2\frac{C_{12}}{C_{11}}\varepsilon_{xx} \\ \varepsilon_{xy} &= \varepsilon_{yz} = \varepsilon_{zx} = 0 \end{aligned} \qquad (2\text{-}14)$$

where, a_0 and a are the lattice constants of the substrate and the layer respectively. C_{11} and C_{12} are the elastic stiffness coefficients. After strain effects are included, the general result is that the effective Hamiltonian for 6x6 **k · p** theory is given by (Chuang 1995)

$$H = -\begin{bmatrix} P+Q & -S & R & 0 & -\frac{S}{\sqrt{2}} & \sqrt{2}R \\ -S^* & P-Q & 0 & R & -\sqrt{2}Q & \sqrt{\frac{3}{2}}S \\ R^* & 0 & P-Q & S & \sqrt{\frac{3}{2}}S^* & \sqrt{2}Q \\ 0 & R^* & S^* & P+Q & -\sqrt{2}R^* & -\frac{S^*}{\sqrt{2}} \\ -\frac{S^*}{\sqrt{2}} & -\sqrt{2}Q & \sqrt{\frac{3}{2}}S & -\sqrt{2}R & P+\Delta & 0 \\ \sqrt{2}R^* & \sqrt{\frac{3}{2}}S^* & \sqrt{2}Q & -\frac{S}{\sqrt{2}} & 0 & P+\Delta \end{bmatrix} \qquad (2\text{-}15)$$

where

$$P = \frac{\hbar^2}{2m_0}\gamma_1 k^2 - a_v(\varepsilon_{xx} + \varepsilon_{yy} + \varepsilon_{zz})$$
$$Q = \frac{\hbar^2}{2m_0}\gamma_2(k^2 - 3k_z^2) - \frac{b}{2}(\varepsilon_{xx} + \varepsilon_{yy} - 2\varepsilon_{zz})$$
$$R = \frac{\hbar^2}{2m_0}\sqrt{3}(-\gamma_2(k_x^2 - k_y^2) + 2i\gamma_3 k_x k_y) + \frac{\sqrt{3}}{2}b(\varepsilon_{xx} - \varepsilon_{yy}) - id\varepsilon_{xy}$$
$$S = \frac{\hbar^2}{2m_0}2\sqrt{3}\gamma_3(k_x - ik_y)k_z - d(\varepsilon_{xz} - i\varepsilon_{yz})$$

where, k_x, k_y, and k_z are the wave vectors and γ_1, γ_2 and γ_3 are Luttinger's parameters. The parameters, a_v, b and d are Pikus-Bir deformation potential.

The eigenenergy equation can be formulated using the 6×6 Hamiltonian. By solving the eigenenergy formulation the band edge energies and the effective masses can be obtained.

2.2.2 Effect of Nitrogen

The incorporation of Nitrogen into the GaInAs matrix significantly modifies the bandstructure. This effect is attributed to the Nitrogen related impurity band, known as the N-level, in the GaInAs host band structure. The interaction of Nitrogen-localized state with the host conduction band modifies the GaInNAs band structure.

Band Anticrossing

Incorporation of Nitrogen into GaInAs forms a Nitrogen-localized state, E_N. E_N changes with the Nitrogen-bonding configuration and Indium composition as follows (Duboz 2002)

$$E_N = E_{Ga} + i(E_{In} - E_{Ga})/4 - y\beta \tag{2-16}$$

where, $E_{Ga} = 1.65$ eV (corresponding to N-Ga_4In_0 configuration), $E_{In} = 1.9$ eV, (corresponding to N-Ga_0In_4 configuration), i = 0-4 is the number of Indium neighbors in the N environment, β = 0.56 eV is a weight parameter that reflects the effect of Indium composition on E_N and y is Indium composition in the GaInNAs QW (Klar 2001; Shan 2001).

E_N interacts with the GaInAs conduction band forming an eigenvalue problem

$$\begin{vmatrix} E-E_C & -V \\ -V & E-E_N \end{vmatrix} = 0 \tag{2-17}$$

where E_C is the uncoupled conduction band energy at Γ point of GaInAs, V describes the coupling between E_N and E_C, $V=[V_{Ga} + (V_{In}-V_{Ga})(i/4)]\sqrt{x}$ (where V_{Ga}=2.4, V_{In}=1.75 and x is Nitrogen composition) (Duboz 2002). The interaction of the GaInAs conduction band with Nitrogen related localized state results in the splitting of conduction band into two energy levels,

E_+ and E_-, where $E_+ > E_-$. E_- is of more interest because it acts as the conduction band of a GaInNAs alloy and is given by

$$E_- = \left(E_N + E_C - \sqrt{(E_N - E_C)^2 + 4V^2}\right)/2 \tag{2-18}$$

As the Nitrogen-bonding configurations changes from Gallium-rich to Indium-rich, E_N increases thus increasing the bandgap energy of GaInNAs (Klar 2001). The electron-to-heavy-hole transition energy, $E_{e1\text{-}Hh1}$, is calculated by solving the Schrödinger equation for conduction-band and heavy-hole band under effective mass envelop function scheme (Moore 1988; Chuang 1995). The physical parameters of GaInNAs at room temperature are mostly obtained by linear interpolations among those of the binary parents (i.e., GaAs, InAs, GaN and InN) according to Vegard's law (Vegard 1921). Appendix A lists the parameters used in this study (Strite 1993; Kim 1996; Meney 1996; Wright 1997; Li 2000; Park 2000; Vurgaftman 2003).

Table 2-1: Comparison of 6-band, 8-band and 10-band k·p models for dilute nitride material.

Model	**Includes conduction-valence band interaction**	**Include Presence of E_N**	**Electron effective mass**	**Valence band parameters used**
10-band	Yes	Yes	InGaAs	InGaAs
8-band	Yes	No	InGaAsN by BAC	InGaAsN
6+2-band	No	No	InGaAsN by BAC	InGaAsN
6+4-band	No	Yes	InGaAs	InGaAsN

Table 2-1 compares the 6-band, 8-band and 10-band **k•p** models for dilute nitrides. Generally 6-band **k·p**, described earlier, is sufficient for the bandstructure calculations. But when the bandgap becomes narrower and conduction band and valence band show coupling effect 8-

band **k·p** becomes more appropriate. Furthermore in the case of dilute nitrides, the existence of extra N-level needs to be taken into account to get better results. So, a 10-band **k·p** model is needed.

10-band K•P

The 10-band **k·p** is considered the most complete and appropriate for the dilute nitrides. In our study, we have used the 10-band **k·p** method as presented by Tomic *et al.*, to calculate the GaInNAs/GaAs subband dispersion and the optical gain spectra (Tomic 2003). In the 10-band **k · p** Hamiltonian of GaInNAs, the effect of N perturbation (for small values of y in $In_xGa_{1-x}As_{1-y}N_y$ layers) is treated by adding 'Nitrogen band' coupling to the conduction band of $In_xGa_{1-x}As$ (known as host structure). The resulting 10×10 Hamiltonian is given by

$$\begin{bmatrix} E_N & V_{NC} & 0 & 0 & 0 & 0 & 0 & 0 & 0 & 0 \\ V_{NC}^* & E_{CB} & -\sqrt{3}T_+ & \sqrt{2}U & -U & 0 & 0 & 0 & -T_- & -\sqrt{2}T_- \\ 0 & -\sqrt{3}T_+^* & E_{HH} & \sqrt{2}S & -S & 0 & 0 & 0 & -R & -\sqrt{2}R \\ 0 & \sqrt{2}U^* & \sqrt{2}S^* & E_{LH} & Q & 0 & T_+^* & R & 0 & \sqrt{3}S \\ 0 & -U^* & -S^* & Q^* & E_{SO} & 0 & \sqrt{2}T_+^* & \sqrt{2}R & -\sqrt{3}S & 0 \\ 0 & 0 & 0 & 0 & 0 & E_N & V_{NC} & 0 & 0 & 0 \\ 0 & 0 & 0 & T_+ & \sqrt{2}T_+ & V_{NC}^* & E_{CB} & -\sqrt{3}T_- & \sqrt{2}U & -U \\ 0 & 0 & 0 & R^* & \sqrt{2}R^* & 0 & -\sqrt{3}T_-^* & E_{HH} & \sqrt{2}S^* & -S^* \\ 0 & T_-^* & -R^* & 0 & -\sqrt{3}S^* & 0 & \sqrt{2}U^* & \sqrt{2}S & E_{LH} & Q \\ 0 & -\sqrt{2}T_-^* & -\sqrt{2}R^* & \sqrt{3}S^* & 0 & 0 & -U^* & -S & Q^* & E_{SO} \end{bmatrix}, \quad \textbf{(2-19)}$$

where, the following matrix elements are the same as in the conventional 8-band Hamiltonian (Chuang 1995; Tomic 2003).

$$E_{CB} = E_{c0} + \frac{\hbar^2}{2m_0}\left(1/m_c^* - \left(E_P/3\right)\left[2/E_g^h + 1/\left(E_g^h + \Delta\right)\right]\right)\left(k_\parallel^2 + k_z^2\right) + \delta E_{CB}^{hy},$$

$$E_{HH} = E_{v0} - \frac{\hbar^2}{2m_0}\left[\left(\gamma_1 + \gamma_2\right)k_\parallel^2 + \left(\gamma_1 - 2\gamma_2\right)k_z^2\right] + \delta E_{VB}^{hy} - \eta_{ax},$$

$$E_{LH} = E_{v0} - \frac{\hbar^2}{2m_0}\left[(\gamma_1 - \gamma_2)k_{\|}^2 + (\gamma_1 + 2\gamma_2)k_z^2\right] + \delta E_{VB}^{hy} + \eta_{ax},$$

$$E_{SO} = E_{v0} - \Delta - \frac{\hbar^2}{2m_0}\gamma_1\left(k_{\|}^2 + k_z^2\right) + \delta E_{VB}^{hy},$$

$$T_{\pm} = \frac{1}{\sqrt{6}}P\left(k_x \pm ik_y\right), \quad U = \frac{1}{\sqrt{3}}Pk_z, \quad S = \sqrt{\frac{3}{2}}\frac{\hbar^2}{m_0}\gamma_3 k_z\left(k_x - ik_y\right),$$

$$R = \frac{\sqrt{3}}{2}\frac{\hbar^2}{2m_0}\left[(\gamma_2 + \gamma_3)\left(k_x - ik_y\right)^2 - (\gamma_3 - \gamma_2)\left(k_x + ik_y\right)^2\right],$$

$$Q = -\frac{1}{\sqrt{2}}\frac{\hbar^2}{m_0}\gamma_2\left(k_x^2 + k_y^2\right) + \sqrt{2}\frac{\hbar^2}{m_0}\gamma_2 k_z^2 - \sqrt{2}\eta_{ax},$$

where, $k_{\|}^2 = k_x^2 + k_y^2$ (k_x, k_y, and k_z are the wave vectors) and the subscripts CB, HH, LH, and SO stand for conduction, heavy-hole, light-hole, and split-off bands, respectively. $\gamma_1 = \gamma_1^L - E_P/(3E_g^h)$, $\gamma_{2,3} = \gamma_{2,3}^L - E_P/(6E_g^h)$ are modified Luttinger-Kohn parameters. $E_p = 2m_0P^2/\hbar^2$, where, P is the Kane matrix element for the conduction band. $\delta E_b^{hy} = -2a_b(1 - C_{12}/C_{11})\varepsilon$ describes the effect of hydrostatic strain, where ε is the strain in the layer plane and subscript b = N, CB, and VB for Nitrogen, conduction and valence band respectively. $\eta_{ax} = -b_v(1 + 2C_{12}/C_{11})\varepsilon$ describes the effect of shear strain on the band structure (Chuang 1995).

$E_N = E_{c0} + \Delta E_{NC} + \delta E_N^{hy} - (\gamma - \kappa)\, y$, describe the band-edge of the N band. The difference between the unstrained conduction and Nitrogen-localized state is taken as (ΔE_{NC}=0.485 eV) (Tomic 2003). V_{Nc} describes the interaction between the N and C bands and is given by $V_{Nc} = -\beta\sqrt{y}$. Values for γ and β are 3.5 and 1.675, respectively (Meney 1996).

2.2.3 Model solid theory

The model solid theory is useful in determining the band offsets accurately for III-V heterostructures as required in **k·p** calculations. The combination of model solid theory (Van de

Walle 1989) and modification due to N band (Tomic 2003) can be used to calculate the band-edge energies. The valence band-edge energy (E_{v0}) and the conduction band-edge energy (E_{c0}) of the GaInNAs well material relative to GaAs, are expressed as (Chuang 1995)

$$\begin{aligned} E_{v0} &= \left(E_{v,av} + \frac{\Delta}{3} + 2a_v\left(1 - C_{12}/C_{11}\right)\varepsilon \right) + \kappa y, \\ E_{c0} &= \left(E_{v,av} + \frac{\Delta}{3} + 2a_c\left(1 - C_{12}/C_{11}\right)\varepsilon + E_g^h \right) - (\alpha - \kappa) y, \end{aligned} \qquad (2\text{-}20)$$

where the last terms on the right hand side of these equations represent the modification due to the N band; y is the fraction of N in the structure, α and κ are parameters which are taken to be 1.55 and 3.5, respectively (Tomic 2003).

2.2.4 Finite difference

This section describes the computational method used in solving the Schrödinger equation and the 10-band **k·p** model.

Schrodinger Equation

For GaAs based material, like other III-V materials, conduction and valence band are decoupled. In GaAs conduction band minima occurs at symmetrical Γ_6 valley. The energy states and wave function of electron, heavy hole and light hole at Γ_6 can be calculated using Duke-Daniel model (BenDaniel 1966). The wave equation has a 1-D Schrödinger-equation-like form

$$-\frac{\hbar^2}{2}\frac{\partial}{\partial z}\left[\frac{1}{m_r^*(z)}\frac{\partial \Psi_{rl}(z)}{\partial z}\right] + U_r(z).\Psi_{rl}(z) = E_{rl}\Psi_{rl}(z) \qquad (2\text{-}21)$$

where Ψ_{rl} and E_{rl} are envelop eigenfunctions of the lth subband of electrons (r=e), heavy holes (r=HH) or light holes (r=LH), and the eigenenergies respectively.

We have solved the Equation (2-21) as eigenvalue problem using 1-D finite difference method. Coefficients of the eigenmatrix were obtained from fourth order Taylor series expansions. The eigenmatrix is given by

$$H_{mn} = C_1(z_n)\delta_{m,n-2} + B_1(z_n)\delta_{m,n-1} + A(z_n)\delta_{m,n} + B_2(z_n)\delta_{m,n+1} + C_2(z_n)\delta_{m,n+2} \qquad \text{(2-22)}$$

Where the coefficients are

$$C_1(z_i) = \frac{\hbar^2}{24m_r^*(z_i)\Delta z^2}\left[\frac{\Delta z}{m_r^*(z_i)}\frac{\partial m_r^*(z_i)}{\partial z} + 1\right]$$

$$B_1(z_i) = -\frac{\hbar^2}{24m_r^*(z_i)\Delta z^2}\left[8\frac{\Delta z}{m^*(z_i)}\frac{\partial m_r^*(z_i)}{\partial z} + 16\right]$$

$$A(z_i) = \frac{5\hbar^2}{4m_r^*(z_i)\Delta z^2} + U_r(z_i)$$

$$B_2(z_i) = -\frac{\hbar^2}{24m_r^*(z_i)\Delta z^2}\left[-8\frac{\Delta z}{m^*(z_i)}\frac{\partial m_r^*(z_i)}{\partial z} + 16\right]$$

$$C_2(z_i) = \frac{\hbar^2}{24m_r^*(z_i)\Delta z^2}\left[-\frac{\Delta z}{m^*(z_i)}\frac{\partial m_r^*(z_i)}{\partial z} + 1\right]$$

$$\frac{\hbar^2}{m} = 3.01(nm^2 \cdot eV)$$

Now on solving the equation of the form $[H]\times[\psi] = E[\psi]$, we get the transition energies. For a compressively strained structure, due to valence band-splitting the heavy hole energy increases and the ground state transition corresponds to a transition between the conduction band and the heavy hole band.

Solving 10-band k·p model

In order to solve the 10-band **k·p** model, we apply the operator $p = -i\hbar\nabla$ to all k_z terms in the eigenvalue equation with matrix operator given in 10-band Hamiltonian. This operation is done to the k_z terms only, since quantization is assumed to be along the z-direction. In doing this, it is convenient to note that the resultant matrix takes the form

$$\begin{bmatrix} A_{11}\nabla_z^2 + B_{11}\nabla_z + C_{11} & \cdots & A_{1m}\nabla_z^2 + B_{1m}\nabla_z + C_{1m} \\ \vdots & \ddots & \vdots \\ A_{m1}\nabla_z^2 + B_{m1}\nabla_z + C_{m1} & \cdots & A_{mm}\nabla_z^2 + B_{mm}\nabla_z + C_{mm} \end{bmatrix} \begin{bmatrix} \chi_{1,z} \\ \chi_{2,z} \\ \cdots \\ \chi_{m-1,z} \\ \chi_{m,z} \end{bmatrix} = \bar{\varepsilon} \begin{bmatrix} \chi_{1,z} \\ \chi_{2,z} \\ \cdots \\ \chi_{m-1,z} \\ \chi_{m,z} \end{bmatrix} \tag{2-23}$$

where $\chi_{i,z}$ denote the wavefunction for i^{th} ($i=1,2,..m$) subband at z coordinate, A and B are the coefficients to 2nd and 1st order partial derivatives. The C terms denote potential offsets and all other terms not operated on by the momentum operator. All terms A, B, and C are actually z–dependent functions, though not denoted as such, to ease the notation. To ensure Hermiticity of the resulting matrix at the heterostructure interfaces, the discretization scheme as noted in Eppenga *et al*. (Eppenga 1987) has been used, where

$$\begin{aligned} B(z)\frac{\partial}{\partial z} &\rightarrow \frac{1}{2}\left(B(z)\frac{\partial}{\partial z} + \frac{\partial}{\partial z}B(z) \right) \\ A(z)\frac{\partial^2}{\partial z^2} &\rightarrow \frac{\partial}{\partial z}A(z)\frac{\partial}{\partial z} \end{aligned} \tag{2-24}$$

Applying these expansions to the m-band Hamiltonian (in general, m=10 for 10-band **k·p**) equation results in a matrix of the form shown in Table 2-2.

Table 2-2: General form of the expanded m-band Matrix. Each point in real-space, along the quantized z-axis corresponds to an m-row block in this matrix.

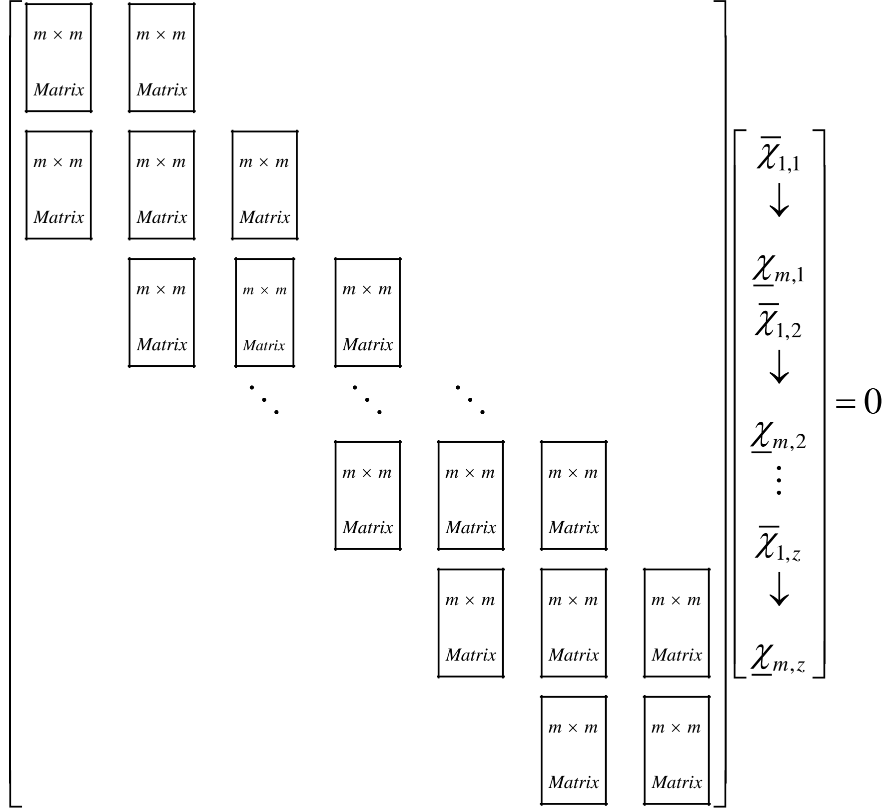

This matrix is then solved using an eigenvalue solver to get the eigenenergies and wavefunctions. These eigenenergies and wavefunctions are used to find the conduction (valence) subband energies and their envelop functions. The 10-dimensional electron and hole envelope wave functions for the QW can be expressed as

$$\Phi = \{\Phi_n^j\} \qquad (j = 1,2,\ldots,10)$$
$$\Phi_n^j = \exp[i(k_x x + k_y y)] \sum_m a_{n,m}^j \frac{1}{\sqrt{L}} \exp\left[i\left(k_z + m\frac{2\pi}{L} \right) z \right] \tag{2-25}$$

where L is the period of the QW, n is the index for energy subbands and $a_{n,m}^j$ is the expansion coefficient. In order to identify the Nitrogen level (N), conduction band (CB), heavy hole (HH),

light hole (LH), and the split-off (SO) band components in the energy states of the QW, we extend the probability functions given by (Ng 2005[1])

$$P_n^N = \sum_{j=1,6}\sum_m a_{n,m}^{j*}a_{n,m}^j, \qquad P_n^{CB} = \sum_{j=2,7}\sum_m a_{n,m}^{j*}a_{n,m}^j,$$
$$P_n^{HH} = \sum_{j=3,8}\sum_m a_{n,m}^{j*}a_{n,m}^j, \qquad P_n^{LH} = \sum_{j=4,9}\sum_m a_{n,m}^{j*}a_{n,m}^j, \tag{2-26}$$
$$P_n^{SO} = \sum_{j=5,10}\sum_m a_{n,m}^{j*}a_{n,m}^j$$

By calculating P_n^N, P_n^{CB}, P_n^{HH}, P_n^{LH} and P_n^{SO}, the constituting components (N, CB, HH, LH and SO) of the QW state *n* can be known. These probability functions are particularly useful in identifying the dominant character in a particular energy state and their sum should be one. The wave function Φ_n^j can be classified as belonging to the conduction band or valence band depending on the position of the energy subband and also the calculated probability functions.

2.2.5 Optical gain model

After calculating the subband structure, we use the many-body optical gain model to calculate the gain spectra. The optical gain, G, is calculated using (Minch 1999; Ng 2005[1])

$$G(\hbar\omega) = \left[1 - \exp\left(\frac{\hbar\omega - \Delta F}{k_B T}\right)\right]\frac{\pi^2 c^2}{n^2\omega^2} R_{sp}(\hbar\omega) \tag{2-27}$$

$$R_{sp}(\hbar\omega) = \frac{ne^2\hbar\omega}{\pi m_0^2 \varepsilon_0 \hbar^2 c^3}\sum_{n_e}\sum_{n_v}\int_{k_\parallel}\frac{Q^{n_c n_v}}{2\pi t_w} f_c f_v S(\hbar\omega) dk_\parallel \tag{2-28}$$

where $R_{sp}(\hbar\omega)$ is the spontaneous emission rate, f_c and f_v are Fermi-dirac distributions for electrons and holes respectively, $\Delta F = E_{fc} - E_{fv}$ is the quasi-Fermi level separation which is dependent on the carrier density, $\hbar\omega$ is the photon energy, *e* is electron charge, ε_0 is the free-space dielectric constant, n is the refractive index, *c* is the speed of light, and $Q^{n_c n_v}$ is the squared

optical transition matrix element (Minch 1999). The line broadening, S($\hbar\omega$), is modeled using a secant-hyperbolic function (Chow 1999)

$$S(\hbar\omega) = \frac{\tau_{in}}{\pi\hbar} sech\left(\frac{E_e(k_{\|}) - E_h(k_{\|}) - \hbar\omega}{\hbar/\tau_{in}}\right) \tag{2-29}$$

where τ_{in} is the intraband relaxation time. The secant-hyperbolic function has shown better agreement between experiment and theory of line broadening in semiconductor lasers as compared with the commonly used Lorenzian function (Tomic 2003). The intraband relaxation time, τ_{in}, is taken to be 0.1 ps (Park 1996; Tomic 2003) in our calculations.

Chapter 3: Indium Segregation in GaInNAs/GaAs QWs

The growth of high quality III-V compound semiconductor heterostructures has attracted a great deal of attention since last few decades. Segregation effect results in non-abrupt interfaces and a disordered (non-uniform) composition profile. The phenomenon of segregation has attracted considerable research interest because of its influence on optical and structural properties of QW structures and devices. However, as mentioned in section 1.4, we need high quality GaInNAs QWs for developing commercial GaInNAs lasers. Therefore crystalline quality of the active layer, abruptness of interfaces and compositional uniformity has to be improved for better laser performance.

Segregation theory is well established in metallic alloys for a long time as the practical impact of segregation at grain boundaries on metal strength has been recognized very early (Chadwick 1975). Moreover, many metals can be tested for segregation due to ease in attaining near-equilibrium thermodynamic conditions. Impurities segregate at surface or grain boundaries and surface composition of alloy is different from the bulk (e.g., the surface of Fe-Cr alloy is Cr-rich). This segregation effect has also been reported in various III-V semiconductor alloys, where they involve the bulk-surface re-distribution of group-III atoms. Particularly, during molecular beam epitaxy (MBE) growth certain Group III atoms tend to partially incorporate in the crystal layer and a portion of which remains at the surface. For example, segregation has been reported in number of systems such as Indium segregation in GaInAs / GaAs and AlInAs /

GaAs (Moison 1989; Schowalter 2006), Al segregation in AlGaAs / GaAs (Massies 1987), and Indium segregation in GaInP / GaAs (Mesrine 1996).

Indium surface-segregation during molecular beam epitaxy has been widely studied by several groups (Moison 1989, Muraki 1992, Schowalter 2006). There are several theoretical models (such as the equilibrium model, kinetic model and Muraki model) to explain the phenomenon of Indium segregation (Moison 1989; Muraki 1992; Dehaese 1995). In order to explain the phenomenon of segregation, an exchange mechanism between Indium and Gallium was proposed by Moison for Indium segregation in GaInAs/GaAs QWs (Moison 1989). This model supposed that the surface layer and bulk layer were in equilibrium. The Indium segregation length in GaInAs, grown on GaAs, was shown to increase from 0.8 to 2.9 nm when the growth temperature increased from 370 to 520 ^{0}C (Muraki 1992). The equilibrium model could not explain the relationship between the Indium segregation length and the substrate temperature as there did not exist the equilibrium for low temperature growth and high growth-rate (Dehaese 1995). To overcome this limitation, a kinetic model was proposed by Dehaese *et al.* (Dehaese 1995) and employed by Yamaguchi *et al.* (Yamaguchi 1997), by introducing the element of non-stationarity. Till now, both the equilibrium and kinetic models have been used for materials with one group V species, e.g., GaInAs (Dehaese 1995, Yamaguchi 1997), GaInN (Inahama 2005) and InAlGaAs (Jensen 1999). In this work, we extend kinetic model for dilute nitride with two group-V elements.

This chapter presents a study on Indium segregation in MBE grown GaIn(N)As/GaAs quantum wells. The experimental reports based on reflection high energy electron diffraction (RHEED) and secondary ion mass spectroscopy (SIMS) measurement showed the evidence of Indium segregation in GaInNAs/GaAs quantum wells (Liu 2006[4]). This chapter is divided into

two parts; the first part, section 3.1, studies Indium segregation using kinetic model (Dehaese 1995), and the second part, section 3.2, studies the effect of Indium segregation on optical properties, including band structure and transition energies. Finally, section 3.3 presents the conclusion.

3.1 Kinetic modeling of Indium segregation

Incorporation of Nitrogen into GaInAs matrix is recognized as a promising method to realize high performance 1.3-1.55 µm lasers. However, the mechanisms controlling the incorporation of Indium and Nitrogen to reach the desired wavelength are not well understood. For plasma-assisted MBE growth of GaInNAs, it has been reported that Nitrogen incorporation is not affected by Indium content (Tournie 2000), while the effect of Nitrogen on Indium incorporation is lacking in literature (Luna 2007). Our recent studies suggest enhanced Indium segregation due to the incorporation of Nitrogen during the growth of GaInNAs QWs (Liu 2006[4]). The enhanced Indium segregation in the growth of GaInNAs/GaAs QW has also been observed by transmission electron microscopy (Luna 2007). But there has been no systematic theoretical investigation on such a phenomenon in GaInNAs material. In order to understand the role of Nitrogen, and possibly control abruptness of heterointerface in GaInNAs/GaAs, it is necessary to develop a theoretical model considering the effect of Nitrogen on Indium incorporation.

In this section, we develop a kinetic model to study the Indium surface-segregation in GaInNAs/GaAs(N) QWs. GaInNAs/GaAs QW samples were grown using the MBE as described in the next section. The segregation length for GaInNAs QW, with different

composition, was measured from SIMS. The kinetic model developed by Dehaese *et al.* has explained the segregation phenomenon in the GaInAs/GaAs very well. We extend this kinetic model to explain the segregation phenomenon in dilute nitride, GaInNAs, QWs. The modified model has been used to predict the Indium segregation lengths for growth temperatures of 400 ^{0}C to 500 ^{0}C, the molecular beam epitaxy growth window for GaInNAs.

3.1.1 Brief description of experiment

The samples studied here, A, B and C, are 10-periods $Ga_{0.665}In_{0.335}N_yAs_{1-y}$/GaAs(N) multi-quantum wells (MQWs) grown on GaAs (100) substrates by solid-source MBE. The nominal thicknesses are 6.1 and 24 nm for the GaInNAs wells and GaAs(N) barriers, respectively. The nominal Nitrogen composition in the QWs, y, is 0%, 0.69%, and 3.15% for samples A, B and C respectively. Sample A was grown without Nitrogen. Nitrogen was generated by a radio-frequency plasma source (Liu 2006[4]). In order to change the incorporation of N while keeping otherwise the same growth conditions, i.e. without changing the RF power or the N flow rate, we grew the samples by dispersive/direct N mode (Wang 2002). Sample B was grown with dispersive N mode for both the QWs and barriers. Sample C was grown with direct N mode in the QWs and dispersive N mode in the barriers. The QWs and barriers were grown at 460 °C. The QW structure was ended with a cap of 100-nm GaAs grown at 580 °C. Figure 3-1 shows the schematic diagram of these three samples (A, B and C).

The composition and Indium segregation length of the QW samples were determined by secondary-ion-mass spectroscopy (SIMS) (Liu 2006[4]). The segregation lengths were determined at the interface between the top GaInNAs QW and the GaAs cap, from SIMS spectra as

described by Liu et al in (Liu 2006[4]). This section concentrates on the theoretical modeling of Indium segregation using the experimentally measured segregation length.

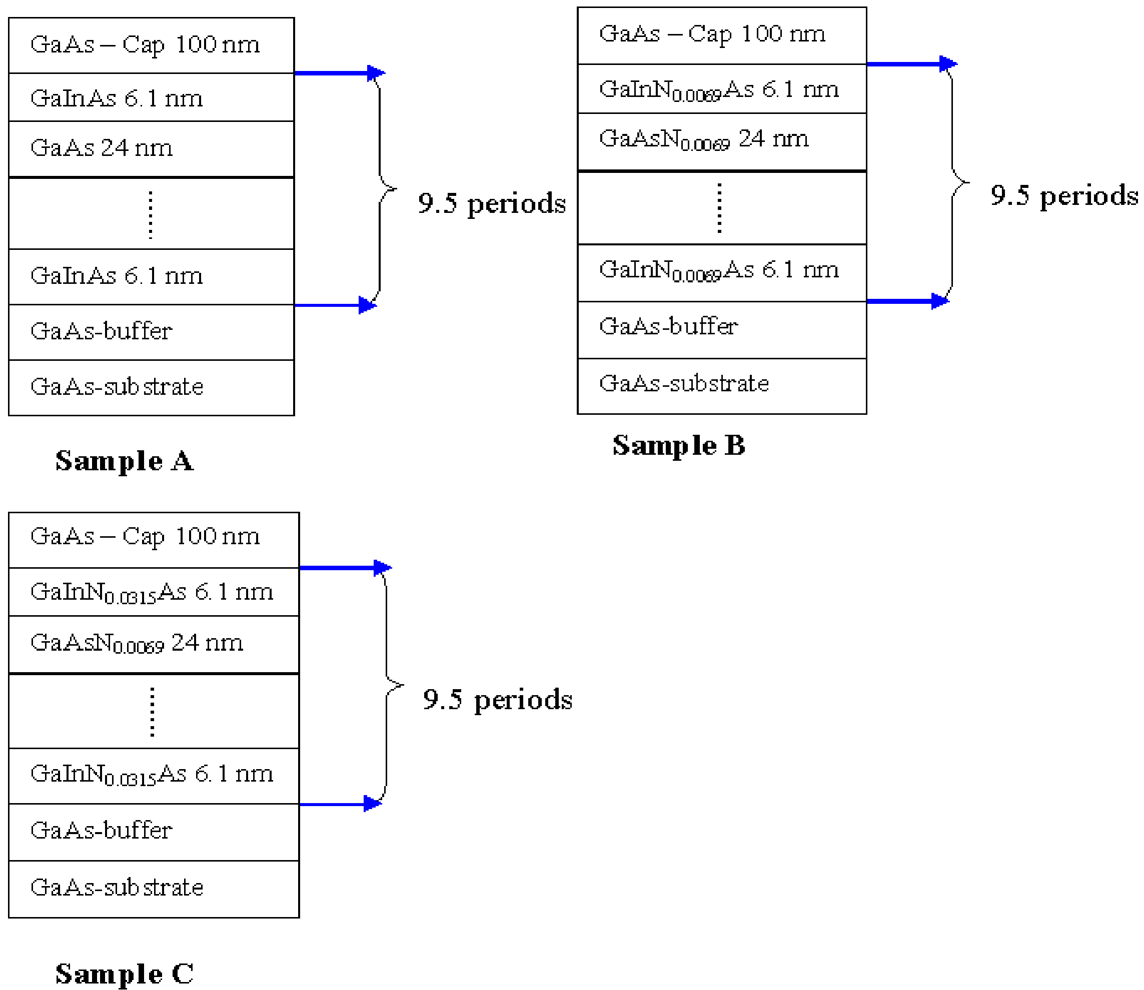

Figure 3-1: Schematic structure of samples A, B and C (each with Indium = 33.5%).

3.1.2 Modified kinetic model

In this study, the kinetic model (Dehaese 1995) concerning the analysis of surface segregation during the MBE growth of GaInAs/GaAs was adopted. In this model, surface segregation is regarded as an exchange between Group III atoms in the surface atomic layer with those underneath (the bulk).

$$[In]_{bulk} + [Ga]_{surface} \overset{E_1}{\underset{E_2}{\Leftrightarrow}} [In]_{surface} + [Ga]_{bulk} \tag{3-1}$$

where [In] and [Ga] are the compositions of Indium and Gallium atoms participating in the exchange process. E_1 and E_2 are energy barriers for the forward and backward reactions, respectively.

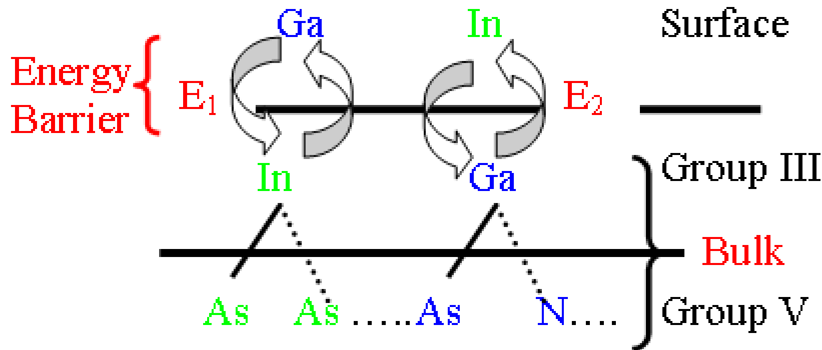

Figure 3-2: Schematic diagram showing the exchange process between surface and bulk Indium and Gallium atoms.

Figure 3-2 shows the schematic diagram of the exchange process. The exchange reaction proceeds to the right side of Equation 3-1 (Indium exchange from bulk to surface and Gallium exchange from surface to bulk) by overcoming an energy barrier E_1 and the reverse exchange reaction (Gallium exchange from bulk to surface and Indium exchange from surface to bulk) is possible by overcoming an energy barrier E_2. During MBE growth, Indium and Gallium atoms are supplied on the surface while the exchange process continues. In the exchange process, the forward and backward exchange rates are $R_1[In]_{bulk}[Ga]_{surface}$ and $R_2[In]_{surface}[Ga]_{bulk}$, respectively. Where, R_1 and R_2 are the rate constants for the forward and backward exchange reactions and are given by $R_1 = ve^{-(E_1/kT)}$ and $R_2 = ve^{-(E_2/kT)}$. Here, v is a vibration frequency, k is the Boltzmann constant, and T is the substrate temperature. When exchange rates are higher

compared to the growth rate (V_g) the bulk and the surface layer will be in the equilibrium, i.e., kinetic model (Dehaese 1995) gives the same result as equilibrium model (Moison 1989) and Indium segregation depends on the segregation energy, $E_s = E_2 - E_1$.

Since the exchange process corresponds to an atomic motion of Indium and Gallium atoms, the energy barriers E_1 and E_2 for GaInAs must be of the order of energy required to break the element III–As bonds in arsenide compounds (Moison 1989). Compared to GaInAs, GaInNAs has two group-V elements. Therefore the incorporation of Nitrogen is expected to change the energy barriers for the exchange process. Since GaInNAs has a small Nitrogen composition (dilute nitrides), the energy barriers are modeled linearly as $E_{1,2}\ (GaInNAs) = E_{1,2}\ (GaInAs) + \alpha_{1,2}$ [N]. Here, $E_{1,2}(GaInAs)$ are energy barriers for forward and backward reactions, in Equation 3-1, for GaInAs material only. [N] is the Nitrogen composition incorporated, and $\alpha_{1,2}$ are proportionality constants for the change in energy barriers with Nitrogen composition. $\alpha_{1,2}$ are the parameters to be determined by comparing the simulation with our experimentally deduced segregation lengths.

The incorporated Nitrogen in the GaInNAs tends to form short range order (SRO) clusters with Nitrogen bonding configurations, $N\text{–}In_mGa_{4-m}$ $(0 \leq m \leq 4)$ (Klar 2001). The cohesive energies of In-As, Ga-As, In-N and Ga-N are 1.55, 1.63, 1.93 and 2.24 eV/bond, respectively (Harrison 1989). The cohesive energies of III-N are much higher compared to that of III-As. As the bulk Nitrogen composition is small and III-N bonds are much stronger than that of III-As bonds, we can neglect the breaking of bulk III-N bonds and assume that only those bulk Indium and Gallium atoms bonded with Arsenic will participate in the exchange process. For the surface Group III atoms, as they have smaller coordination, the Indium and Gallium atoms in the

surface layer are loosely bonded to Arsenic and Nitrogen as compared to the bulk Group III atoms. Thus, we consider all the surface Indium and Gallium atoms to participate in the exchange process. The Equation (3-1) can be modified as,

$$[In]_{bulk,bonded\ with\ As} + [Ga]_{surface} \underset{E_2}{\overset{E_1}{\Leftrightarrow}} [In]_{surface} + [Ga]_{bulk,bonded\ with\ As} \quad (3\text{-}2)$$

The N–In$_m$Ga$_{4-m}$ configuration will affect the effective participation of Indium and Gallium atoms in the exchange reaction. Since we are dealing with dilute nitrides, we assume that these SRO clusters will be well separated. Thus for N–In$_m$Ga$_{4-m}$ configuration, the Equation (3-2) can be written as,

$$\left[[In]_{bulk} - m[N]\right] + [Ga]_{surface} \underset{E_2}{\overset{E_1}{\Leftrightarrow}} [In]_{surface} + \left[[Ga]_{bulk} - (4-m)[N]\right] \quad (3\text{-}3)$$

During the growth, Indium and Gallium atoms are supplied on the surface while the exchange process continues. Therefore, the continuous equation concerning the Indium composition is solved, and, as a result, the profile of Indium composition can be obtained as functions of the substrate temperature and the incident flux of III-group material (Dehaese 1995).

Figure 3-3 presents Indium composition profiles calculated by the kinetic model for GaInAs/GaAs heterostructure. The constant values are $v = 1\times10^{-13}$ s, $E_1(GaInAs)$ = 1.840 eV and $E_s(GaInAs)$ = 0.20 eV, which are taken from reference (Dehaese 1995). The simulation in Figure 3-3 has been performed for $Ga_{0.665}In_{0.335}As$ with GaAs growth rate $V_{g,GaAs}$ = 0.57 ML/s (i.e., $Ga_{0.665}In_{0.335}As$ growth rate = 0.86 ML/s) and growth temperature T = 460°C, the same condition as in our experiment. Since the segregation length is calculated at the GaInAs/GaAs interface when there is no Indium flux. Thus $V_{g,GaAs}$ is the actual growth rate during the Indium segregation into GaAs layer. The segregation length is deduced from the 1/e decay length of Indium composition profile at the upper interface (GaAs on GaInAs), shown in the inset of

Figure 3-3. The segregation length obtained from Figure 3-3 is 1.12 nm which is very close to the segregation length deduced from SIMS measurements for our GaInAs/GaAs sample, 1.14 nm (sample A, in Figure 3-1).

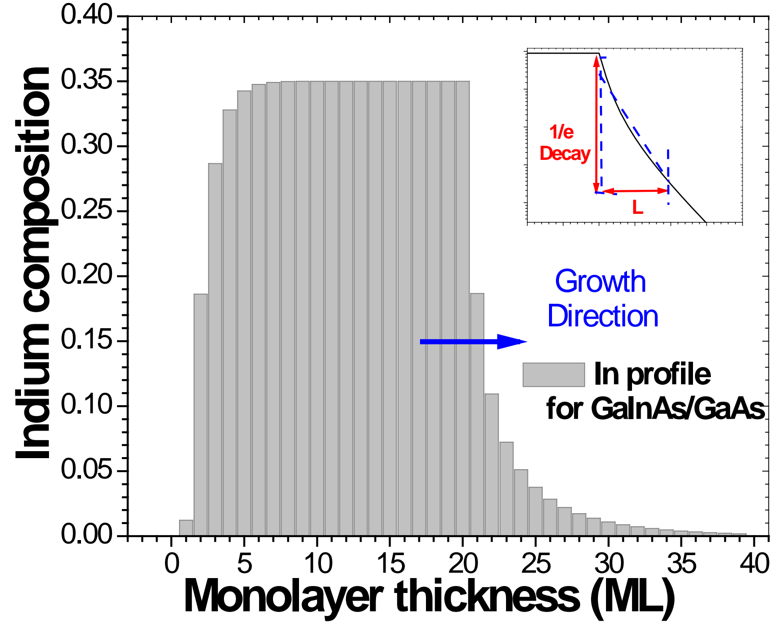

Figure 3-3: Calculated Indium composition profiles at substrate temperature 460 ^{0}C and a growth rate of GaAs 0.57 ML/s. Nominal widths of $Ga_{0.665}In_{0.335}As$ QW and GaAs barrier are 20 ML and 15 ML, respectively. Segregation length is obtained from decay length at the upper heterointerface as shown in inset.

3.1.3 Results and discussion

The model parameters α_1 and α_2 have been obtained by minimizing the mean square error,

$$Err(\alpha_1,\alpha_2) = \sum_{[N]} [L_{SIMS}([N]) - L_c(\alpha_1,\alpha_2,[N])]^2 \qquad (3\text{-}4)$$

where L_{SIMS} is the segregation length deduced from SIMS measurements and L_c is the calculated segregation length from simulation. The values of α_1 *and* α_2 are obtained by minimizing the function, $Err(\alpha_1,\alpha_2)$. The search was carried out in the range of -200 to 200 meV for both α_1 and α_2. The research report (Alt 2001) suggest the presence of N-In_0Ga_4 as dominant configuration in

the *as-grown* GaInNAs layer, L_c has been calculated for this N-bonding configuration, i.e. with $m = 0$. Pavelescu has reported that while growing the GaAs cap layer, at higher temperature than that of the QW growth, the N-bonding configuration changes due to self-annealing effect (Pavelescu 2003). Since the Indium segregation occurs at the interface before the GaAs cap layer is fully grown, the dominant N-bonding configuration will be the N-bonding configuration existing before self-annealing. Moreover, at the cap layer growth temperature, 580 ^{0}C, the Gallium/Indium interdiffusion coefficient is negligible (Dixit 2008), therefore self-annealing due to the cap layer growth does not play an important role in determining the Indium segregation length. The values of α_1 and α_2 obtained from the above procedure are -28.95 and -63.52 meV respectively.

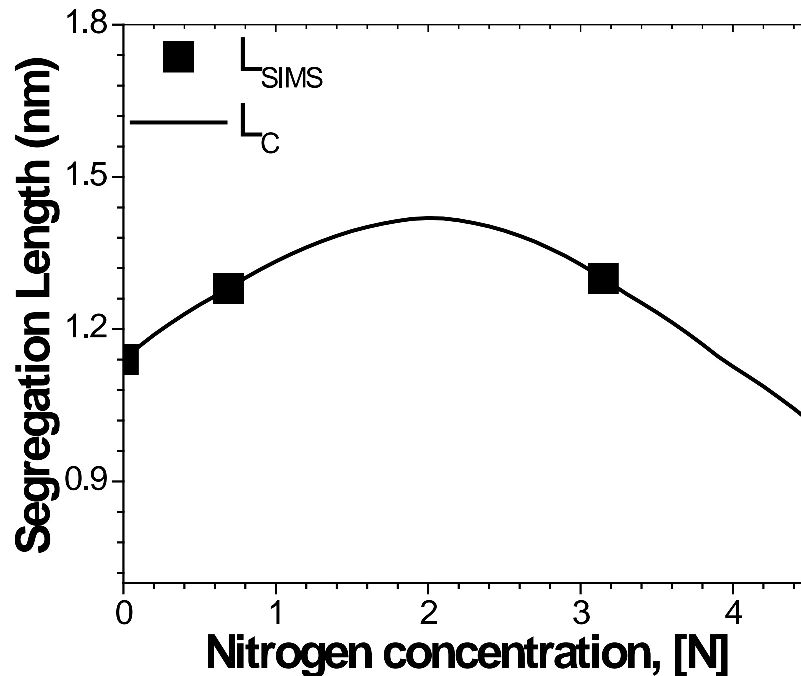

Figure 3-4: Segregation length vs. Nitrogen composition for $Ga_{0.665}In_{0.335}N_yAs_{1-y}$ QW at growth temperature of 460 ^{0}C for calculated (L_C) and experimental deduced (L_{SIMS}) segregation lengths.

Figure 3-4 shows the calculated segregation length, L_c variation with Nitrogen composition for $Ga_{0.665}In_{0.335}N_yAs_{1-y}$ QW at growth temperature of 460 ^{0}C, using α_1 and α_2. The experimental results, L_{SIMS}, are presented as the solid squares.

The negative values of α_1 and α_2 indicate reduced energy barriers for the forward and backward exchange processes in GaInNAs as compared to those in GaInAs. During the exchange reaction bulk Gallium/Indium atoms will break bonds with Arsenic and form bonds at surface with Arsenic or Nitrogen. Formation of III-N bond is energetically favorable compared to III-As bond due to the larger cohesive energies of III-N bonds. We speculate that the excess energy supplied by the formation of III-N bonds may contribute towards lowering the energy barrier for the exchange reaction resulting in negative values of $\alpha_{1,2}$. For the forward reaction Indium atoms exchange from bulk to surface and some of the Indium atoms may bond with the Nitrogen at surface. The difference between cohesive energies of In-As and In-N, 0.38 eV/bond, will contribute towards lowering the energy barrier for forward exchange reaction. Similarly, for the backward reaction Gallium atoms will exchange from bulk to surface. The difference between cohesive energies of Ga-As and Ga-N, 0.61 eV/bond, may contribute towards lowering the energy barrier for backward exchange reaction. The greater cohesive energy difference may be responsible for the greater lowering of energy barrier for backward exchange reaction as compared to forward exchange reaction, i.e., the larger magnitude of α_2 compared to α_1.

Figure 3-5 shows the difference between forward and backward exchange rate constants (R_1-R_2) and the segregation energy (E_s) *vs*. the Nitrogen composition at 460 ^{0}C. As Nitrogen composition increases the difference between forward and backward exchange rate constants (R_1-R_2) increases, therefore we can expect an increase of Indium segregation length. But, we also

notice that E_s decreases with Nitrogen composition, which will decrease the Indium segregation. It has been established that Indium segregation is predicted by E_s only when bulk and surface layer are in equilibrium (Dehaese 1995). Thus, we can expect that the Indium segregation will follow the trend of (R_1-R_2) to increase with Nitrogen composition when the exchange rate is lower than growth rate, i.e., when the bulk and surface layer are not in equilibrium (kinetically limited). Once the exchange rate is equal to or greater than the growth rate, surface and bulk layers easily reach to equilibrium. In this situation the Indium segregation will follow the trend of E_s, i.e., decreases with [N].

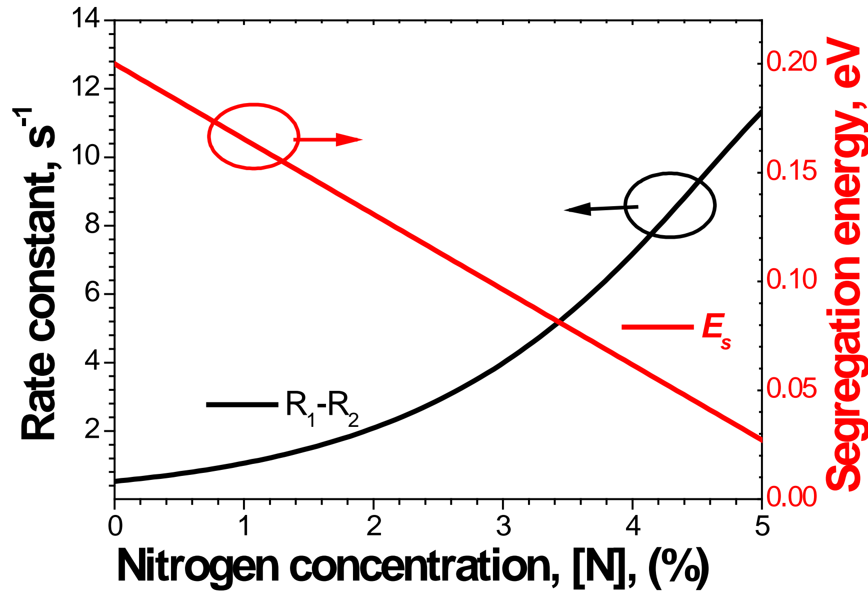

Figure 3-5: The difference between forward and backward exchange rate constants (R_1-R_2) and the segregation energy (Es) vs. the Nitrogen composition for $Ga_{0.665}In_{0.335}N_yAs_{1-y}$ QW at growth temperature of 460 ^{0}C.

While Nitrogen composition increases, the energy barriers decrease and the exchange rates increase. In order to find the equilibrium region, we calculate the equilibrium exchange rates by equating the forward exchange rate and backward exchange rate. This leads to

$$[In]_{surface}[Ga]_{bulk} / [In]_{bulk}[Ga]_{surface} = R_1/R_2 = exp(E_s/kT). \quad (3\text{-}5)$$

The equilibrium exchange rates are calculated, by solving the Equation 3-5, for nominal bulk Indium and Gallium compositions. On solving this equation we can get the exchange rates at equilibrium as a function of E_s thus a function of Nitrogen composition.

Figure 3-6 shows the exchange rate *vs*. Nitrogen composition curves for growth temperatures of 400 – 500 ^{0}C. The equilibrium exchange rate is increasing with the Nitrogen composition due to reduced energy barriers. Also shown in Figure 3-6 are horizontal lines representing growth rates of V_g = 0.57 ML/s and V_g = 1 ML/s. When the growth rate is higher than the exchange rate, the surface monolayer will be quickly formed leaving little time for the exchange process to reach equilibrium. The intersection points of exchange rates with growth rate will give the transition points from kinetically limited region to equilibrium region for the respective growth rate.

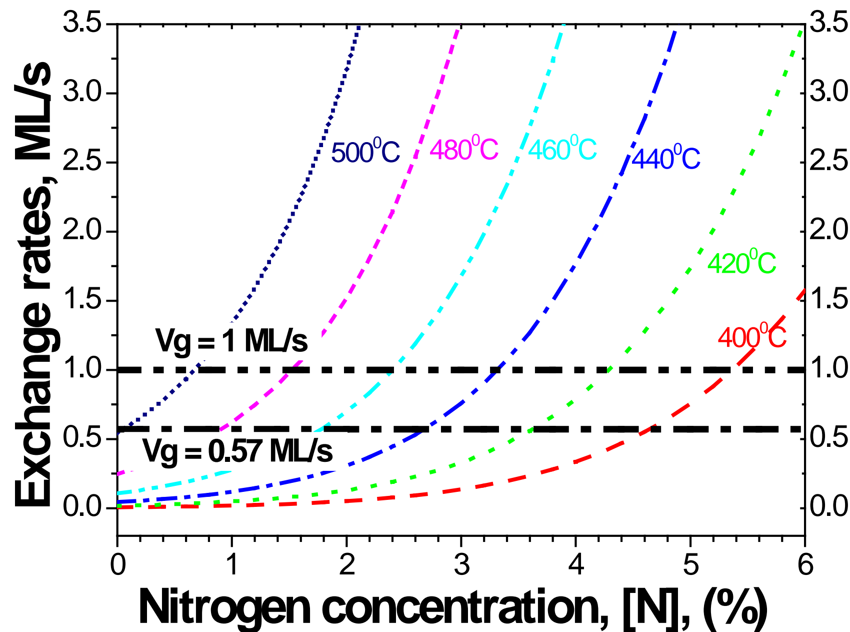

Figure 3-6: The equilibrium exchange rate vs. Nitrogen composition curves for $Ga_{0.665}In_{0.335}N_yAs_{1-y}$ QW at various growth temperatures. Two horizontal lines correspond to GaAs growth rate, Vg = 0.57 ML/s and 1 ML/s.

This result can be used to depict the kinetically limited and equilibrium regions as shown in Figure 3-7 which plots the growth temperature *vs.* the Nitrogen composition. From Figure 3-7 one can see that for a given Nitrogen composition, as growth temperature increases growth tends to go into the equilibrium region (vertical red arrow). Also, for a given temperature with increasing Nitrogen composition growth tends to go into the equilibrium region (horizontal green arrow). Considering our data for [N] = 0.69% and [N] = 3.15%, they locate at a kinetically limited region and equilibrium region respectively. This explains the trend observed in Figure 3-4 where Indium segregation follows an increasing trend at [N] = 0.69% due to being in kinetically limited region. Thus it follows the $(R_1\text{-}R_2)$ ~ [N] trend. When [N] = 3.15%, it is in equilibrium region, thus it follows E_s ~ [N] trend, i.e., decreases with [N].

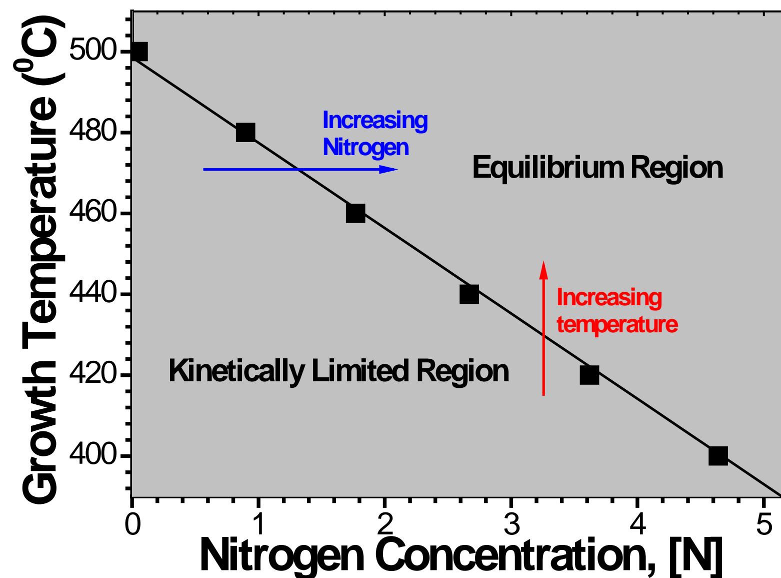

Figure 3-7: Nitrogen composition vs. growth temperature showing the kinetically limited and equilibrium regions for $Ga_{0.665}In_{0.335}NAs$ QW with GaAs growth rate = 0.57 ML/s.

Figure 3-8 shows the calculated Indium segregation length variation with N composition for various growth temperatures and with GaAs growth rates, (a) $V_{g,GaAs}$ = 0.57 ML/s and (b) $V_{g,GaAs}$ = 1 ML/s. Figures 3-8(a) and (b) show that for a fixed temperature, the segregation length

firstly increases with Nitrogen composition and after a maximum value start to decrease with further addition of Nitrogen. The Nitrogen composition corresponding to peak segregation length is actually the transition point from kinetically limited region to equilibrium region. We can see that the transition point happens at lower [N] for higher temperature. Comparison of Figure 3-8(a) and (b) also shows that the transition point moves to lower [N] with lower growth rate. This can be explained from the Figure 3-6 that for a certain growth temperature, the intersection of equilibrium lines with higher growth rate, V_g = 1 ML/s, corresponds to a higher [N], as compared to V_g = 0.57 ML/s. At higher growth rate the kinetically limited region expands towards higher [N]. This is because at higher growth rate monolayer is quickly formed and thus leaving lesser time for the exchange reaction (Dehaese 1995).

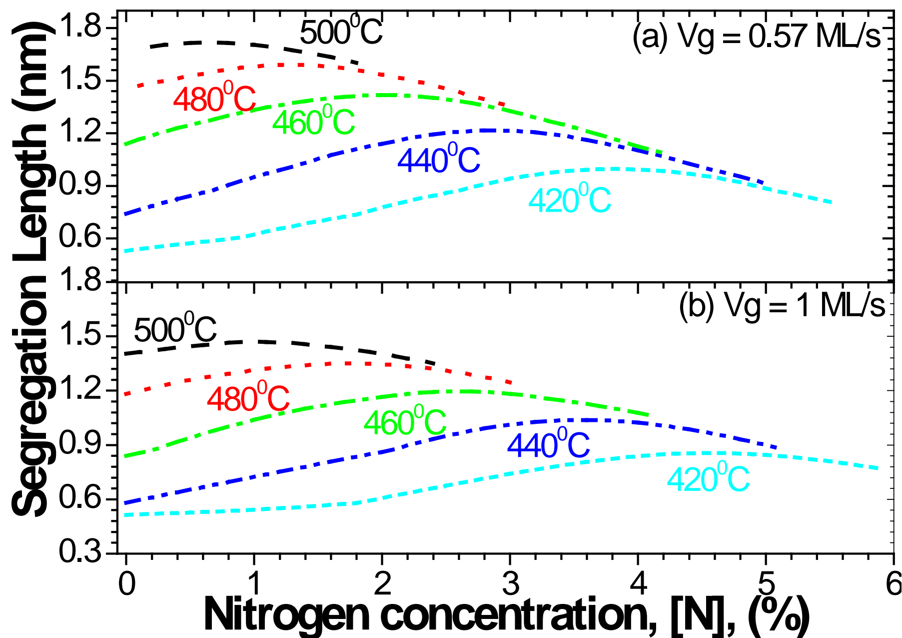

Figure 3-8: Calculated Indium segregation length variation with Nitrogen content in the $Ga_{0.665}In_{0.335}NAs/GaAs$ QW for GaAs growth rate (a) growth rate = 0.57 ML/s and (b) growth rate = 1 ML/s, at different growth temperatures.

It should be noted that the above work on modeling the Indium segregation in GaInNAs/GaAs quantum wells is only a preliminary work. The proposed model is limited by the

experimental data. We have currently only three experimental data points available as shown in Figure 3-4. A model based on such limited data may not be valid in a general case. More experimental data would be needed to validate the model.

3.2 Effect of segregation on subbands

In the previous section, we studied the origin of Indium segregation in GaInNAs/GaAs QWs. Naturally, a question arises: how does this Indium segregation affect the optical properties of GaInNAs QWs? This section studies the effect of Indium segregation on band structure and optical transition energies of strained GaInNAs / GaAs quantum wells. As we are looking into the applications at 1.3 and 1.55 μm emission wavelengths, the nominal (In, N) compositions in the quantum well are chosen accordingly.

Two GaInNAs/GaAs QW structures, for 1.3 and 1.55 μm respectively, are described in section 3.2.1. A simple model developed by (Muraki 1992) is used to calculate the composition profiles of the QWs with different segregation efficiencies (a parameter related to the segregation length) of Indium atoms. Section 3.2.2 describes the Muraki model. Section 3.2.3 shows the corresponding strain profile in the quantum well for various segregation efficiencies. Confinement potentials of electron and hole are then derived from composition and strain profiles as described in section 3.2.4. The energies of electrons and holes are numerically calculated by solving the Schrödinger equation, which includes the effects of valence band mixing and strain. Section 3.2.5 presents the results and discussion on the subband energy levels and optical transition energy for heavy-hole band and light-hole band as a function of the segregation efficiency.

3.2.1 The structures studied

Two single GaInNAs /GaAs quantum well structures have been studied theoretically. The GaInNAs /GaAs quantum well has a 7.5-nm thick $Ga_{1-x}In_xN_yAs_{1-y}$ single QW sandwiched between GaAs barriers. Figure 3-9 shows the nominal composition and thickness of the GaInNAs/GaAs QW structures. The Indium and N composition are selected as x = 65%, y = 1.5% for the emission wavelength at 1.3 µm and x = 61%, y = 3.9% for emission wavelength at 1.55 µm. These compositions are chosen such that the QW is within a critical thickness to avoid the creation of dislocations.

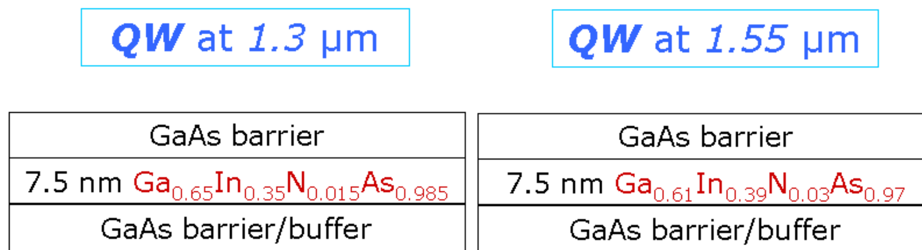

Figure 3-9: Schematic of GaAs/GaInNAs/GaAs QW structures for 1.3 and 1.55 um emission wavelength.

3.2.2 Muraki model

We employ Muraki's model of segregation for consecutive monolayers, but interpolate it to form a continuous function of z-axis in growth direction. We assume that the same segregation efficiency applies to all the monolayers. The composition profile for segregated QW is characterized by a segregation efficiency R that is given by $e^{-(d/L)}$, here d is the thickness of one monolayer and L is segregation length. During the growth of the QW, the impinging Indium atoms are partially (1-R) incorporated into the growing layer with the remaining fraction R incorporated into the following layer. Thus, for a single $Ga_{1-x}In_xN_yAs_{1-y}$ / GaAs quantum well

with segregation efficiency, R, composition profile of Indium along the growth direction z is given by

$$x(z) = \begin{cases} x_0\left(1 - R^{z/d}\right) & \left(0 \le z \le t_w\right) \\ x_0\left(1 - R^{t_w/d}\right)R^{(z-t_w)/d} & \left(t_w < z \le t_w + t_b\right) \end{cases} \quad (3\text{-}6)$$

where t_w and t_b are the thicknesses of quantum well and barrier, respectively. Here, x_0 is the nominal Indium mole fraction for ideal square quantum well. The GaInNAs quantum well starts at z = 0. The mole fraction of Nitrogen is assumed to be abrupt based on the experiments that Indium does not affect the incorporation of Nitrogen during MBE growth (Pan 2000[1]; Tournie 2000). Thus, for y_0 as mole fraction, Nitrogen profile is expressed as

$$y(z) = \begin{cases} y_0 & (0 \le z \le t_w) \\ 0 & (t_w < z \le t_w + t_b) \end{cases} \quad (3\text{-}7)$$

3.2.3 Segregation effect on strain

The lattices mismatch between the thin QW and thick barriers results in tetragonal deformation of the QW lattice. The effect of hydrostatic strain is two-fold; biaxial compressive in-plane strain along [100] and [010] directions, and uniaxial shear strain along [001], i.e. crystal growth direction. The in-plane strain and uniaxial shear strain across the QW will vary according to the composition of $Ga_{1-x}In_xN_yAs_{1-y}$ due to Indium segregation. The strain for segregated QWs can be given by (Chuang 1995)

$$\begin{aligned} \varepsilon_{//} &= \varepsilon(x, y) \\ \varepsilon_{\perp} &= -2[c_{12}(x, y)/c_{11}(x, y)]\varepsilon(x, y) \end{aligned} \quad (3\text{-}8)$$

where c_{11}(x, y) and c_{12}(x, y) are elastic stiffness constants. ε(x, y) is the misfit factor between the well and barrier depending on Indium and N compositions in the QW, which is negative for

compressive strain. Indium segregation modifies the QW structure and the hydrostatic strain, leading to a change in the bandgap that can be given by

$$U = E_n - \sum \Delta E_r \pm \Delta S \tag{3-9}$$

where E_n is the unstrained bandgap energy, ΔE_r and ΔS are the changes in bandgap energy. Subscript "r" refers to "c" (conduction band edge) or "v" (valence band edge). The change of the band edge due to hydrostatic strain can be expressed as

$$\Delta E_r(x,y) = \pm 2a_r(x,y)\left[1 - \frac{c_{12}(x,y)}{c_{11}(x,y)}\right]\varepsilon(x,y) \tag{3-10}$$

where a_r refers to a_c (hydrostatic deformation potential of conduction band) or a_v (hydrostatic deformation potential of valence band). ΔS is the change in valence band structure due to shear strain. Shear strain breaks the degeneracy of the heavy and light hole bands, shifting the heavy hole band up for compressive strain. ΔS can be expressed by

$$\Delta S(x,y) = -b(x,y)\left[1 + 2\frac{c_{12}(x,y)}{c_{11}(x,y)}\right]\varepsilon(x,y) \tag{3-11}$$

where b(x,y) is the shear deformation potential. The conduction band edge can be assumed to be unaffected by shear deformation, i.e., ΔS is zero for conduction band. Figure 3-10 summarizes the effect of compressive and tensile strain on the band-edges of the conduction and valence bands.

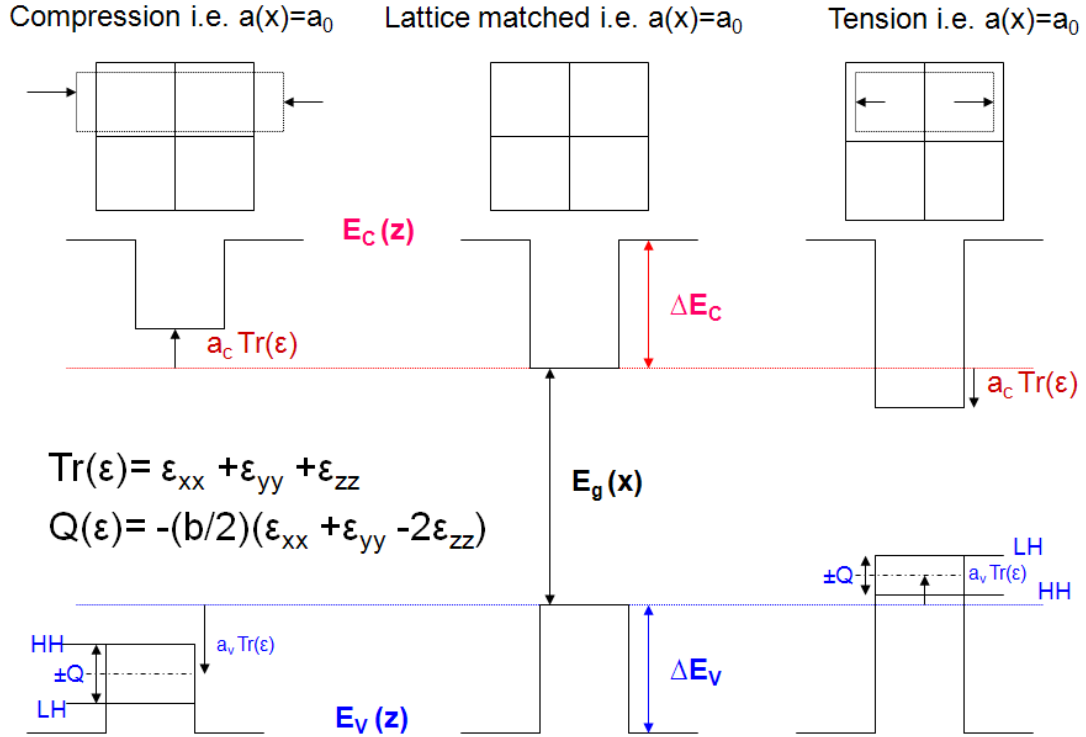

Figure 3-10: Effect of compressive and tensile strain on the conduction and valence band-edges.

3.2.4 Subband energies

To calculate the electron, heavy hole and light hole wave functions in the Indium segregated $Ga_{1-x}In_xN_yAs_{1-y}$ / GaAs QWs, we apply the multiple-band effective mass theory in the envelop function scheme as described in section 2.2. When calculating we assume that the envelope functions satisfy the boundary conditions at the QW interface. The effective mass theory has been proved effective in the calculations of a GaAs-based QW with the well width down to 2-nm (Moore 1988). Therefore, the error due to the effective mass approximation in the calculations of the 7.5-nm GaInNAs / GaAs QW is negligible. In GaInNAs with dilute Nitrogen incorporated, the conduction and valence bands are well separated and decoupled. Both the minimum in the conduction band and the maximum in the valence band occur at the symmetrical Γ_6 valley.

The composition dependence of bulk bandgap of $Ga_{1-x}In_xN_yAs_{1-y}$ is calculated using band the anti-crossing (BAC) model (Duboz 2002).

$$E_g(Ga_{1-x}In_xN_yAs_{1-y}) = \frac{1}{2}\left[E_g(Ga_{1-x}In_xAs) + E^N - \sqrt{(E_g(Ga_{1-x}In_xAs)\times E^N)^2 + 4V^2x}\right] \quad \textbf{(3-12)}$$

Where $E_g(Ga_{1-x}In_xAs) = x\,E_g(InAs) + (1-x)E_g(GaAs) - x(1-x)C$, E^N = 1.65 -0.31y, and V = *3.0 - 0.65y*. C is the bowing parameter (0.51 eV) (Li 1999). The band offset ratio, $Q_c = \Delta E_c/\Delta E_0$, at the hetero-junctions is chosen to be Q_c = 0.8 based on the experimental measurements (Hetterich 2000). Here, ΔE_c and ΔE_0 are energy differences of the conduction bands and band gaps, respectively.

The electron and hole wave functions at the zone center of the Γ_6 valley can be calculated separately in accordance with the Ben–Daniel and Duke models (Ben Daniel 1966). The wave equation has a form of one-dimensional Schrödinger-like equation as given below

$$-\frac{\hbar}{2}\frac{\partial}{\partial z}\left[\frac{1}{m_r^*(z)}\frac{\partial \psi_{rl}}{\partial z}\right] + U_r(z)\cdot\psi_{rl}(z) = E_{rl}\psi_{rl}(z) \quad (3\text{-}13)$$

where ψ_{rl} and E_{rl} are the eigen wavefunctions and eigenenergies of the subband in level l of electrons (r = e), heavy holes (r = Hh), or light holes (r = Lh), $m_r^*(z)$ is the effective mass and U_r(z) is the confinement profile.

The physical parameters of GaInNAs at room temperature are mostly obtained by linear interpolations among those of the binary parents (i.e. GaAs, GaN, InAs, and InN) according to Vegard's law (Vegard 1921). Appendix A presents the parameters used in this study (Strite 1993; Kim 1996; Meney 1996; Wright 1997; Li 2000; Park 2000; Vurgaftman 2001; Vurgaftman 2003).

The eigenenergy problem, Equation (3-12), can be numerically solved for electrons in conduction band and heavy and light holes in valence band separately by using a one-dimensional finite difference method with the confinement profiles given in Equation (3-9). Coefficients of the eigenmatrix were obtained from fourth order Taylor series expansions. The detailed procedure has been described in the section 2.2.4 in chapter 2.

The solution to the equation of the form $[H]\times[\psi]=E[\psi]$ gives the eigenenergy for each band. The optical transition energy e_1-Hh_1 (e_1-Lh_1) is then obtained by the energy difference between electrons and heavy (light) holes confined in the ground states.

3.2.5 Results and Discussion

First of all, we calculate the composition profile in the GaInNAs / GaAs QW for nominal and segregated structures.

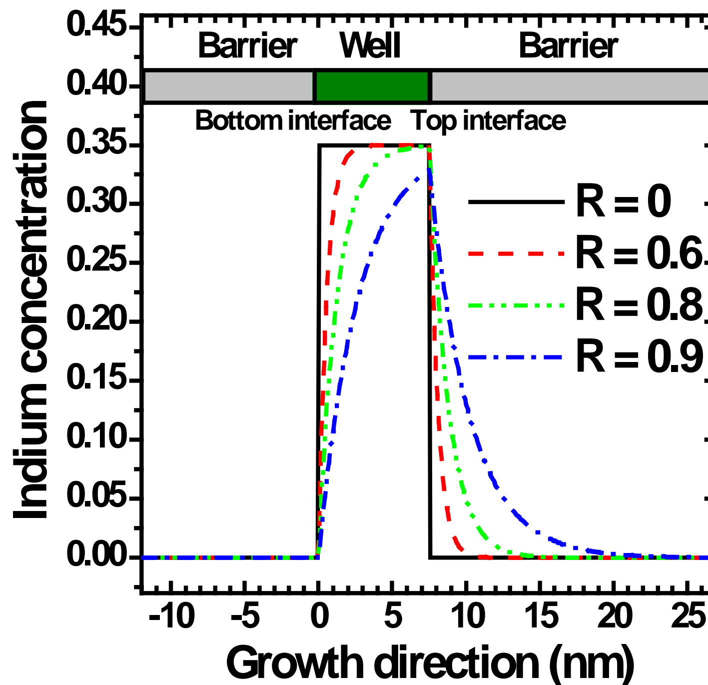

Figure 3-11: Indium segregation profile of $Ga_{0.65}In_{0.35}N_{0.015}As_{0.985}$ / GaAs single QW with different segregation efficiencies.

Figure 3-11 shows the Indium composition profiles across the $Ga_{0.65}In_{0.35}N_{0.015}As_{0.985}$ / GaAs QW modified by the segregation of Indium atoms according to Equation (3-6). For small segregation efficiency, the Indium composition maximum does not change but the transition point (between Indium < 35% and Indium = 35%) shifts towards the top interface with the increase of segregation efficiency *R*. For segregation efficiency of 0.9, the maximum of Indium composition decreases to 33%. Because the N composition does not change across the QW as described by Equation 3-7, there is a very thin Indium-poor-GaInNAs interfacial layer at the bottom region of the GaInNAs QW and a thin Indium grading GaInAs layer in the region of the top barrier close to the interface due to Indium segregation. These composition distributions result in abrupt changes in the strain at the interfaces (i.e. z = 0 and 7.5 nm) of the QW.

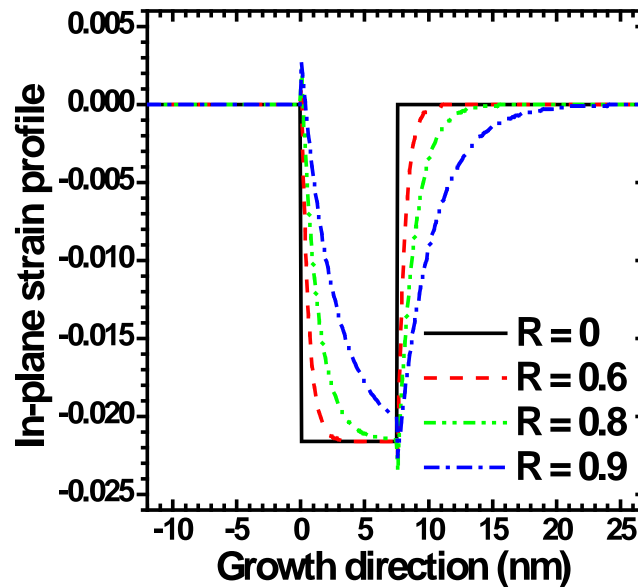

Figure 3-12: In-plane strain profile of $Ga_{0.65}In_{0.35}N_{0.015}As_{0.985}$ / GaAs QW with various Indium segregation efficiencies.

Figure 3-12 presents the in-plane strain profile across the Indium segregated QW with different segregation efficiencies. One can see that the strain profile consists of three parts; firstly, the bottom GaAs barrier that is unstrained. Secondly, the QW area that is mostly

compressively strained, and the compressive strain increases along the growth direction for certain segregation efficiency. Finally, the top barrier area close to the interface that is compressively strained due to the segregation induced GaInAs interfacial layer.

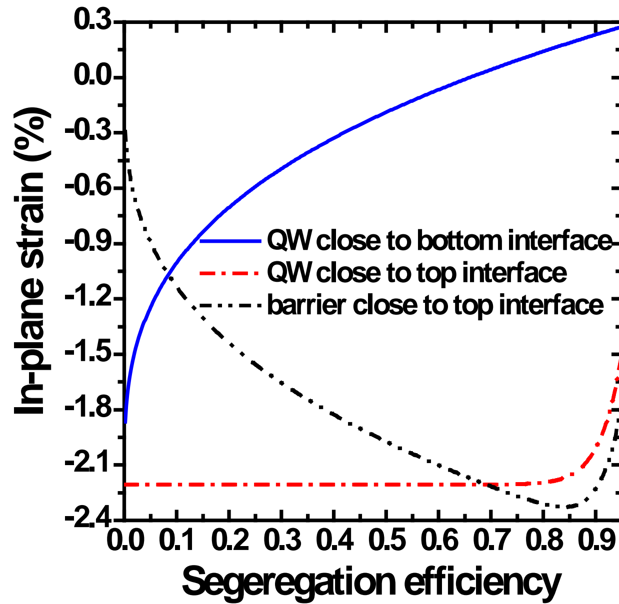

Figure 3-13: In-plane strain at the regions close to the QW / barrier interfaces as a function of segregation efficiency.

Figure 3-13 shows the in-plane strain as a function of segregation efficiency taken at the three important regions of the $Ga_{0.65}In_{0.35}N_{0.015}As_{0.985}$ / GaAs QW structure. In the first region, the QW region close to the bottom interface, the compressive strain decreases with the increase of segregation efficiency. When R = 0.66, the strain decreases to zero. Further increase of segregation efficiency leads to the sharp peak of tensile strain at the bottom interface (see Figure 3-12). In the second region, the QW region close to the top interface, the compressive strain decreases only minutely for segregation efficiency smaller than 0.84 but show a greater reduction for larger segregation efficiencies. In the third region, the barrier region close to the top interface, the compressive strain increases with the increase of segregation efficiency for $R \leq 0.84$. When R = 0.69, the compressive strain at each side of the top interface equals the other. Further increase

of segregation efficiency results in a sharp peak of compressive strain at the top interface (see Figure 3-12). However, for $R > 0.84$ the compressive strain at both sides of the top interface begins to decrease due to the decrease of the Indium composition maximum there (see Figure 3-11).

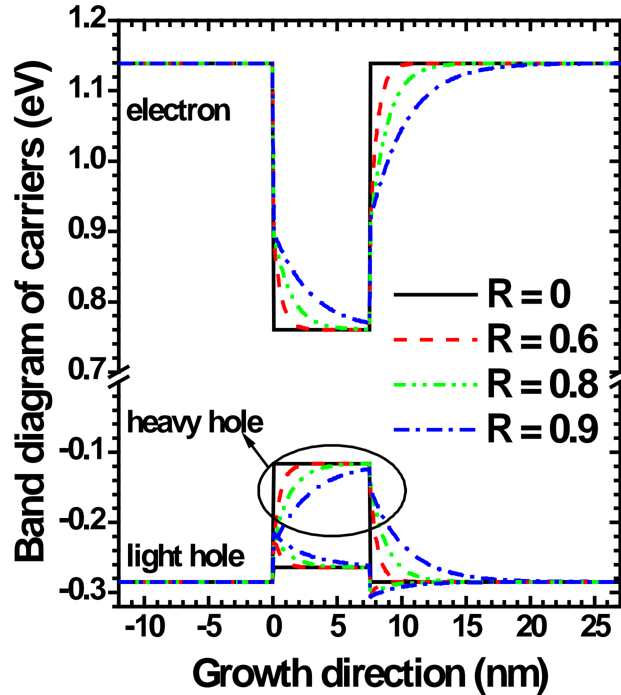

Figure 3-14: Confinement potentials of electrons in the conduction band, heavy holes and light holes in the valence band of the $Ga_{0.65}In_{0.35}N_{0.015}As_{0.985}$ / GaAs QW (λ~1.3 μm) with various segregation efficiencies of Indium atoms.

The composition and in-plane strains across the QW structures change the carrier confinement energies in the QWs. Presented in Figure 3-14 are the confinement profiles of the electrons in the conduction band and heavy and light holes in the valence band for the nominal and segregated $Ga_{0.65}In_{0.35}N_{0.015}As_{0.985}$ / GaAs QWs. The confinement profiles are determined by the variation of bulk material bandgap energy and the in-plane strain. In the QWs, moving from z = 0 nm to z = 7.5 nm, the conduction band and heavy hole band energies decrease while that of the light hole band increases. This is due to the increasing Indium composition and the

compressive strain. On the contrary, in the top barrier region, along the direction from the interface to the barrier region, the conduction band and heavy hole band energies increase while that of the light hole decreases. This band diagram results in the confinement of electrons and heavy holes in the QW near the top interface (z = 7.5 nm), and the light holes confined in the QW near the bottom interface (z = 0). Interestingly, this also suggest a space-indirect transition within the QW, between light holes localized in Indium-poor-region and electrons localized in Indium-rich region of the quantum well as shown in Figure 3-14, where we see a narrow valley for effective localization of light hole in Indium-poor-region. This is similar to the experimental observation of space-indirect transition in GaAs/GaAsN/InGaAs hetrostructure between electron localized in GaAsN layer and hole localized in InGaAs layer (Egorov 2003).

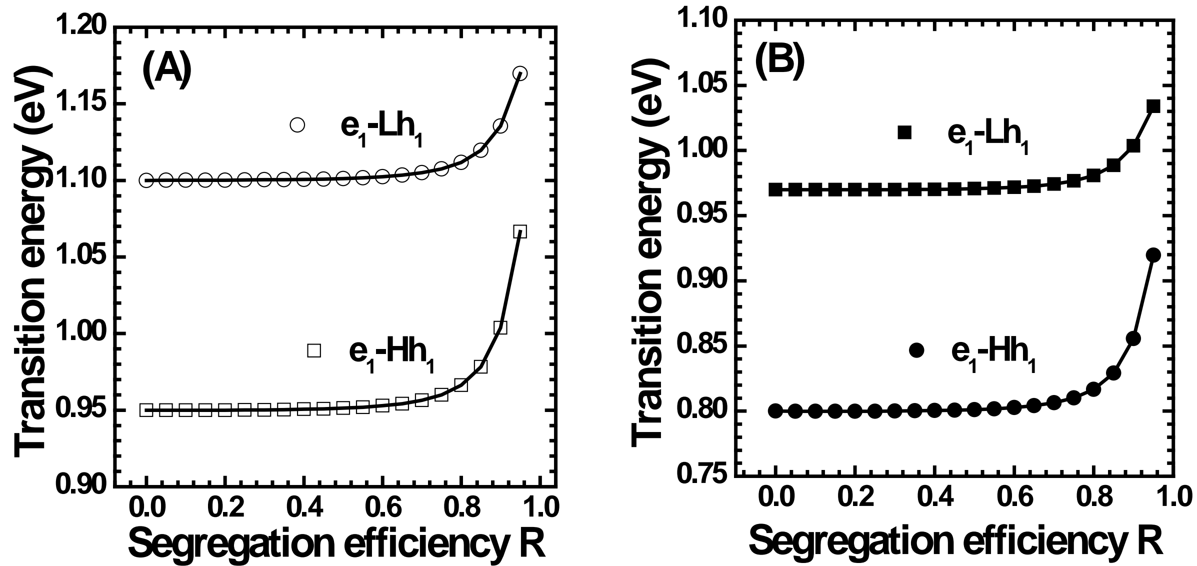

Figure 3-15: Transition energies of e_1-Hh_1 and e_1-Lh_1 in (A) $Ga_{0.65}In_{0.35}N_{0.015}As_{0.985}$ / GaAs and (B) $Ga_{0.61}In_{0.39}N_{0.03}As_{0.97}$ / GaAs QW structures as a function of Indium segregation efficiency.

The transition energies of e_1-Hh_1 and e_1-Lh_1 for the segregated QWs are obtained by solving $[\boldsymbol{H}]\times[\psi]=\boldsymbol{E}[\psi]$ using the potentials shown in Figure 3-14 as discussed in chapter 2 (section 2.2.4). Figure 3-15 shows transition energies of e_1-Hh_1 and e_1-Lh_1 as a function of

segregation efficiency for (a) $Ga_{0.65}In_{0.35}N_{0.015}As_{0.985}$ / GaAs QW (λ~1.3 μm) and (b) $Ga_{0.61}In_{0.39}N_{0.03}As_{0.97}$ / GaAs QW (λ~1.55 μm). The optical transition energies of e_1-Hh_1 and e_1-Lh_1 are approximately constant for segregation efficiencies smaller than 0.6 and 0.7, respectively, but increase for larger segregation efficiencies. The blue shift in transition energies of e_1-Lh_1 caused by Indium segregation is smaller than that of e_1-Hh_1 for $R > 0.6$, corresponding to the different effects of segregation on confinement profiles of heavy hole and light hole. It is interesting to note that the blue shift in transition energy against the segregation efficiency is the same for both QW structures in Figure 3-15. Consider that these two structures have the same strain; this observation may imply that the blue shift in transition energy due to segregation is mainly affected by strain rather than by the compositions of the QW. We may draw this conclusion because the QW materials of the two structures have the same lattice constant and different compositions, but the segregation-induced blue shifts in optical transition energies are almost the same.

3.3 Conclusion

In this chapter, Indium segregation has been studied in GaInNAs/GaAs QWs for its origin and the effect on the band structure. The origin of Indium segregation has been studied using a kinetic model, where the effect of Nitrogen is explained in terms of activation energy barrier lowering for Gallium/Indium exchange across surface and layer underneath (bulk) group-III sites.

The effect of Indium segregation on band structure and transition energy is studied for GaInNAs / GaAs single QWs emitting at 1.3 μm wavelength. Constant segregation efficiency for both the well and barrier were used to model the composition profile. The optical transition

energies were numerically calculated for the QWs with various segregation efficiencies of Indium atoms. The results indicate that the transition energy starts to blue shift for segregation efficiencies larger than 0.6, which is mainly affected by the strain rather than by the composition in the QW. We also show a space-indirect transition between light holes localized in Indium-poor-region and electrons localized in Indium-rich-region of the quantum well. Our calculations suggest that photoluminescence is a powerful tool for the investigation of segregation with the efficiencies larger than 0.7, but loses their reliability in the case of segregation efficiency smaller than 0.7.

Chapter 4: Effect of Composition Disorder on Optical Gain

The growth of complex heterostructures such as QWs, superlattices, or graded heterojunctions requires high quality materials with uniform composition and ideal interfaces. However, in actual growth there are several factors which affect the composition profile taking it far from ideal. For example, in the last chapter Indium segregation (Indium composition disorder) was studied and shown to have significant effect on bandstructure and transition energies of GaInNAs/GaAs QWs. For GaInNAs/GaAs QWs, apart from Indium segregation there is non-uniformity in Nitrogen profile (Nitrogen composition disorder). Moreover, it is known that incorporation of Nitrogen atoms tends to enhance the Indium segregation during the growth of GaInNAs/GaAs QW (Liu 2006[4]; Luna 2007).

Composition disordering in GaInNAs/GaAs QWs has also been reported to significantly affect structural and optical properties including gain spectrum of TE and TM modes (Moison 1989; Schowalter 2006; Chan 2002). Segregation induced asymmetric composition profile combined with the non-linear band anticrossing interaction (of GaInAs conduction band and higher-lying Nitrogen resonant band) modifies the carrier confinement and the transition energies and hence affects the optical gain characteristics significantly (Liu 2006[1]; Schowalter 2006).

In this chapter, a detailed theoretical analysis of composition disorder in GaInNAs/GaAs single QW is presented. The effects of the composition disorders of Indium and Nitrogen, in a

GaInNAs/GaAs single-QW along the growth direction, on the QW's band structure and further on its optical gain spectrum have been studied theoretically.

4.1 QW Structure

In this study, the disordered composition profiles are taken from experimental results of the MBE grown GaInNAs/GaAs QWs reported by Luna *et al.* (Luna 2007). The QW consists of a 7-nm-thick $Ga_{0.59}In_{0.41}N_{0.038}As_{0.962}$ QW sandwiched by 30-nm GaAs barriers. The nominal Indium and Nitrogen compositions in the QW are 0.41 and 0.038, respectively, which correspond to an emission wavelength of 1.55 μm.

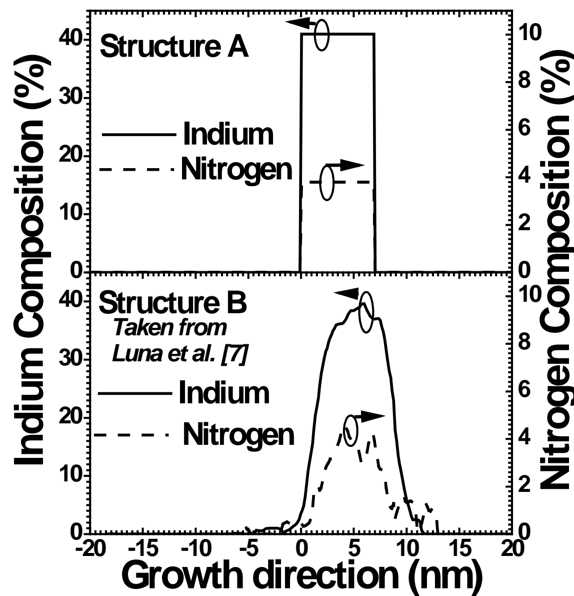

Figure 4-1: Indium and Nitrogen composition profiles for a 7-nm-thick $Ga_{0.59}In_{0.41}N_{0.038}As_{0.962}$/GaAs QW without disorder (structure A, nominal structure with uniform compositions and ideal interfaces) and with disorder (structure B, taken from the experimental results reported in (Luna 2007) with author's permission).

In order to study the effect of composition disorder, we compare the nominal structure with the composition disordered structure. The nominal structure, hereafter referred to as structure A, consists of uniform composition profiles of Indium and Nitrogen in the QW and

abrupt (ideal) interfaces. The composition disordered structure, hereafter referred to as structure B, has non-uniform Indium and Nitrogen composition profiles in the QW. The interfaces are not abrupt. The disordered composition profiles of structure B are taken from experimental results of the MBE grown GaInNAs/GaAs QWs (at 460^0C) reported by Luna *et al.*(Luna 2007). Figure 4-1 shows the Indium and Nitrogen composition profiles in the two structures.

4.2 Strain and carrier confinement profile

Based on these composition profiles, we can calculate the in-plane strain profiles (as explained in section 2.2.1).

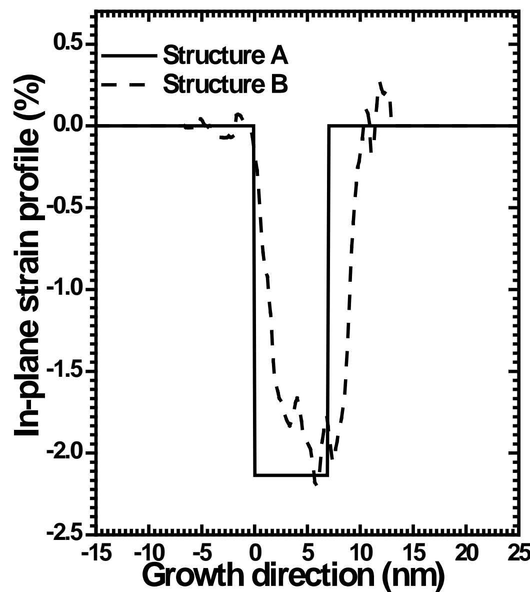

Figure 4-2: In-plane strain profiles of a 7-nm-thick $Ga_{0.59}In_{0.41}N_{0.038}As_{0.962}$/GaAs QW for structures A and B.

Figure 4-2 presents the in-plane strain profiles across the nominal and the composition disordered QWs. For structure A, two regions can be identified: unstrained GaAs barrier and compressively strained GaInNAs QW. For structure B, the strain profile consists of three parts: firstly, the bottom GaAs barrier that is unstrained; secondly, the QW area that is compressively

strained; and finally, the top barrier area close to the interface that is tensile strained. Indium and Nitrogen disorders modify the composition and the in-plane strain across the QW structures, which in turn change the carrier confinements for the GaInNAs QW.

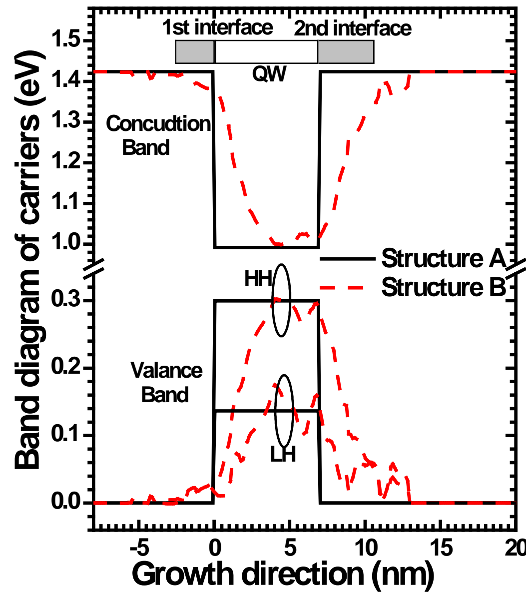

Figure 4-3: Confinement potentials of electrons in the conduction band, heavy holes and light holes in the valence band for structures A and B.

Figure 4-3 presents the confinement profiles of the carriers in the conduction band and valence band (HH and LH) for the structures A and B. The confinement profiles are determined by the variation of bulk material bandgap energy and the in-plane strain. The confinement profiles in structure B show narrow valleys that become broader for higher order quantization. The QW (in both the structures) is compressively strained and thus the valence band is split into HH and LH, where the HH band is pushed up and the LH band is pulled down. Figure 4-3 also shows small fluctuations in the potential profiles which indicate a significant possibility of carrier traping in the GaInNAs QWs. The experimental report confirms the existence of random potential fluctuations due to Nitrogen, which dominate the PL properties at low temperatures

(Nomuraa 2005). These potential fluctuations persist even after annealing and are responsible for carrier trapping for temperatures up to 100 K (Khee 2005).

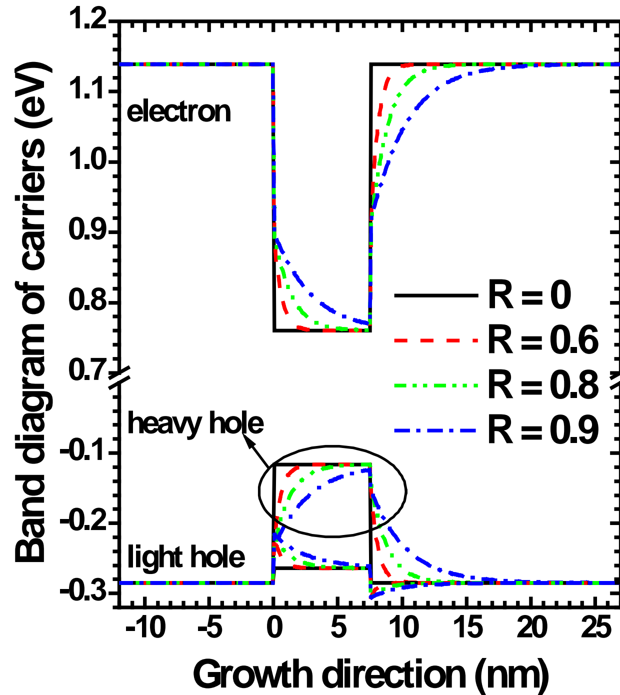

Figure 4-4: Confinement potentials of electrons in the conduction band, heavy holes and light holes in the valence band of the $Ga_{0.65}In_{0.35}N_{0.015}As_{0.985}$ / GaAs QW with various segregation efficiencies of Indium atoms without considering Nitrogen disorder.

To separate the effects of Indium and Nitrogen disorders we refer to the last chapter where effect of Indium segregation (Indium-disorder modeled using Muraki model) was discussed while the Nitrogen profile was assumed to be abrupt. Figure 4-4 presents the carrier confinement profiles without taking the Nitrogen disorders into account. This result is similar to the one presented in section 3.2.5. The light holes and heavy holes are confined towards the first and the second interfaces, respectively, while the electrons are confined towards the second interface. This implies a smaller probability for *e-lh* transition. However, when Nitrogen disorder is involved as in structure B in Figure 4-3, both the light holes and heavy holes are confined towards the second interface within the QW. This shows that the Nitrogen disorder tends to

enhance the *e-lh* transition probability. This is attributed to the enhancement of tensile strain due to Nitrogen (Park 2004), which is further magnified by the tendency of Nitrogen to hinder Indium incorporation resulting in higher Nitrogen and smaller Indium compositions locally, i.e., higher tensile strain (Rubini 2006).

4.3 Band dispersion

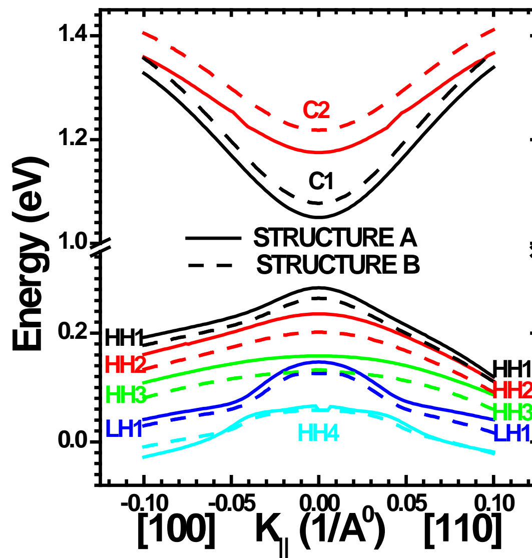

Figure 4-5: Energy dispersion curves for conduction and valence subbands along [100] and [110] crystal directions for structures A and B.

Figure 4-5 shows the energy dispersion curves for conduction and valence subbands for structures A and B. The envelope function associated with each subband varies with the wave vector in the plane of the QW ($k_{//}$) due to subband coupling giving rise to non-parabolicity. The subband states are labeled as Cn, HHn and LHn (n = 1, 2, 3, 4) according to their dominant characteristics at $k_{//}= 0$. The two conduction subbands are designated as C1 and C2, and the five valence subbands are designated as HH1, HH2, HH3, LH1, and HH4. C1 and HH1 are the ground states for electrons and holes, respectively. The calculated subbands look asymmetric along [110] and [100], specialy for HH1 and HH4, which could be due to different effective

masses along these two directions. The subbands for structures B are pulled down from the valence-band-edge and pushed up from the conduction-band-edge as compared with the structure A. This is due to the narrower confinement valley for structure B, which makes the quantization energies larger. However, for higher order subbands, in structure B, valley gets broader (see Figure 4-3) and HH4 shows a reverse trend for higher $k_{||}$ (shifting up for structure B as compared with structure A). Due to the broadening of the valley for higher order subbands, energies are closely spaced compared to the nominal QW, i.e., the separation between HH4 and HH3 is smaller for structure B than that of structure A. Interestingly, for structure B, the third (HH3) and fourth (LH1) valence subbands overlap at $k_{||}=0$, which results in enhancement of electron-light hole transitions. The band structure also shows non-parabolicity, resulting from band coupling which changes the in-plane carrier masses.

4.4 Effect of Nitrogen disorder on transition energy

In order to separate the effects of Indium and Nitrogen disorders on optical properties, we compare the effect of Indium segregation for two types of QWs, one with a uniform Nitrogen composition profile and the other with disordered Nitrogen composition profile. The segregated Indium composition is calculated using the Muraki model (Muraki 1992)

$$x_n = \begin{cases} x_0\left(1 - R^n\right), & \left(1 \le n \le N, well\right) \\ x_0\left(1 - R^N\right)R^{n-N}, & \left(N < n,\ barrier\right) \end{cases} \tag{4-1}$$

where n is the number of monolayers, x_0 is the nominal Indium composition (0.41 here), N is QW thickness in monolayer, and R is the segregation efficiency.

Figure 4-6 shows the increase in transition energy (blueshift) due to Indium segregation for uniform and disordered Nitrogen composition profiles. The blueshift for structure B is shown

as solid round dot, which corresponds to segregation efficiency R= 0.8 (Luna 2007). The solid diamond represents the ideal structure A without Indium and N disorder. From Figure 4-6, the maximum difference in blueshift energy is only 7 meV between the two curves at any segregation efficiency. This implies that certain Nitrogen disorder plays only a minor role in the blueshift caused by Indium segregation. One can also see that for both cases (with uniform and disordered Nitrogen compositions), the blueshift is negligible for segregation efficiencies R < 0.6, after which blueshift increases rapidly with Indium segregation.

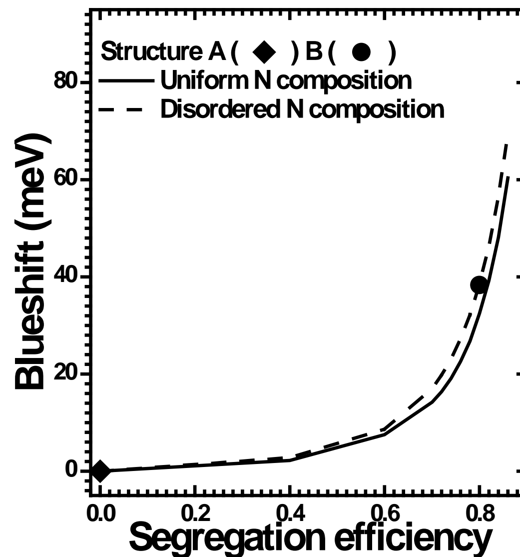

Figure 4-6: The increase of electron-heavy hole (C1-HH1) transition energies (blueshift) as a function of Indium segregation efficiency for structures A and B.

4.5 Optical gain

In the optical gain calculation, the first five valance subbands and two conduction subbands have been used as there is negligible contribution from higher order subbands to the optical gain. The optical gain has been calculated using the method described in section 2.2.5. The optical gain of the transverse electric (TE) and transverse magnetic (TM) modes of the GaInNAs/ GaAs segregated QWs are shown in Figure 4-7 and Figure 4-8, respectively.

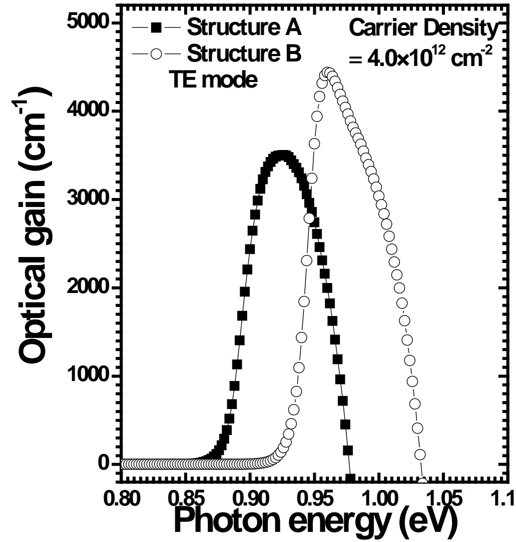

Figure 4-7: Optical gain spectra of the TE mode of the $Ga_{0.59}In_{0.41}N_{0.038}As_{0.962}$/GaAs QW as a function of photon energy for structures A and B.

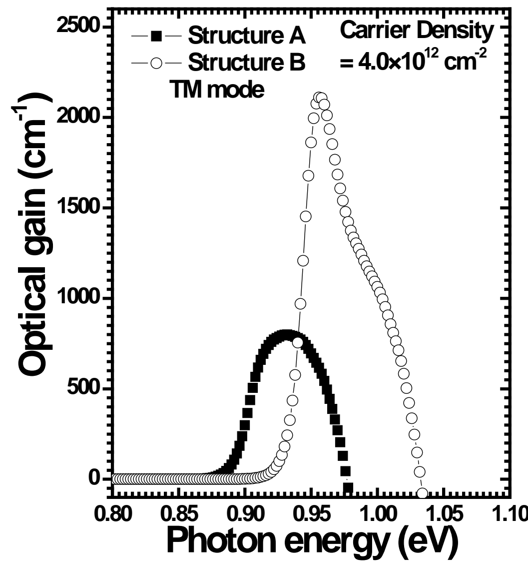

Figure 4-8: Optical gain spectra of the TM mode of the $Ga_{0.59}In_{0.41}N_{0.038}As_{0.962}$/GaAs QW as a function of photon energy for structures A and B.

The injected carrier density is set to be 4.0×10^{12} cm^{-2}. For compressive-strained GaInNAs/GaAs QW structure A, the first three valence subbands are heavy-hole bound states. Consequently, the gain of the TE mode is much larger than that of the TM mode, as reported in experimental measurements by Kvietkova *et al.* (Kvietkova 2005), and Hofmann *et al.* (Hofmann 2002). Hofmann *et al.* used 1.9 % Nitrogen and reported higher TM mode gain than

that was reported by Kvietkova who used only 0.1% Nitrogen composition. The higher TM mode gain is due to higher Nitrogen composition which increases tensile strain. Since in our case the Nitrogen composition is almost double to that of Hofmann *et al.*'s, therefore we can expect even higher TM mode gain compared to the experimental reports of Hofmann *et al.*. For structure B, the gain spectra shift towards the higher photon energy in comparison to structure A. As shown in Figure 4-7 and Figure 4-8, the gain peak energy shifts caused by the N disorder are 36 and 26 meV for the TE and TM modes, respectively. Likewise, the optical gains are increased by 27% and 162% for the TE and TM modes, respectively. The larger increase in the optical gain of the TM mode is due to the change in the third valence subband, which is HH for structure A and an overlap of HH3 and LH1 for structure B. The increase in TM mode optical gain is also due to the enhancement of *e-lh* transition probability as discussed earlier (Park 2004).

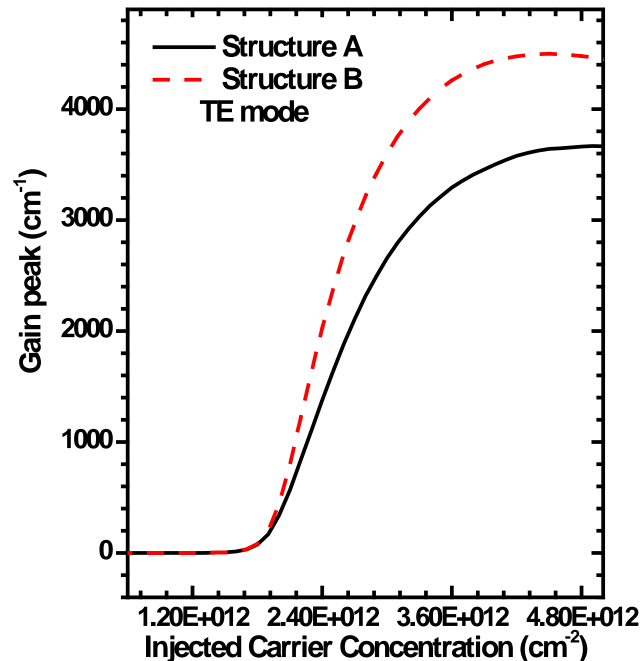

Figure 4-9: Optical gain peak of the TE modes of the $Ga_{0.59}In_{0.41}N_{0.038}As_{0.962}/GaAs$ QW as a function of the injected carrier concentration for structures A and B.

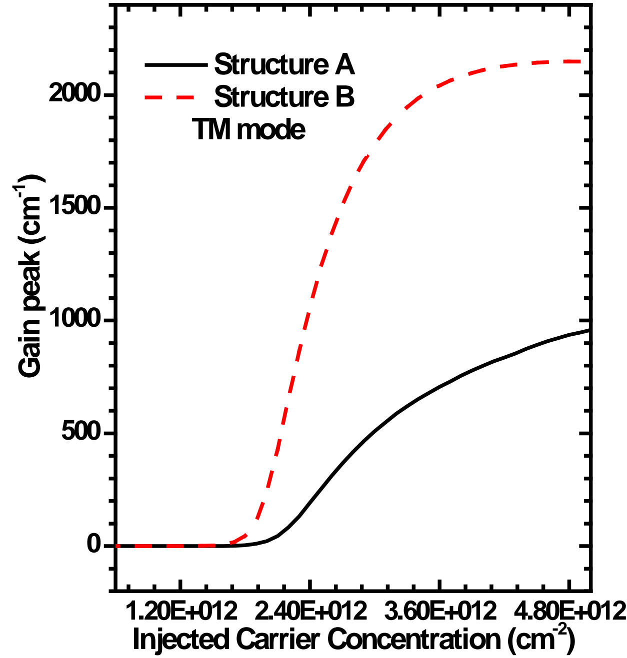

Figure 4-10: Optical gain peak of the TM modes of the $Ga_{0.59}In_{0.41}N_{0.038}As_{0.962}$/GaAs QW as a function of the injected carrier concentration for structures A and B.

Figure 4-9 and Figure 4-10 show the gain peak values of the TE and TM modes respectively as a function of the injected carrier concentration for structures A and B. For structures A and B, gain peaks for TE and TM modes increase monolithically with injected carrier concentration. The threshold carrier density for TE mode is 2×10^{12} cm^{-2} in both the structures A and B. The threshold carrier density for TM mode is 2×10^{12} cm^{-2} for structure A and 1.5×10^{12} cm^{-2} for structure B. This supports the idea that disordered structure has significant increase in the TM mode gain.

The radiative current density can be calculated from the emission spectrum using $J_{rad} = et_w\hbar\int R_{sp}(\hbar\omega)d\omega$, as described in section 2.2.5. The calculated radiative current density only takes into account the carrier injection contributing to the radiation. Figure 4-11 and Figure 4-12 show the gain values at the peaks of the TE and TM modes respectively, as a function of the

radiative current density for structures A and B. It is seen that the gain peaks also increase with radiative current density.

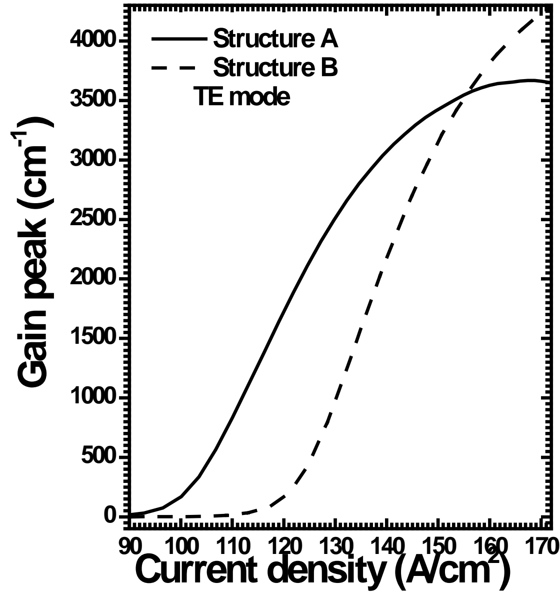

Figure 4-11: Optical gain peak of the TE modes of the $Ga_{0.59}In_{0.41}N_{0.038}As_{0.962}$/GaAs QW as a function of the radiative current density for structures A and B.

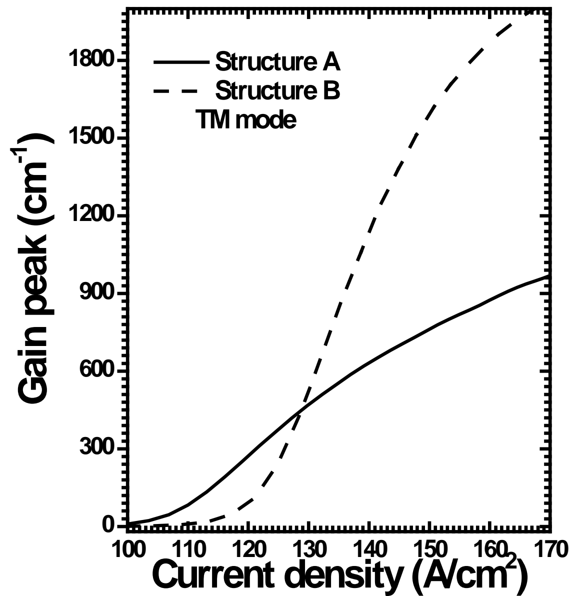

Figure 4-12: Optical gain peak of the TM modes of the $Ga_{0.59}In_{0.41}N_{0.038}As_{0.962}$/GaAs QW as a function of the radiative current density for structures A and B.

The threshold current densities of both the TE and TM modes can be determined from Figure 4-11 and Figure 4-12, they are 100 A/cm^2 (for both the TE and TM modes) for structure A and 120 A/cm^2 (for both the TE and TM modes) for structure B. Interestingly, for TE mode the injected carrier density is same for structures A and B but structure A has smaller threshold radiative current density. This is due to the shape of the spontaneous emission spectrum which requires larger current desnity to achieve same carrier concentration in structure B. Structure B shows a higher threshold current density for both the TE and TM modes as compared with structure A. The calculated values of the threshold current density are quite close to the best experimental values of GaInNAs (130 A/cm^2) reported in the literature (Zhao 2008). The small difference is due to not considering confinement factor and optical loss in our simulations.

4.6 Conclusion

In conclusion, optical gain characteristic of QW structures with uniform Indium and Nitrogen composition profiles were compared with the real experimental composition profiles. The subband energy dispersion and optical gain were numerically calculated for the QWs. Both the Indium and N disorders can cause the blueshift in transition energy, but Indium disorder plays the major role. The disorder also enhances the TM mode optical gain, especially at high carrier densities. However, threshold carrier density for the TE mode is same in both the disordered structure and the nominal structure. These results may provide important information in the design and fabrication of GaInNAs/GaAs based optoelectronic devices.

Chapter 5: Thermal Annealing Induced Blueshift

MBE growth of GaInNAs is carried out at low temperature (< 480 ^{O}C) to improve the solubility of Nitrogen in GaInAs and to avoid phase separation of GaInNAs into GaInAs and GaN (Chalker 2004). However, this leads to a high defect density in the crystal and poor photoluminescence (PL) properties. Post-growth thermal annealing is used to remove the defects. Although rapid thermal annealing (RTA) improves the PL efficiency of the GaInNAs / GaAs quantum wells (QWs), it also causes an undesirable blueshift. This blueshift has been attributed to Gallium/Indium interdiffusion across the QW interface (Ng 2005) and reorganization of the Nitrogen-bonding configuration, $N\text{-}In_mGa_{4-m}$ ($0 \leq m \leq 4$), in short range order (SRO) clusters (Pan 2000; Tournie 2002; Liu 2006[3]). Klar *et al.* (Klar 2001) attributed the blueshift to the SRO mechanism and explained that the rearrangement of Nitrogen-bonding configuration forms five discrete sets of bandgap corresponding to $N\text{-}In_0Ga_4$, $N\text{-}In_1Ga_3$, $N\text{-}In_2Ga_2$, $N\text{-}In_3Ga_1$, and $N\text{-}In_4Ga_0$ phases in GaInNAs. Similar conclusions were reported by Tournie *et al.* (Tournie 2002), where post-annealing PL measurements from GaInAs and GaAsN did not show any blueshift but from GaInNAs it showed a blueshift of 67 meV. In Tournie's experiments, X-ray diffraction (XRD) measurements and transmission electron microscopy (TEM) did not show any compositional change in GaInNAs indicating the reorganization of N-bonding configuration. There are several reports separately explaining these two phenomena but lack the quantitative

contribution from both. In this work we try to understand and explain the individual contributions of SRO and interdiffusion.

In this chapter, we present a detailed analysis of PL blueshift mechanism in an MBE-grown GaInNAs/GaAs single QW. PL peak wavelengths from the QW were measured for annealing temperatures of 680-800 ^{0}C and annealing time up to 3 hours. Experimental PL blueshift was analyzed for individual blueshift components due to the reorganization of the N-bonding configuration and the Gallium/Indium interdiffusion across the QW interfaces, using a linear model and a genetic algorithm-based approach. In section 5.1, experimental procedures are briefly described. In section 5.2, analysis of photoluminescence blueshift using a linear model is described. In section 5.3, the PL blueshift as a combined effect of SRO and interdiffusion is analyzed using genetic algorithm based approach. Finally, in section 5.4, conclusion is presented.

5.1 Experiment

The QW structure analyzed in this study was an 8-nm $Ga_{0.628}In_{0.372}N_{0.015}As_{0.985}$/GaAs single QW grown by solid-source MBE on GaAs (100) substrate. Nitrogen was produced by a radio-frequency (RF) plasma source. The QW was sandwiched between the 500-nm GaAs buffer and 100-nm GaAs cap layers. The growth temperature of the QW was 460 °C. The GaAs buffer and cap layers were grown at 580 °C. After the growth, the as-grown wafer was cut into small pieces and the small pieces of samples were repeatedly annealed in a Nitrogen atmosphere of a rapid thermal annealing (RTA) chamber at temperatures of T_{ann} = 680, 700, 750, and 800 °C, for few seconds to several hours . There were no extra dielectric capping layer on top of the samples, but the samples were covered by a GaAs wafer during the annealing. After the annealing, the PL spectra were measured at room temperature using an Accent Rapid Photoluminescence Mapping

System (RPM 2045) with a He-Cd laser (325nm) as the excitation light source. We did not do the wafer mapping but the measured PL from four pieces of as-grown samples showed up to ±36 meV difference, which is much smaller then the observed PL blueshift.

5.2 Linear model based approach

PL blueshift has been attributed to the phenomenon of Gallium/Indium interdiffusion by Ng *et al.* (Ng 2005). However, blueshift only considering the interdiffusion tends to overestimate the extent of diffusion. In this section we show that this blueshift is actually a combination of the two phenomena including Gallium/Indium interdiffusion and short-range-order.

5.2.1 Interdiffusion model

In order to model blueshift, first of all we construct the interdiffusion model by solving Fick's second law of diffusion. For a square quantum well the composition profile of diffusing species is given as

$$C(z) = (C_0/2)\left[erf\,\frac{w_0+2z}{4L_D} + erf\,\frac{w_0-2z}{4L_D}\right] \tag{5-1}$$

where *erf* is the error function, C_0 is the initial Indium composition, w_0 is the thickness of the as-grown QW, and z is the distance in the growth direction with z = 0 at the well center. The Indium composition profile is characterized by a diffusion length $L_D = \sqrt{D_0 \exp(-E_a / kT_{ann}) t_{ann}}$, where D_0 is diffusion constant, E_a is the activation energy for diffusion, k is the Boltzmann constant, T_{ann} is the annealing temperature and t_{ann} is the annealing time. The composition profile is used to determine the strain profile and resulting potential profile for various subbands (conduction, heavy hole and light hole bands) and $E_{e1\text{-}Hh1}$ transition energies.

The interdiffusion across the QW/barrier interfaces affects the characteristic PL energy by changing the effective width of the well and, therefore, the energy of the confined levels. This also modifies the well composition and band gap energy. For GaAs based materials, such as GaInAs and GaInNAs, the conduction and valence bands are decoupled. The minimum in the conduction band occurs at symmetrical Γ_6 valley. The energy states and wave function of the electron, heavy-hole and light-hole at Γ_6 can be calculated using the Duke-Daniel model. A detailed description of this procedure is given in section 2.2.4. We accommodate lattice mismatch by including biaxial in-plane strain and uniaxial shear strain after interdiffusion. The uniaxial shear strain results in hole-splitting, which pushes up the heavy-hole energy states. The calculated confinement profiles of electrons and heavy holes with various diffusion lengths have been used to find the ground state transition energy.

For the 8-nm $Ga_{0.628}In_{0.372}N_{0.015}As_{0.985}$ / GaAs QW structure, the transition energy between the first confined states of electron and heavy-hole, E_{e1}-H_{h1}, as a function of diffusion length is shown in Figure 5-1a. Figure 5-1b displays the squared-diffusion-length dependence of E_{e1}-H_{h1}. The XRD measurements (Liu 2006) and simulations indicate that the diffusion lengths are smaller than 2 nm in this study. As evident from Figure 5-1b, within the range of 0-4 nm^2 the numerically calculated transition energy, E_{e1}-H_{h1}, increases linearly with L_D^2, and can be well fitted by $E_{e1-Hh1} = E_0 + A \times Dt$ with E_0 = 0.9145 eV and A = 0.032 eV/nm^2.

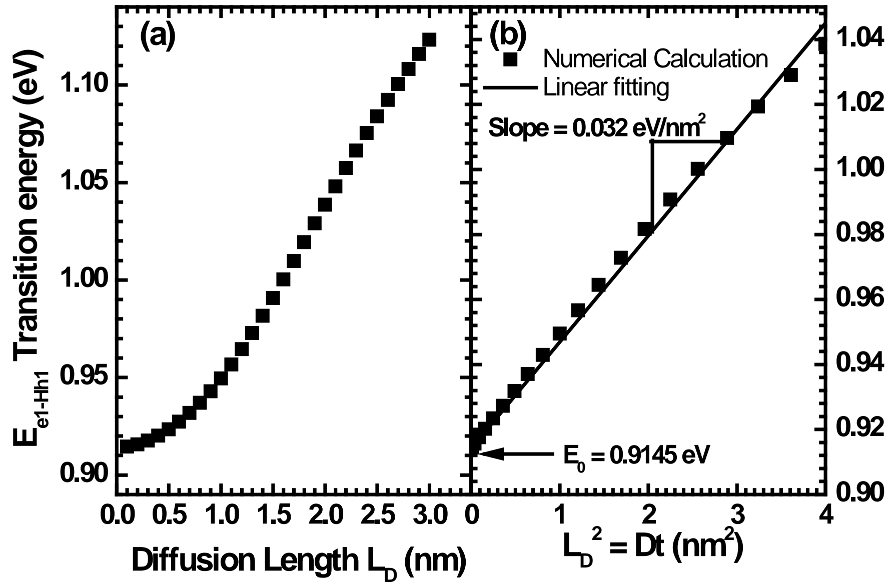

Figure 5-1: Numerically calculated transition energy between the first confined states of electron and heavy-hole (a) as a function of diffusion length, and (b) as a function of squared-diffusion-length, the solid-line is a linear fitting for the calculated data.

5.2.2 Linear model

In section 5.2.1 we established that blueshift due to interdiffusion varies linearly with the squared diffusion length, i.e., annealing time. We have shown that considering the interdiffusion only would over-estimate the extent of interdiffusion (Liu 2006; Ng 2005). This over estimation is particularly significant during the early stage of annealing. Figure 5-2 shows the blueshift in GaInNAs/GaAs samples where two regions (abrupt and linear) can be easily identified. This abrupt blueshift has also been observed in GaInAs / GaAs QWs, and interpreted as an effect of strain-induced interdiffusion (Gillin 1993). The PL blueshift at the initial stage of annealing the GaInNAs / GaAs QW is faster than that of the GaInAs / GaAs QW grown at the same conditions with the same well width and Indium composition. The compressive strain in the GaInNAs / GaAs QW is then definitely smaller than that in the GaInAs / GaAs QW. This comparison reveals that in GaInNAs / GaAs QW, the effect of strain-induced interdiffusion on the PL

blueshift at the initial annealing stage is much less pronounced than that of SRO. Because of a lack of knowledge of the annealing time dependence of blueshift due to SRO, ΔE_{SRO}, combined with the fact that blueshift due to interdiffusion varies linearly with annealing time, $E_{PL} = \Delta E_{SRO} + E_0 + A \times Dt_{ann}$ has been used to fit the PL blueshift in the linear region after abrupt blueshift.

5.2.3 Results and discussion

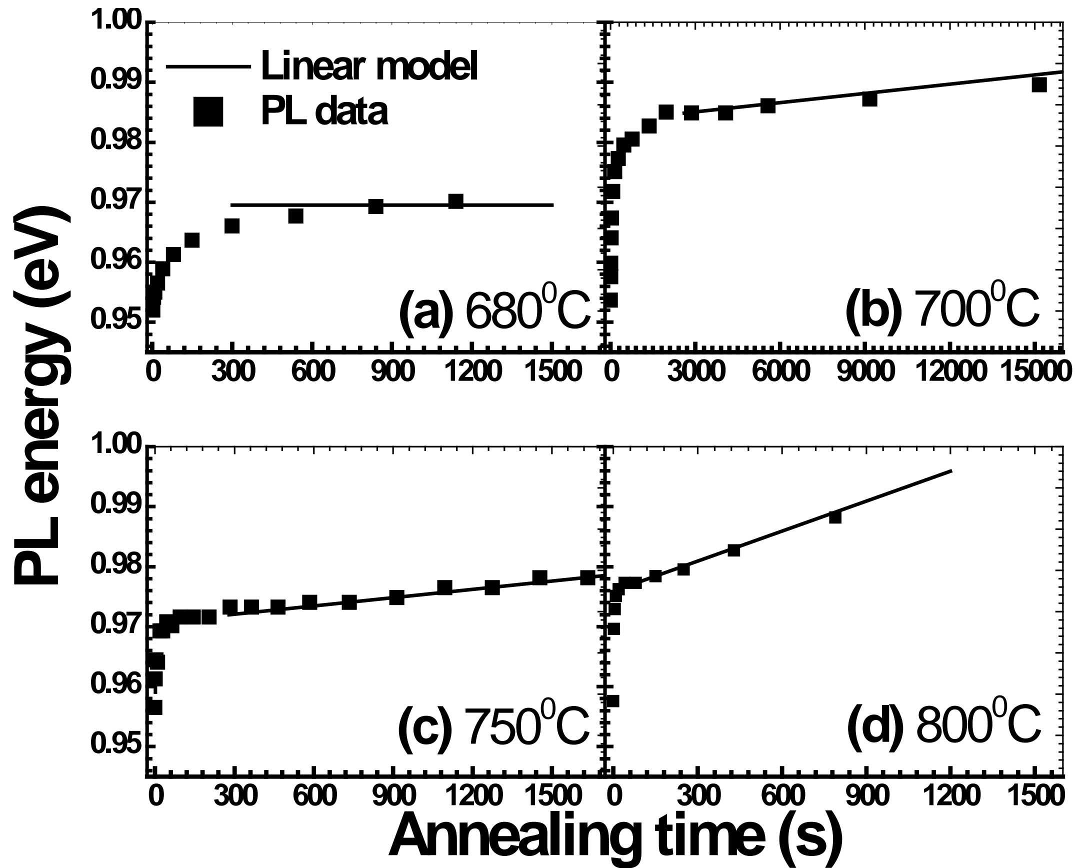

Figure 5-2: Photoluminescence peak energy as a function of annealing time annealed at 680 ^{0}C (a), 700 ^{0}C (b), 750 ^{0}C (c), and 800 ^{0}C (d). The solid lines are the best fittings by using $E_{PL} = \Delta E_{SRO} + E_0 + A \times D\ t$, with E_0 = 0.9145 eV and A = 0.032 eV/nm^2.

Figure 5-2 shows the photoluminescence peak energy for 8-nm $Ga_{0.628}In_{0.372}N_{0.015}As_{0.985}/GaAs$ QW as a function of annealing time for annealing temperatures

680 ^{0}C (a), 700 ^{0}C (b), 750 ^{0}C (c), and 800 ^{0}C (d). The solid lines are the best fittings by using $E_{PL} = \Delta E_{SRO} + E_0 + A \times D\,t$, with E_0 = 0.9145 eV and A = 0.032 eV/nm^2. The data used for the best fitting are summarized in Table 5-1. It is found that the ΔE_{SRO} is over a range of 18~28 meV, which shows a highest value for 700 ^{0}C and smallest value for 800 ^{0}C annealing temperature. Comparison between the theoretical E_0 = 0.9145 eV and the PL energy of the as-grown sample (0.9520 eV) reveals that the ΔE_{SRO} caused by '*self annealing*' is about 37.5 meV. The relatively smaller diffusion coefficients obtained (see Table 5-1), as compared with those reported in GaInAs /GaAs, GaAs / AlGaAs QW structures, is due to the relatively lower annealing temperature studied here (Ryu 1995; Choe 1998).

Table 5-1: The best fitting values of the diffusion coefficient D and the SRO effect ΔE_{SRO} for the photoluminescence energy blueshifts.

Annealing Temperature T_{ann} (^{o}C)	D ($\times 10^{-18}$ cm^2/s)	ΔE_{SRO} (meV)
680	0.03	20
700	0.10	28
750	0.97	23
800	3.52	18

From the data presented in table 5-1, the Arrhenius plot has been constructed according to $D = D_0 e^{-(E_A/kT_{ann})}$ as shown in Figure 5-3. It can be seen that the activation energy E_A for interdiffusion is 3.25 eV. This activation energy value is considerably larger than those (~0.6 eV) obtained by *Ng et.al.*, where the annealing time durations considered are not longer than 30 s. Within this annealing time range, as we discussed above, the PL blueshift is mainly caused by SRO, and shows a faster blueshift behavior than the real interdiffusion. The pre-exponential factor of D_0 obtained from the Arrhenius plot is 5.88$\times 10^{-3}$ cm^2/s.

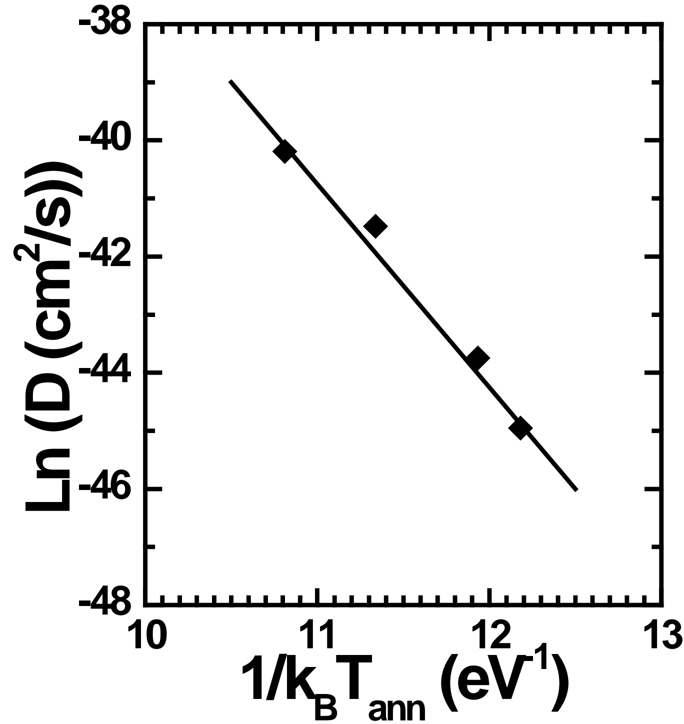

Figure 5-3: An Arrhenius plot of GaInNAs / GaAs interdiffusion coefficients for temperatures between 680 and 800 ^{0}C.

The fitting by the linear model gives the clue about SRO blueshift and identifies the time and temperature during which blueshift is dominated by interdiffusion. However, this model ignores the time dependence of the blueshift due to SRO and separately fits the blueshift for different annealing temperatures which does not consider the activation energy of SRO. Therefore, in next section we consider another model based on genetic algorithm which tries to overcome these limitations.

5.3 Genetic algorithm based approach

In the section 5.2, we have concluded that SRO is a dominant mechanism for short time annealing and Gallium/Indium interdiffusion is a dominant mechanism for long time annealing. There are several reports studying the Gallium/Indium atoms interdiffusion induced PL

blueshifts, very limited studies of blueshift caused by the SRO have been reported, particularly the time dependence of blueshift due to SRO (Dixit 2008). In this section, we model the time dependence of short range order and do the comprehensive analysis of the photoluminescence blueshift using the genetic algorithm.

5.3.1 Short Range Order

Incorporation of Nitrogen into GaInAs forms Nitrogen-localized state, E_N (Duboz 2002). E_N changes with the Nitrogen-bonding configuration and Indium composition, which has been described earlier (section 2.2.2). As the Nitrogen-bonding configurations change from Gallium-rich to Indium-rich E_N increases which increases the bandgap energy of GaInNAs (Klar 2001). Here, we analyze the effect of different N-bonding configurations on interdiffusion induced blueshift using band anticrossing model (described in section 2.2.2). Here, we analyze the blueshift due to interdiffusion, while assuming same Nitrogen-bonding configuration, for each of the five possible Nitrogen-bonding configurations. Figure 5-4 shows the numerically calculated Gallium/Indium interdiffusion induced blueshifts in $E_{e1\text{-}Hh1}$ as a function of diffusion length for different Nitrogen-bonding configurations. It is clearly seen from Figure 5-4 that when the diffusion length is shorter than 2 nm, the effect of Nitrogen-bonding configuration is insignificant on the interdiffusion induced blueshift. QW with more Gallium neighbors in N-bonding configuration shows higher interdiffusion induced blueshift, as shown in Figure 5-4, particularly significant for diffusion lengths larger than 2 nm. This can be attributed to the stronger interaction of Nitrogen localized state, E_N, with GaInAs conduction band, resulting in a different blueshift for different N-bonding configurations. For Gallium rich N-bonding configuration, E_N is closer to the conduction band. Interdiffusion decreases Indium composition

in the QW, particularly for longer diffusion lengths. This strengthens the interaction between E_N and the GaInAs conduction band (Duboz 2002).

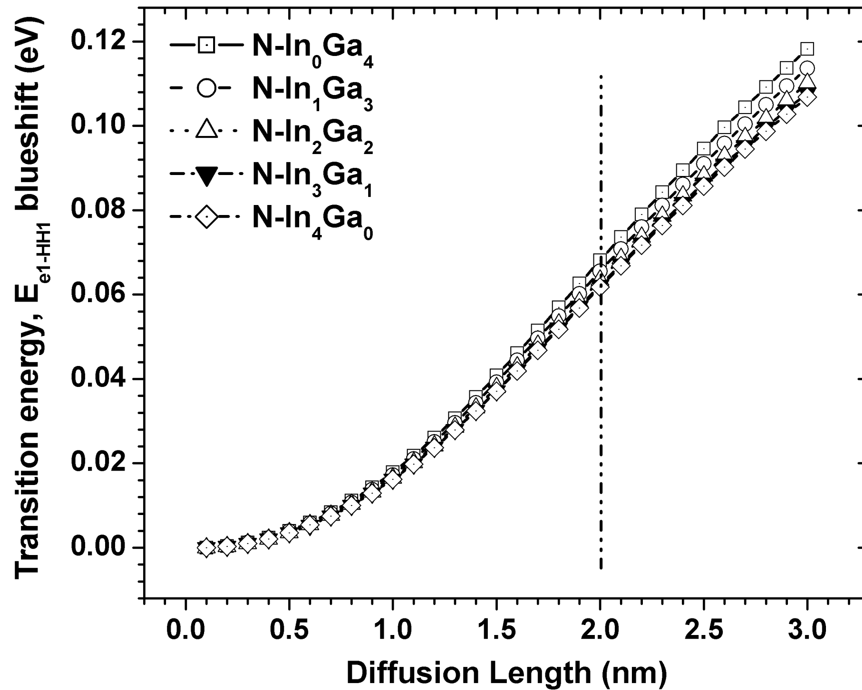

Figure 5-4: Blueshift in transition energy, Ee1-Hh1, of an 8-nm $Ga_{0.628}In_{0.372}N_{0.015}As_{0.985}$ / GaAs QW as a function of diffusion length for different Nitrogen-bonding configurations ($N\text{-}In_0Ga_4$ (□), $N\text{-}In_1Ga_3$ (○), $N\text{-}In_2Ga_2$ (△), $N\text{-}In_3Ga_1$ (▼), and $N\text{-}In_4Ga_0$ (◊)).

5.3.2 Genetic algorithm

A genetic algorithm (GA) is a search procedure based on population genetics with excellent capability without prior information about the nature of the problem (Khreis 2005). Implementation of GA involves five basic steps: population initialization, population evaluation, selection of parent chromosomes, crossover and mutation, and finally replacing parents with offspring. Simulation stops when the repeating process does not show improvement according to the pre-set criteria.

We use GA to fit the PL peak energy variation as a function of annealing time, with the combined blueshift due to interdiffusion and short range order. An exponential function is introduced to profile the rearrangement rate of the Nitrogen-bonding configuration

$$\Delta E_{SRO} = \Delta E_0(T_{ann})\left(1 - e^{-\left(t_{ann}/\tau(T_{ann})\right)}\right) \tag{5-2}$$

where ΔE_{SRO} is the blueshift due to SRO as function of annealing time, ΔE_0 is the maximum contribution to blueshift by SRO at a particular annealing temperature (T_{ann}), and τ is an annealing-temperature-dependent time constant which controls the reorganization rate of Nitrogen-bonding configuration. When $t_{ann} = 2.303\ \tau$, the blueshift due to SRO reaches 90% of ΔE_0.

In the employed GA approach four parameters, {Ea, D_0, ΔE_0, and τ}, have been selected for the optimization that forms a chromosome. The first generation is randomly generated within the initial solution space with population size, 24 chromosomes. The initial solution space was set chosen to be, $0 \leq \tau \leq 150$, $0 \leq \Delta E_0 \leq 30$, based on our results in previous section 5.2. However, for different annealing temperatures we had different values of ΔE_0 and τ making the chromosome size larger. The generated population is evaluated and ranked based on fitness function, given by

$$e = \sum_{T_{ann}} \sum_{t_{ann}} [E_{PL} - \Delta E_{SRO} - f(L_D)]^2 \tag{5-3}$$

where, E_{PL} is the measured blueshift in PL energy and $f(L_D)$ is the blueshift due to interdiffusion corresponding to diffusion length L_D. $f(L_D)$ is calculated by solving the Schrödinger equation. Schrödinger equation was solved at 100 intermediate points for diffusion lengths, $0 \leq L_D \leq 4$ nm. During optimization $f(L_D)$ was calculated from these pre-calculated values, using interpolation.

The third step of the GA approach involves the selection of parent chromosomes based on fitness functions. Chromosomes with smaller fitness functions are considered fit (close to solution) and unacceptable chromosomes are discarded. Surviving chromosomes are paired for mating and crossover operation is described by combination procedure.

$$child_1 = \begin{cases} E_a & = & r\,E_{a1} + (1-r)\,E_{a2} \\ D_0 & = & r\,D_{01} + (1-r)\,D_{02} \\ \Delta E_{SRO} & = & r\Delta E_{SRO1} + (1-r)\Delta E_{SRO2} \\ \tau & = & r\,\tau_1 + (1-r)\,\tau_2 \end{cases} \qquad child_2 = \begin{cases} E_a & = & (1-r)\,E_{a1} + r\,E_{a2} \\ D_0 & = & (1-r) r\,D_{01} + r\,D_{02} \\ \Delta E_{SRO} & = & (1-r)\Delta E_{SRO1} + r\Delta E_{SRO2} \\ \tau & = & (1-r)\,\tau_1 + r\,\tau_2 \end{cases}$$

where $\{Ea_1, D_{01}, \Delta E_{SRO1}, \tau_1\}$ and $\{Ea_2, D_{02}, \Delta E_{SRO2}, \tau_2\}$ are two surviving chromosomes, r is a weighted operator (a random number, $r \in (0, 1)$). After mutation surviving chromosomes are evaluated and ranked based on fitness functions and genetic operator is repeated until termination condition is satisfied, i.e., 2000 future generations of chromosomes do not show any improvement within the order of 10^{-6} in the fitness functions value. The chromosome with smaller fitness function value, i.e., least square errors is adapted as a final solution.

This procedure was repeated 20 times to check the accuracy and consistency of the simulation. The best fit values were obtained by refining the individual upper and lower limits and relocating in the vicinity of their individual solution space with wide enough range (±20 for τ and ±10 for ΔE_0).

GA based approach has also shown excellent accuracy in determining pre-factor and activation energy for the diffusion coefficients at different temperatures without a need for an Arrhenius plot (Khreis 2005). Moreover, results obtained using a GA search procedure ensures self-consistency in the fitting data across our annealing temperature range, 680 – 800 ^{o}C.

5.3.3 Results and discussion

Figure 5-5 shows the calculated $E_{e1\text{-}Hh1}$ transition energies for the 8-nm $Ga_{0.628}In_{0.372}N_{0.015}As_{0.985}$ / GaAs QW with different N-Ga_mIn_{4-m} configurations.

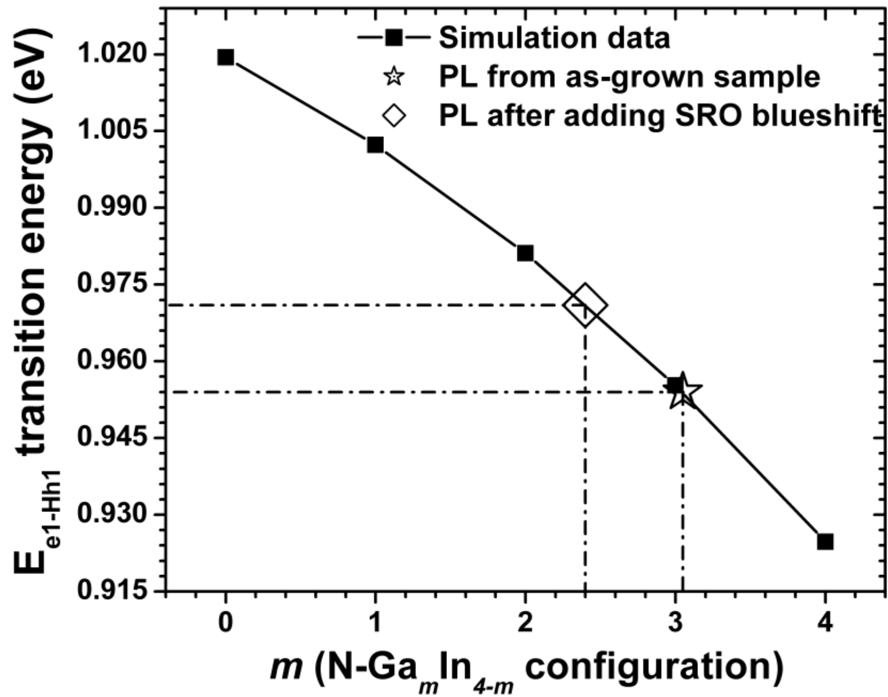

Figure 5-5: Transition energy, Ee1-Hh1, of an 8-nm $Ga_{0.628}In_{0.372}N_{0.015}As_{0.985}$ / GaAs QW as a function of Nitrogen-bonding configuration.

Measured PL peak energy from the as-grown sample (shown as star in Figure 5-5) is close to the calculated transition energy for N-Ga_3In_1 phase. This indicates that the as-grown GaInNAs QW has N-Ga_3In_1 phase. MBE growth of GaInNAs is carried out under non-equilibrium conditions where bonding energy favors the atomic arrangement with Ga-N bonds instead of In-N bonds (Alt 2001). Thus we assume the SRO configuration of GaInNAs QW before the GaAs cap layer growth was N-Ga_4In_0. GaAs cap layer grown on GaInNAs QW had an inherent self-annealing effect due to the higher growths temperature for GaAs than that of GaInNAs (Pessa 2003; Hugues 2007). The blueshift due to self-annealing is 29.3 meV, which is

obtained by comparing the PL peak energy from the as-grown sample and the calculated E_{e1-Hh1} for N-Ga_4In_0 phase. This value is supposed to be more accurate compared to the one determined earlier using linear model which was without the consideration of N-bonding configurations.

During the post-growth annealing process two effects, the SRO and Gallium/Indium interdiffusion, contribute to the blueshift in the PL emission wavelength. Significant role of local strain effect has been reported during the thermal annealing, which changes Nitrogen-bonding configuration from Gallium-rich to Indium-rich environment causing blueshift in bandgap (Kurtz 2001; Chauveau 2004). Rearrangement rate of Nitrogen-bonding configuration is affected by the supplied thermal energy showing faster blueshift for higher annealing temperature. On the other hand, the Gallium/Indium atoms interdiffusion decreases the Indium composition in the QW thus causing blueshift in transition energy.

Since the diffusion lengths for these samples are shorter than 2 nm, under the annealing conditions studied (Liu 2006), thus using the result from Figure 5-4 we can separate the SRO and interdiffusion in analyzing the PL blueshifts in our experiments, i.e., the resultant PL blueshift will be the sum of the two individual blueshifts. Figure 5-6 shows the PL peak energy variation as a function of annealing time at the annealing temperatures 680, 700, 750 and 800 ^{0}C, respectively. The GA based fittings, which simultaneously take into account all the T_{ann} and t_{ann} studied, are shown as the black solid curves for the overall PL transition energies. Also shown in Figure 5-6 are the separated simulation curves of SRO (dashed lines) and interdiffusion (dotted lines) induced transition energies in PL emissions. The sums of interdiffusion and SRO blueshift curves make the GA fitting curves. We can see from Figure 5-6 that interdiffusion induced blueshift increases with the annealing time for T_{ann} = 700, 750, and 800 ^{o}C. Besides, the higher

the T_{ann}, the larger is the interdiffusion induced blueshift (for the same t_{ann}). For T_{ann} = 680 °C, interdiffusion is negligible and the main contribution for blueshift comes from SRO, in agreement with the other experimental reports (Hugues 2007). From the SRO curves we can see that the SRO induced blueshift is dominant when t_{ann} is short. At long t_{ann} the SRO effect is negligible while interdiffusion induced blueshift dominates.

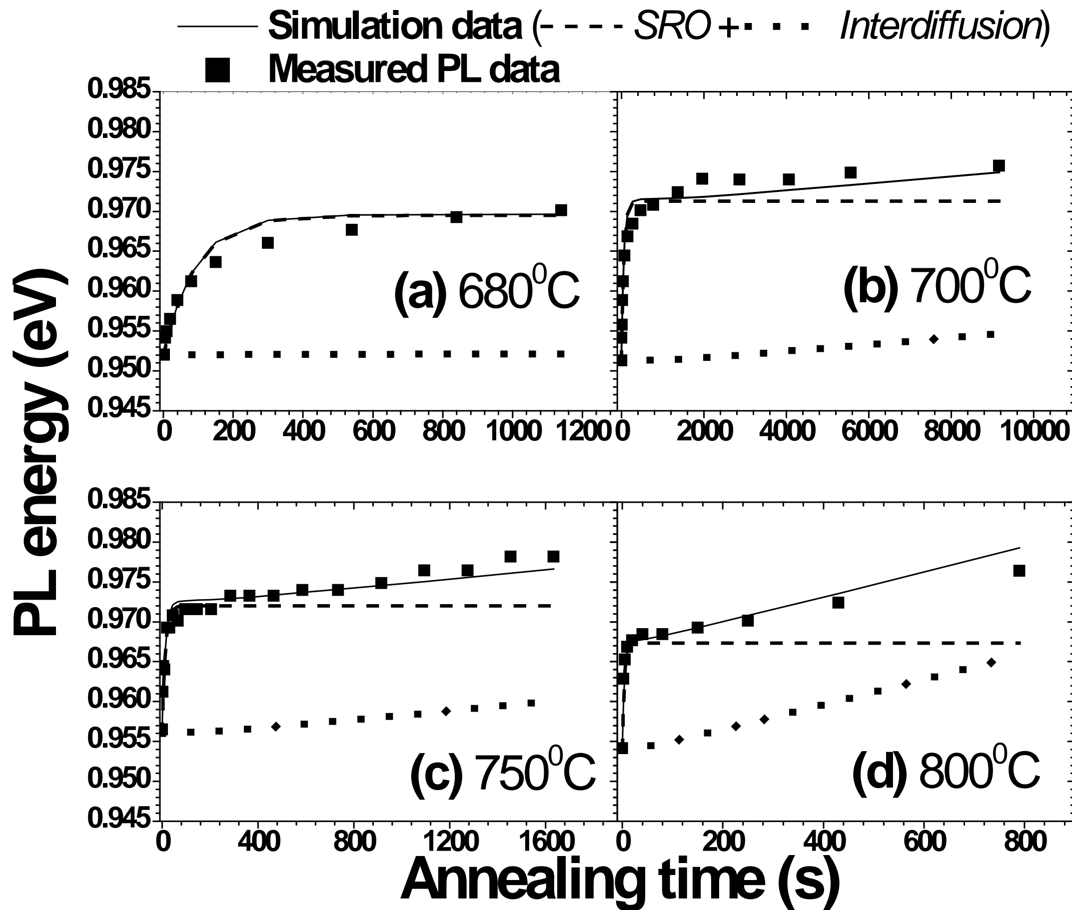

Figure 5-6: Photoluminescence peak energy as a function of annealing time, with annealing performed at (a) 680 °C, (b) 700 °C, (c) 750 °C, and (d) 800 °C. The solid lines are best fits over calculated transition energies with blueshifts due to interdiffusion (dotted lines) and SRO (dashed lines).

The activation energy for interdiffusion obtained by the GA method is E_a = 3.196 eV. This value is close to the E_a = 3.25 eV obtained from the simple linear fitting model, as discussed earlier, for the same experimental data. However, the difference in these two values can be

explained as follows. As all the annealing temperatures are considered together in the GA based fitting the parameters determined will have inherent self-consistency. GA method also removes the ambiguity faced by the linear model in identifying the linear region, where it ignores any further contribution to blueshift by SRO.

The parameters, ΔE_0 and time constant τ, obtained from the SRO simulation are listed in Table 5-2. The average ΔE_0 caused by post growth annealing in our experimental temperature range is about 17 meV which is smaller than the calculated change in $E_{e1\text{-}Hh1}$, 26 meV, for the Nitrogen nearest neighbor configuration changes from N-Ga_3In_1 (as in as-grown sample) to N-Ga_2In_2 (see Figure 5-5). The smaller ΔE_0 implies that annealing at 680-800 ^{0}C results in an N-bonding with the coexistence of N-Ga_3In_1 and N-Ga_2In_2, shown as the open diamond in Figure 5-5. This is in close agreement with the results reported by Kudraweic *et al.* (Kudrawiec 2004).

Table 5-2: The best fitting values of ΔE_{SRO} and τ for different annealing temperatures

Annealing	ΔE_{SRO} (eV)	
Temperature (^{o}C)	ΔE_0	τ (seconds)
680	17.50±0.57	91.65±7.66
700	20.10±0.88	59.62±5.74
750	16.02±0.47	12.62±1.02
800	13.36±0.57	3.80±0.23

It is interesting to note that ΔE_0 first increases with T_{ann} and then decrease when T_{ann} is further increased. At the highest T_{ann} studied (800 ^{0}C) ΔE_{SRO} is the lowest. This is probably due to higher diffusion coefficient, which inhibits short range order as there is less probability of getting Indium rich environment, i.e., more Indium atoms have diffused out of the quantum well. This explanation is supported by other research reports that Indium is the diffusing species, while Nitrogen atoms do not diffuse and they remain within the quantum well (Liu 2006[2]).

We also note that the time constant τ for SRO induced change in PL energy decreases with annealing temperature, varying from 91 sec for 680 ^{0}C to 3.8 sec for 800 ^{0}C. Figure 5-7 shows the Arrhenius plot of 1/τ versus 1/kT. From the Arrhenius plot, we can estimate that the activation energy for the SRO rearrangement is 2.37 eV. Comparing with the activation energy for interdiffusion, 3.196 eV, the smaller activation energy of SRO rearrangement supports the conclusion that the SRO mechanism is dominant at low annealing temperature and at the early stage of the annealing process.

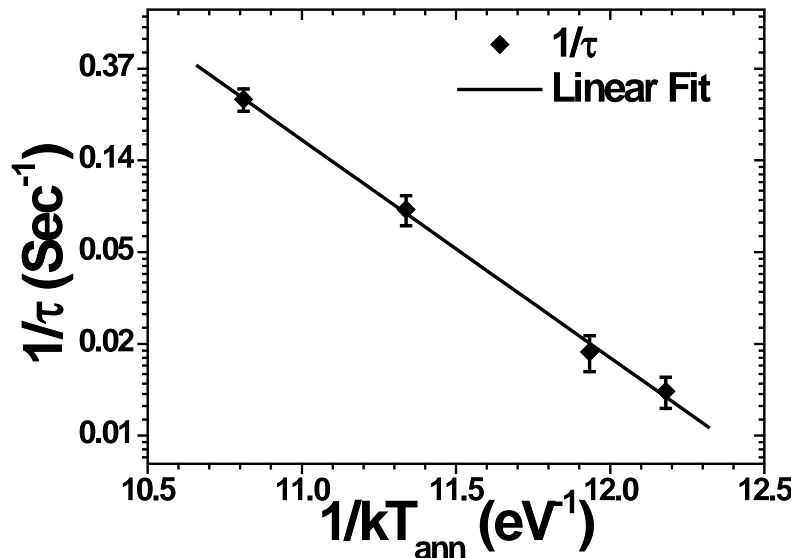

Figure 5-7: An Arrhenius plot of GaInNAs/GaAs SRO time constants (τ) for temperature range between 680 – 800 ^{0}C.

5.4 Conclusion

In conclusion, we have studied the thermal annealing induced PL blueshift from an 8-nm $Ga_{0.628}In_{0.372}N_{0.015}As_{0.985}$ / GaAs QW. The PL peak energy as a function of annealing time duration in the temperature range of 680 – 800 ^{0}C have been analyzed using a linear model and a genetic algorithm based fitting. The comparison of the two models shows that linear model is a good first step in estimating the effect of SRO and interdiffusion but the GA based approach offers more insight into the two phenomena. Results based on our theoretical calculations show

that the PL blueshift due to interdiffusion is linear with annealing time and independent of Nitrogen-bonding configuration when the diffusion length is less than 2 nm. Our calculations suggest the N-Ga_3In_1 bonding configuration in the as-grown QW sample. Post-growth thermal annealing changes the configuration to a mixture of N-Ga_3In_1 and N-Ga_2In_2. The activation energy characterized for SRO rearrangement of the N-bonding configurations is 2.38 eV which is smaller than that for the diffusion process. This result implies that SRO should be the dominant mechanism that induces PL blueshift at lower annealing temperatures and at the beginning of the annealing process.

Chapter 6: Conclusion and Future Work

6.1 Conclusions

In conclusion, we have investigated the effect of Indium segregation and thermal annealing on optical properties of MBE grown GaInNAs/GaAs QWs for their emission at 1.3 and 1.55 µm wavelength.

After realizing that the inclusion of Nitrogen tends to enhance Indium segregation, we presented a (primitive) kinetic model to explain the phenomenon of Indium segregation in GaInNAs/GaAs QW. This kinetic model, based on Indium/Gallium exchange mechanism, has been modified to incorporate the effect of Nitrogen and explain the observed change in Indium segregation length with Nitrogen composition. However, for practical purposes we needed to know the effect of Indium segregation on the optical properties of the QW. For this purpose, we studied the effect of Indium segregation on bandstructure and optical transition energies for 1.3 and 1.55 µm emission wavelengths. It was concluded that only the segregation efficiencies that are larger than 0.6 have significant effect on transition energy. To further consider a more realistic situation, we adopted experimentally measured data for Indium and Nitrogen compositions in the QW to calculate the optical gain spectra of the GaInNAs/GaAs QW. Using the 10-band **k·p** model and many body optical gain model, the effect of composition disorder (Indium segregation and non-uniform Nitrogen profile) on the subband dispersion and optical gain spectra of GaInNAs/GaAs QWs was analyzed.

After studying the as-grown GaInNAs/GaAs QW structure, we studied the photoluminescence blueshift resulting from rapid thermal annealing, which is performed to improve the optical and crystalline quality of GaInNAs material by overcoming the crystal defects arising from plasma damage or interstitial incorporation of Nitrogen. The undesirable blueshift resulting from annealing was studied and explained in terms of two responsible mechanisms: rearrangement of local N-bonding configurations and Gallium/Indium atom interdiffusion across the QW/barrier interface. Using an original approach based on a genetic algorithm, individual contributions from both the mechanisms were calculated. The activation energies for SRO and interdiffusion were estimated to be 2.3 eV and 3.25 eV respectively, indicating the important role played by SRO at low temperature and at the beginning of annealing process.

6.2 Suggested future work

In this work, we have presented a kinetic model to incorporate the effect of Nitrogen on Indium segregation in GaInNAs/GaAs QWs. However, this model is a preliminary work based on few data points. This model can be improved by collecting more experimental data at various growth temperatures, growth rate, III/V flux ratio and Nitrogen compositions. Kinetic modeling can also be performed for different interfaces such as GaInAs/GaAs, GaInNAs/GaAs, GaNAs/GaAs, GaInAs/GaNAs, and GaInNAs/GaNAs. We can also look into alternative theories such as rate equation model to further explore the mechanism of Indium segregation.

We have performed an optical gain spectrum calculation using a 10-band **k·p** model and many body optical gain model. This comprehensive model can be used to calculate the characteristic of a complete laser structure made from dilute nitride materials. Also, we would

like to explore the photoluminescence blueshift in an alternative QW structure with a spacer layer, such as GaNAs strain compensation layer, to look into the origin of interdiffusion and comparison of underlying mechanism for N-bonding reconfiguration.

We have not explored the critical thickness in this work, which would be an interesting topic. Although inclusion of Nitrogen reduces the strain, plasma damage and interstitial incorporation significantly damage the quality of as-grown GaInNAs layer. It would be interesting to look into the real impact of Nitrogen on critical thickness of dilute nitride layers.

Appendix A: Material Parameters

	GaAs	InAs	GaN	InN
Lattice constant a_0 (Å)	5.6533	6.0583	4.46	5.02
Elastic constant C_{11} (Gpa)	119	83.29	296	184
Elastic constant C_{12} (Gpa)	5.38	4.526	15.4	11.6
Effective mass m_c (M_0)	0.0632	0.0213	0.13	0.14
Effective mass m_{HH} (M_0)	0.5	0.517	0.806	0.8
Effective mass m_{LH} (M_0)	0.088	0.024	0.205	0.19
Bandgap E_g (eV)	1.424	0.354	3.1	0.756
dE_g/dP ($\times 10^{-6}$ eV/bar)	11.3	10.2	32.0	22.0
Shear deformation potential b (eV)	-1.7	-1.8	-2.67	-2.67
Deformation potential constant a_c(eV)	-7.17	-5.08	-6.17	-2.65
Deformation potential constant a_v(eV)	1.16	1.00	0.69	0.7
Spin orbit split-off potential Δ_{SO}(eV)	0.34	0.41	0.017	0.005

References

Ager III J. W., and Walukiewicz W., "Current status of research and development of III–N–V semiconductor alloys," *Semiconductor Science and Technology* **17**, 741 (2002)

Agrawal G. P., "Fiber-Optic Communication Systems," John Wiley & Sons (1997)

Alt H. Ch., Egorov A. Yu., Riechert H., Wiedemann B., Meyer J. D., Michelmann R. W., and Bethge K., "Local vibrational mode absorption of Nitrogen in GaAsN and InGaAsN layers grown by molecular beam epitaxy," *Physica B: Condensed Matter* **302-303**, 282 (2001)

Ashley T., Burke T.M., Pryce G.J., Adams A.R., Andreev A., Murdin B.N., O'Reilly E. P., and Pidgeon C.R., “$InSb_{1-x}N_x$ growth and devices,” *Solid-State Electronics* **47**, 387-394 (2003)

Asplund C., Sundgren P., and Hammar M., “Optimization of MOVPE-grown GaInNAs/GaAs quantum wells for 1.3-µm laser applications,” Proceedings of the 14th Indium Phosphide and Related Materials Conference, Stockholm, Sweden, p. 619 (2002)

Bardeen J., "An Improved Calculation of the Energies of Metallic Li and Na," *Journal of Chemical Physics* **6**, 367 (1938)

Bell T. E., "Alfred Yi Cho," *IEEE Spectrum* **31**, 70 (1994)

Bendaniel D. J., and Duke C. B., "Space-Charge Effects on Electron Tunneling," *Physical Review* **152**, 683 (1966)

References

Bhat R., Caneau C., Salamanca-Riba L., Bi W., and Tu C., "Growth of GaAsN/GaAs, GaInAsN/GaAs and GaInAsN/GaAs quantum wells by low-pressure organometallic chemical vapor deposition," *Journal of Crystal Growth* **195**, 427 (1998)

Bourret-Courchesne E., Ye Q., Peters D.W., Arnold J., Ahrned M., Irvine S.J.C., Kanjolaia R., Smith L.M., and Rushworth S.A., “Pyrolysis of dimethylhydrazine and its co-pyrolysis with triethylGallium,” *Journal of Crystal Growth* 217, 47 (2000)

Brewer P. D., Chow D. H., and Miles R. H., "Atomic antimony for molecular beam epitaxy of high quality III-V semiconductor alloys," *Journal of Vacuum Science & Technology B* **14**, 2335 (1996)

Buyanova I. A., Chen W. M., and Tu C. W., "Defects in dilute nitrides," *Journal of Physics: Condensed Matter* **16**, S3027 (2004)

Chadwick G. A., and Smith D. A., “Grain boundary structure and properties," Academic, London (1975)

Chalker P. R., Bullough T. J., Gass M., Thomas S., and Joyce T. B., "The microstructural influence of Nitrogen incorporation in dilute nitride semiconductors," *Journal of Physics: Condensed Matter* **16**, S3161 (2004)

Chan M. C. Y., Surya C., and Wai P. K. A., "The effects of interdiffusion on the subbands in $Ga_xIn_{1-x}N_{0.04}As_{0.96}$/GaAs quantum well for 1.3 and 1.55 μm operation wavelengths," *Journal of Applied Physics* **90**, 197 (2001)

References

Chan M. C. Y., Surya C., and Wai P. K. A., "Optical gain of interdiffused GaInNAs/GaAs quantum wells," *Applied Physics A: Materials Science & Processing* **75**, 573 (2002)

Chauveau J. M., Trampert A., Ploog K. H., and Tournie E., "Nanoscale analysis of the In and N spatial redistributions upon annealing of GaInNAs quantum wells," *Applied Physics Letters* **84**, 2503 (2004)

Cho A. Y., "Recent developments in molecular beam epitaxy (MBE)," *Journal of Vacuum Science and Technology* **16**, 275 (1979)

Cho A. Y., "Growth of III-V semiconductors by molecular beam epitaxy and their properties," *Thin Solid Films* **100**, 291 (1983)

Chow W. W., and Koch S. W., "Semiconductor—Laser Fundamentals," Springer, Germany (1999)

Chuang S. L., "Physics of Optoelectronic devices," Wiley-Interscience publication, New York (1995)

Dang Y. X., Fan W. J., Ng S. T., Yoon,S. F., and Zhang D. H., "Study of interdiffusion in GaInNAs/GaAs quantum well structure emitting at 1.3 μm by eight-band **k•p** method," *Journal of Applied Physics* **97**, 103718 (2005)

David R. Goff, Kimberly S. Hansen, Michelle K. Stull, “Fiber optic video transmission: the complete guide,” Focal Press, (2003)

References

Dehaese O., Wallart X., and Mollot F., "Kinetic model of element III segregation during molecular beam epitaxy of III-III'-V semiconductor compounds," *Applied Physics Letters* **66**, 52 (1995)

Dixit V., Liu H. F., and Xiang N., "Analyzing the thermal-annealing-induced photoluminescence blueshifts for GaInNAs/GaAs quantum wells: a genetic algorithm based approach," *Journal of Physics D: Applied Physics* **41**, 115103 (2008)

Duboz J.-Y., Gupta J. A., Wasilewski Z. R., Ramsey J., Williams R. L., Aers G. C., Riel B. J., and Sproule G. I., "Band-gap energy of $In_xGa_{1-x}N_yAs_{1-y}$ as a function of N content," *Physical Review B (Condensed Matter and Materials Physics)* **66**, 085313 (2002)

Dudley J. J., Babic D. I., Mirin R., Yang L., Miller B. I., Ram R. J., Reynolds T., Hu E. L., and Bowers J. E., "Low threshold, wafer fused long wavelength vertical cavity lasers," *Applied Physics Letters* **64**, 1463 (1994)

Egorov A.Yu., Odonobludov V.A., Mamutin V.V., Zhukov A.E., Tsatsu'nikov A.F., Kryzhanovskaya N.V., Ustinov V.M., Hong Y.G., Tu C.W., “Valence band structure of GaAsN compounds and band-edge lineup in GaAs/GaAsN/InGaAs heterostructures,” *Journal of crystal growth* **251**, 417 (2003)

Eppenga R., Schuurmans M. F. H., and Colak S., "New **k•p** theory for GaAs/Ga1-xA1xAs-type quantum wells," *Physical Review B* **36**, 1554 (1987)

Fan W. J., Yoon S. F., Ng T. K., Wang S. Z., Loke W. K., Liu R., and Wee A., "Comparison of Nitrogen compositions in the as-grown GaN_xAs_{1-x} on GaAs measured by high-resolution

X-ray diffraction and secondary-ion mass spectroscopy," *Applied Physics Letters* **80**, 4136 (2002)

Fischer M., Reinhardt M., and Forchel A, "GaInAsN/GaAs laser diodes operating at 1.52 µm," *Electronics Letters* **36**, 1208 (2000)

Friedman D.J., Geisz J.F., Kurtz S.R. and Olson J.M., “1-eV solar cells with GalnNAs active layer,” *Journal of Crystal Growth* **195**, 409 (1998)

Friedman D.J., Geisz J.F., Kurtz S.R., Olson J.M., and Reedy R., "Nonlinear dependence of N incorporation on In content in GaInNAs," *Journal of Crystal Growth* **195**, 438 (1998[1])

Gambin V., “Long Wavelength Luminescence from GaInNAsSb on GaAs,” PhD thesis, Stanford University (2002)

Gillin W. P., Dunstan D. J., Homewood K. P., Howard L. K., and Sealy B. J., "Interdiffusion in InGaAs/GaAs quantum well structures as a function of depth," *Journal of Applied Physics* **73**, 3782 (1993)

Gokhale M.R., Wei J., Wang H. and Forrests S.R., “Growth and characterization of small band gap (~0. 6 eV) InGaAsN layers on InP,” *Applied Physics Letters* **74**, 1287 (1999)

Goldstein L., Fortin C., Starck C., Plais A., Jacquet J., Boucart J., Rocher A., and Poussou C., "GaAlAs/GaAs metamorphic Bragg mirror for long wavelength VCSELs," *Electronics Letters* **34**, 268 (1998)

Ha W., Gambin V., Wistey M., Yuen H., Kim S. and Harris J., Jr., “Long wavelength GaInNAs(Sb) lasers on GaAs,” *Proceedings of the 14th Indium Phosphide and Related Materials Conference,* May 12-16, Stockholm, Sweden, ISSN 1092-8669, pp. 381 (2002)

Hal P.N., Chert W.M., Buyanova I.A., Xin H.P. and Tu C.W., “Direct determination of electron effective mass in GaNAs/GaAs quantum wells,” *Applied Physics Letters* **77**, 1843 (2000)

Harmand J.C., Ungaro G., Largeau L. and LeRoux G., “Comparison of Nitrogen incorporation in molecular-beam epitaxy of GaAsN, GaInAsN, and GaAsSbN,” *Applied Physics Letters* **77**, 2482 (2000)

Harris J.S., Jr., “Tunable long-wavelength vertical-cavity lasers: the engine of next generation optical networks,” *IEEE Journal of Selected Topics in Quantum Electronics* **6**, 1145 (2000)

Harris J.S., Jr., “GalnNAs long-wavelength lasers: progress and challenges,” *Semiconductor Science and Technology* **17**, 880 (2002)

Harrison W. A., "Electronic Structure and the Properties of Solids," Dover Publications, New York (1989)

Henini M., “Dilute nitride semiconductors,” Elsevier, Oxford (2005)

Hetterich M., Dawson M. D., Egorov A. Yu., Bernklau D., and Riechert H., "Electronic states and band alignment in GalnNAs/GaAs quantum-well structures with low Nitrogen content," *Applied Physics Letters* **76**, 1030 (2000)

References

Ho I.-H., and Stringfellow G. B., "Solubility of Nitrogen in binary III-V systems," *Journal of Crystal Growth* **178**, 1 (1997)

Hofmann M. R., Gerhardt N., Wagner A. M., Ellmers C., Höhnsdorf F., Koch J., Stolz W., Koch S. W., Rühle W. W., Hader J., Moloney J. V., O'Reilly E. P., Borchert B., Egorov A. Y., Riechert H., Schneider H. C., and Chow W. W., "Emission dynamics and optical gain of 1.3-μm (GaIn)(NAs)/GaAs lasers," *IEEE Journal of Quantum Electronics* **38**, 213 (2002)

Hohnsdorf F., Koch J., Agert C., and Stolz, W., "Investigations of (GaIn)(NAs) bulk layers and (GaIn)(NAs) multiple quantum well structures grown using tertiarybutylarsine (TBAs) and 1,1-dimethylhydrazine (UDMHy)," *Journal of Crystal Growth* **195**, 391 (1998)

Hovel H. J., "Scanned photoluminescence of semiconductors," *Semiconductor Science and Technology* **7**, A1 (1992)

http://www.jpix.ad.jp/en/techncal/traffic.html

Huang Y. C., Wang J. S., Lu Y. K., Wu C. T., Huang S. L., and Cheng W. H., " Fabrication of 300-nm Cr-doped Fibers Using Fiber Drawing with Pressure Control," Proceedings of the optical Fiber communication/National Fiber Optic Engineers Conference, San Diego, USA, p. 1 (2008)

Hugues M., Damilano B., Chauveau J.-M., Duboz J.-Y., and Massies J., "Blue-shift mechanisms in annealed (Ga,In)(N,As)/GaAs quantum wells," *Physical Review B* **75**, 045313 (2007)

References

Illek S., Borchert B., Ebbinghaus G., Egorov A.Yu. and Riechert H., "GaInNAs/GaAs multiple quantum-wells (MQWs) for 1.3 μm laserapplications," *Proceedings of the 12th InP and Related Material Conference,* Williamsburg, USA, p. 537 (2000)

Inahama S., Akiyama T., Nakamura K., and Ito T., "Theoretical Investigation of Indium Surface Segregation in InGaN Thin Films," *e-Journal of Surface Science and Nanotechnology* **3**, 503 (2005)

Jensen J. R., Hvam J. M., and Langbein W., "Optical properties of InAlGaAs quantum wells: Influence of segregation and band bowing," *Journal of Applied Physics* **86**, 2584 (1999)

Johnson A.D., Bennett R.H., Newey J., Pryce G.J., Williams G.M., Burke T.M., Jones J.C. and Keir A.M., "InN_xSb_{1-x} light emitting diodes grown by MBE," *Materials Research Society Symposium Proceedings* **607**, 28 (2000)

Kaminov Ivan P., and Tingye Li, "Optical fiber telecommunications IV", Academic Press, New York (2002)

Khee N. T., Fatt Y. S., and Weijun F., "Laser Power and Temperature Dependent Photoluminescence Characteristics of Annealed GaInNAs/GaAs Quantum Well," *Proceeding of Materials Research Symposium* **799**, Z5.15 (2003)

Khreis O. M., and Al-Kofahi I. S., "Accurate and direct determination of interdiffusion parameters, a genetic algorithm approach," *Semiconductor Science and Technology* **20**, 320 (2005)

References

Kim K., Lambrecht Walter R. L., and Segall B., "Elastic constants and related properties of tetrahedrally bonded BN, AlN, GaN, and InN," *Physical Review B* **53**, 16310 (1996)

Kim K., and Zunger A., "Spatial Correlations in GaInAsN Alloys and their Effects on Band-Gap Enhancement and Electron Localization," *Physical Review Letters* **86**, 2609 (2001)

Kirchner V., Heinke H., Birkle U., Einfeldt S., Hommel D., Selke H., and Ryder P. L., "Ion-induced crystal damage during plasma-assisted MBE growth of GaN layers," *Physical Review B* **58**, 15749 (1998)

Kitatani T., Kondow M., and Tanaka T., "Effects of thermal annealing procedure and a strained intermediate layer on a highly-strained GaInNAs/GaAs double-quantum-well structure," *Journal of Crystal Growth* **221**, 491 (2000)

Klar P. J., Gruning H., Koch J., Schafer S., Volz K., Stolz W., Heimbrodt W., Saadi A. M. Kamal, Lindsay A., and O'Reilly E. P., "(Ga, In)(N, As)-fine structure of the band gap due to nearest-neighbor configurations of the isovalent Nitrogen," *Physical Review B* **64**, 121203 (2001)

Kondow M., Uomi K., Niwa A., Kitatani T., Watahiki S. and Yazawa Y., “GaInNAs: a novel material for long-wavelength-range laser diodes with excellent high-temperature performance,” *Japanese Journal of Applied Physics* **35**, 1273 (1996)

Kondow M., Nakatsuka S., Kitatani T, Yazawa Y., and Okai M., "Room-Temperature Pulsed Operation of GaInNAs Laser Diodes with Excellent High-Temperature Performance," *Japanese Journal of Applied Physics* **35**, 5711 (1996[1])

References

Kondow M., Nakatsuka S., Kitatani T., Yazawa Y. and Okai M., “Room-temperature continuous-wave operation of GaInNAs/GaAs laser diode,” *Electronics Letters* **32**, 2244 (1996[2])

Kondow M., Uomi K., Kitatani T., Watahiki S. and Yazawa Y., “Extremely large N content (up to 10%) in GaNAs grown by gas-source molecular beam epitaxy,” *Journal of Crystal Growth* **164**, 175 (1996[3])

Kondow M., Kitatani T., Nakatsuka S., Larson M. C., Nakahara K., Yazawa Y., Okai M., and Uomi K., "GaInNAs: a novel material for long-wavelength semiconductor lasers," *IEEE Journal of selected Topics in Quantum Electronics* **3**, 719 (1997)

Kondow M., Kitatani T., Shirakata S., "Annealing in GaInNAs system," *Journal of Physics: condensed matter* **16**, S3229 (2004)

Kudrawiec R., Pavelescu E.-M., Wagner J., Sek G., Misiewicz J., Dumitrescu M., Konttinen J., Gheorghiu A., and Pessa M., "Photoreflectance evidence of multiple band gaps in dilute GaInNAs layers lattice-matched to GaAs," *Journal of Applied Physics* **96**, 2576 (2004)

Kurtz S., Webb J., Gedvilas L., Friedman D., Geisz J., Olson J., King R., Joslin D., and Karam N., "Structural changes during annealing of GaInAsN," *Applied Physics Letters* **78**, 748 (2001)

Kurtz S., Reedy R., Barber G.D., Geisz J.F., Friedman D.J., McMahon W.E., and Olson J.M.,” Incorporation of Nitrogen into GaAsN grown by MOCVD using different precursors,” *Journal of Crystal Growth* **234**, 318 (2002)

References

Krispin P., Spruytte S.G., Harris J.S., and Ploog K.H., "Origin and annealing of deep level defects in p-type GaAs/Ga(As,N)/GaAs heterostructures grown by molecular beam epitaxy", *Journal of Applied Physics* **89**, 6294 (2001)

Kvietkova J., Hetterich M., Egorov A.Yu., Riechert H., Leibiger G., and Gottschalch V., "Temperature and polarization dependence of the optical gain and optically pumped lasing in GaInNAs/GaAs MQW structures," *Proceedings of 27th International conference on physics of Semiconductors (ICPS-27)* **772**, p. 1542 (2005)

LaPierre R.R., Robinson B.J. and Thompson D.A., "Group V incorporation in InGaAsP grown on InP by gas source molecular beam epitaxy," *Journal of Applied Physics* **79**, 3021 (1996)

Lee R.T., and Stringfellow G.B., "Pyrolysis of 1,1 dimethylhydrazine for OMVPE growth," *Journal of Electronic Materials* **28**, 963 (1999).

Li G., Chua S. J., Xu S. J., Wang X. C., Helmy A., Ke Mao-Long, and Marsh J. H., "Silica capping for $Al_{0.3}Ga_{0.7}As/GaAs$ and $In_{0.2}Ga_{0.8}As/GaAs$ quantum well intermixing," *Applied Physics Letters* **73**, 3393 (1998)

Li E. H., "Material parameters of InGaAsP and InAlGaAs systems for use in quantum well structures at low and room temperatures," *Physica E: Low-dimensional Systems and Nanostructures* 5, 215 (2000)

References

Li W., Jouhti T., Peng C. S., Konttinen J., Laukkanen P., Pavelescu E.-M., and Pessa M., "Low-threshold-current 1.32-µm GaInNAs/GaAs single-quantum-well lasers grown by molecular-beam epitaxy," *Applied Physics Letters* **79**, 3386 (2001)

Li W., Pessa M., and Likonen J., "Lattice parameter in GaNAs epilayers on GaAs: Deviation from Vegard's law," *Applied Physics Letters* **78**, 2864 (2001[1])

Li L.H., Pan Z., Zhang W., Wang X.Y., and Wu R.H., “Quality improvement of GalnNAs/GaAs quantum wells grown by plasma-assisted molecular beam epitaxy” *Journal of Crystal Growth* **227-228**, 527 (2001[2])

Liu H. F., Dixit V., and Xiang N., "Anneal-induced interdiffusion in 1.3-µm GaInNAs/GaAs quantum well structures grown by molecular-beam epitaxy," *Journal of Applied Physics* **99**, 013503 (2006)

Liu H. F., Dixit V., and Xiang N., "Effect of Indium segregation on optical and structural properties of GaInNAs/GaAs quantum wells at emission wavelength of 1.3-µm," *Journal of Applied Physics* **100**, 083518 (2006[1])

Liu H. F., and Xiang N., "Influence of GaNAs strain-compensation layers on the optical properties of GaIn(N)As/GaAs quantum wells upon annealing," *Journal of Applied Physics* **99**, 053508 (2006[2])

Liu H. F., Xiang N., and Chua S. J., "Annealing behavior of N-bonding configurations in $GaN_{0.023}As_{0.977}$ ternary alloy grown on GaAs (0 0 1) substrate by molecular beam epitaxy," *Journal of Crystal Growth* **290**, 24 (2006[3])

Liu H. F., Xiang N., and Chua S. J., "Influence of N incorporation on In content in GaInNAs/GaNAs quantum wells grown by plasma-assisted molecular beam epitaxy," *Applied Physics Letters* **89**, 071905 (2006[4])

Liu H. Y., Hopkinson M., Navaretti P., Gutierrez M., Ng J. S., and David J. P. R., "Improving optical properties of 1.55-μm GaInNAs/GaAs multiple quantum wells with Ga(In)NAs barrier and space layer," *Applied Physics Letters* **83**, 4951 (2003)

Luna E., Trampert A., Pavelescu E.-M., and Pessa M., "Nitrogen-enhanced Indium segregation in (Ga,In)(N,As)/GaAs multiple quantum wells grown by molecular-beam epitaxy," *New Journal of Physics* **9**, 405 (2007)

Martini S., Quivy A. A., Da Silva C. F., and Leite J. R., "Real-time determination of the segregation strength of Indium atoms in InGaAs layers grown by molecular-beam epitaxy," *Applied Physics Letters* **81**, 2863 (2002)

Martini S., Quivy A. A., Da Silva M. J., Lamas T. E., Da Silva C. F., Leite J. R., and Abramof E., "Ex-situ investigation of Indium segregation in InGaAs/GaAs quantum wells using high-resolution X-ray diffraction," *Journal of Applied Physics* **94**, 7050 (2003)

Massies J., Turco F., Saletes A., and Contour J. P., "Experimental evidence of difference in surface and bulk compositions of $Al_xGa_{1-x}As$, $Al_xIn_{1-x}As$ and $Ga_xIn_{1-x}As$ epitaxial layers grown by molecular beam epitaxy," *Journal of Crystal Growth* **80**, 307 (1987)

Meney A. T., O'Reilly E. P., and Adams A. R., "Optical gain in wide bandgap GaN quantum well lasers," *Semiconductor Science and Technology* **11**, 897 (1996)

References

Mesrine M., Massies J., Deparis C., Grandjean N., and Vanelle E., "Real-time investigation of In surface segregation in chemical beam epitaxy of $In_{0.5}Ga_{0.5}P$ on GaAs (001)," *Applied Physics Letters* **68**, 3579 (1996)

Miller D. L., Bose S. S., and Sullivan G. J., "Design and operation of a valved solid-source As_2 oven for molecular beam epitaxy," *Journal of Vacuum Science & Technology B* **8**, 311 (1990)

Minch J., Park S. H., Keating T., and Chuang S. L., "Theory and experiment of $In_{1-x}Ga_xAs_yP_{1-y}$ and $In_{1-x-y}Ga_xAl_yAs$ long-wavelength strained quantum-well lasers," *IEEE Journal of Quantum Electronics,* **35**, 771 (1999)

Moison J. M., Guille C., Houzay F., Barthe F., and Van Rompay M., "Surface segregation of third-column atoms in group III-V arsenide compounds: Ternary alloys and heterostructures," *Physical Review B* **40**, 6149 (1989)

Moore K. J., Duggan G., Dawson P., and Foxon C. T., "Short-period GaAs-AlAs superlattices: Optical properties and electronic structure," *Physical Review B* **38**, 5535 (1988)

Muraki K., Fukatsu S., Shiraki Y., and Ito R., "Surface segregation of In atoms during molecular beam epitaxy and its influence on the energy levels in InGaAs/GaAs quantum wells," *Applied Physics Letters* **61**, 557 (1992)

Ng T. K., Djie H. S., Yoon S. F., and Mei T., "Thermally induced diffusion in GaInNAs/GaAs and GaInAs/GaAs quantum wells grown by solid source molecular beam epitaxy," *Journal of Applied Physics* **97**, 013506 (2005)

References

Ng S. T., Fan W. J., Dang Y. X., and Yoon S. F., "Comparison of electronic band structure and optical transparency conditions of $In_xGa_{1-x}As_{1-y}N_y$/GaAs quantum wells calculated by 10-band, 8-band, and 6-band **k•p** models," *Physical Review B* **72**, 115341 (2005[1])

Nomuraa K., Yamadab T., Iguchib Y., Takagishib S., and Nakayamaa M., "Photoluminescence properties of localized states caused by Nitrogen alloying in a GaInNAs/GaAs single quantum well," *Journal of Luminescence* **112**, 146 (2005)

Ougazzaden A., Le Bellego Y., Rao E.V.K., Leprince L., and Patriarche G.," Metal organic vapor phase epitaxy growth of GaAsN on GaAs using dimethylhydrazine and tertiarybutylarsine," *Applied Physics Letters* **70**, 2861 (1997)

Pan Z., Li L. H., Zhang W., Lin Y. W., Wu R. H., and Ge W., "Effect of rapid thermal annealing on GaInNAs/GaAs quantum wells grown by plasma-assisted molecular-beam epitaxy," *Applied Physics Letters* **77**, 1280 (2000)

Pan Z., Li L. H., Zhang W., Lin Y. W., and Wu R. H., "Kinetic modeling of N incorporation in GaInNAs growth by plasma-assisted molecular-beam epitaxy," *Applied Physics Letters* **77**, 214 (2000[1])

Pan Z., Li L.H., Zhang W., Wang X.Y., Lin Y., and Wu R.H., "Growth and characterization of GaInNAs/GaAs by plasma-assisted molecular beam epitaxy," *Journal of Crystal Growth* **227-228**, 516 (2001)

Park S. H., Kim H. M., Jeong W. G., and Choe B. D., "Differential gain of strained InGaAs/InGaAsP quantum-well lasers lattice matched to GaAs," *Journal of Applied Physics* **79**, 2157 (1996)

Park S. H., and Chuang S. L., "Comparison of zinc-blende and wurtzite GaN semiconductors with spontaneous polarization and piezoelectric field effects," *Journal of Applied Physics* **87**, 353 (2000)

Park S. H., “Many-body optical gain of GaInNAs/GaAs strained quantum-well lasers,” *Applied Physics Letters* **85**, 890 (2004)

Parker E. H. C., "The Technology and Physics of Molecular Beam Epitaxy," Springer (1985)

Patriarche G., Jeannes F., Oudar J.-L., and Glas F., "Structure of the GaAs/InP interface obtained by direct wafer bonding optimised for surface emitting optical devices," *Journal of Applied Physics* **82**, 4892 (1997)

Pavelescu E.-M., Peng C. S., Jouhti T., Konttinen J., Li W., Pessa M., Dumitrescu M., and Spanulescu S., "Effects of insertion of strain-mediating layers on luminescence properties of 1.3-µm GaInNAs/GaNAs/GaAs quantum-well structures," *Applied Physics Letters* **80**, 3054 (2002)

Pavelescu E.-M., Jouhti T., Dumitrescu M., Klar P. J., Karirinne S., Fedorenko Y., and Pessa M., "Growth-temperature-dependent (self-)annealing-induced blueshift of photoluminescence from 1.3-µm GaInNAs/GaAs quantum wells," *Applied Physics Letters* **83**, 1497 (2003)

Pessa M., Peng C. S., Jouhti T., Pavelescu E.-M., Li W., Karirinne S., Liu H., and Okhotnikov O., "Towards high-performance nitride lasers at 1.3-μm and beyond," *IEE Proceedings - Optoelectronics* **150**, 12 (2003)

Phillips J. C., and Kleinman L., "New Method for Calculating Wave Functions in Crystals and Molecules," *Physical Review* **116**, 287 (1959)

Phillips J.C., Alper A.M., Margrave J.L., and Nowick A.S., “Bonds and Bands in Semiconductors,” Academic Press, New York (1973)

Pikus G. E. and Bir G. L., "Symmetry and Strain-Induced Effects in Semiconductors," Wiley, New York (1974)

Rao E. V. K., Ougazzaden A., Le Bellogo Y., and Juhel M., " Optical properties of low band gap $GaAs_{(1-x)}N_x$ layers: Infleunce of post-growth treatments," *Applied Physics Letter* **72**, 1409 (1998)

Riechert H., Ramakrishnan A., and Steinle G., "Development of InGaAsN-based 1.3 μm VCSELs," *Semiconductor Science and Technology* **17**, 892 (2002)

Rubini S., Bais G., Cristofoli A., Piccin M., Duca R., Nacci C., Modesti S., Carlino E., Martelli F., Franciosi A., Bisognin G., De Salvador D., Schiavuta P., Berti M., and Drigo A. V., "Nitrogen-induced hindering of In incorporation in InGaAsN," *Applied Physics Letters* **88**, 141923 (2006)

Rüdiger Paschotta, Encyclopedia of Laser Physics and Technology (available: http://www.rp-photonics.com/optical_fiber_communications.html), Wiley VCH (2008)

Ryang W., "High resolution X-ray diffraction characterization of semiconductor structures," *Materials Science and Engineering: R: Reports* **13**, 1-56 (1994)

Sato S., and Satoh S., "1.21 μm Continuous-Wave Operation of Highly Strained GaInAs Quantum Well Lasers on GaAs Substrates," *Japanese Journal of Applied Physics* **38**, L990 (1999)

Schowalter M., Rosenauer A., and Gerthsen D., "Influence of surface segregation on the optical properties of semiconductor quantum wells," *Applied Physics Letters* **88**, 111906 (2006)

Schubert E. Fred, "Light Emitting Diodes," Cambridge University Press, (2006)

Seitz F., "The Modern Theory of Solids," McGraw Hill, New York (1940)

Serries D., Geppert T., Ganser P., Kohler K., and Wagner J., “High In content GaInAsN on InP: composition dependent band gap energy and luminescence properties,” *Proceedings of the 14th InP and Related Materials Conference,* Stockholm Sweden, pp. 389 (2002)

Shan W., "Band Anticrossing in III-N-V Alloys," *physica status solidi (b)* **223**, 75 (2001)

Slater J. C., and Koster G. F., "Simplified LCAO Method for the Periodic Potential Problem," *Physical Review* **94**, 1498 (1954)

Spruytte S.G., Coldren C.W., Marshall A.F., and Harris J.S.,“MBE growth of nitridearsenide materials for long-wavelength optoelectronics”, *Proceedings of Materials Research Society Spring Meeting.* **W8**.4 (1999)

Spruytte S.G., Larson M.C., Wampler W., Coldren C.W., Krispin P., Petersen H.E., Picraux S., Ploog K., and Harris J.S., "Nitrogen incorporation in group III-nitride-arsenide materials grown by elemental source molecular beam epitaxy," *Journal of Crystal Growth* **227-228**, 506 (2001)

Spruytte S.G., "MBE Growth of nitride-arsenides for long-wavelength optoelectronics," PhD Thesis, Stanford University, April (2001[1])

Strite S., Chandrasekhar D., Smith D. J., Sariel J., Chen H., Teraguchi N., and Morkoc H., "Structural properties of InN films grown on GaAs substrates: observation of the zinc-blende polytpe," *Journal of Crystal Growth* **127**, 204 (1993)

Tajima M., Ibuka S., Aga H., and Abe T., "Characterization of bond and etch-back silicon-on-insulator wafers by photoluminescence under ultraviolet excitation," *Applied Physics Letters* **70**, 231 (1997)

Tomic S., O'Reilly E. P., Fehse R., Sweeney S. J., Adams A. R., Andreev A. D., Choulis S. A., Hosea T. J. C., and Riechert H., "Theoretical and experimental analysis of 1.3-µm InGaAsN/GaAs lasers," *IEEE Journal of Selected Topics in Quantum Electronics* **9**, 1228 (2003)

Tournie E., Pinault M.-A., Vezian S., Massies J., and Tottereau O., "Long wavelength GaInNAs/GaAs quantum-well heterostructures grown by solid-source molecular-beam epitaxy," *Applied Physics Letters* **77**, 2189 (2000)

Tournie E., Pinault M.-A., and Guzman A., "Mechanisms affecting the photoluminescence spectra of GaInNAs after post-growth annealing," *Applied Physics Letters* **80**, 4148 (2002)

Uchiyama S., and Kashiwa S., "GaInAsP/InP SBH surface emitting laser with Si/Al_2O_3 mirror," *Electronics Letters* **31**, 1449 (1995)

Ustinov V. M., and Zhukov A. E., "GaAs-based long-wavelength lasers," *Semiconductor Science and Technology* **15**, R41 (2000)

Van de Walle C. G., "Band lineups and deformation potentials in the model-solid theory," *Physical Review B* **39**, 1871 (1989)

Vegard L., Die Konstiution der Mischkristalle und die Raumfüllung der Atome,Zeitschrift für Physik, 5, 17 (1921)

Viswanathan T., “Telecommunication Switching Systems and Networks,” Prentice Hall of India Pvt. Ltd., (2004)

Volz K., Gambin V., Ha W., Wistey M.A., Yuen H., Bank S., and Harris, J.S., “The role of Sb in the MBE growth of (GaIn)(NAsSb),” *Journal of Crystal Growth* **251**, 360 (2003)

Vurgaftman I., Meyer J. R., and Ram-Mohan L. R., "Band parameters for III--V compound semiconductors and their alloys," *Journal of Applied Physics* **89**, 5815 (2001)

Vurgaftman I., and Meyer J. R., "Band parameters for Nitrogen-containing semiconductors," *Journal of Applied Physics* **94**, 3675 (2003)

Wang S. Z., Yoon S. F., Ng T. K., Loke W. K., and Fan W. J., "Molecular beam epitaxial growth of $GaAs_{1-X}N_X$ with dispersive Nitrogen source," *Journal of Crystal Growth* **242**, 87 (2002)

Wee S. F., Chai M. K., Homewood K. P., and Gillin W. P., "The activation energy for GaAs/AlGaAs interdiffusion," *Journal of Applied Physics* **82**, 4842 (1997)

Welty R.J., Xin H., Tu C.W., and Asbeck P.M., "Minority carrier transport properties of GaInNAs heterojunction bipolar transistors with 2% Nitrogen," *Journal of Applied Physics* **95**, 327 (2004)

Weyers M., Sato M., and Ando H., "Red shift of Photoluminescence and Absorption in Dilute GaAsN Alloy Layers," *Japanese Journal of Applied Physics* **31**, 853 (1992)

Wistey M.A., Bank S.R., Yuen H.B., and Harris J.S., "Real-time measurement of GaInNAs Nitrogen plasma ion flux", *North American MBE Conference*, Keystone, CO, pp. 2-9. (2003)

Wright A. F., "Elastic properties of zinc-blende and wurtzite AlN, GaN, and InN," *Journal of Applied Physics* **82**, 2833 (1997)

Yamaguchi K., Okada T., and Hiwatashi F., "Analysis of Indium surface segregation in molecular beam epitaxy of InGaAs/GaAs quantum wells," *Applied Surface Science* **117-118**, 700 (1997)

Yuen W., Li G. S., and Chang-Hasnain C. J., "Multiple-wavelength VCSEL arrays on patterned substrates", *Vertical-Cavity Lasers, Technologies for a global Information Infrastructure,*

WDM components Technology, Advanced Semiconductor Lasers and Applications, Gallium Nitride Materials, Processing, and Devices conference, Montreal, Que., Canada (1997)

Yuen H.B., Bank S.R., Wistey M.A., Bae H.P., Moto A., and Harris J.S. "Effects of N_2 flow on GaInNAs grown by a RF plasma cell in MBE", *MRS Spring Conference*, San Francisco, CA (2004)

Yuen H.B., Bank S. R., Wistey M.A., Moto A., and Harris J.S., "Comparison of GaNAsSb and GaNAs as quantum well barriers for GaInNAsSb optoelectronic devices operating at 1.3-1.55 µm," *Journal of Applied Physics* **96**, 6375 (2004[1])

Zhao H., Adolfsson G., Wang S. M., Sadeghi M., and Larsson A., "Very low threshold current density 1.29 µm GaInNAs triple quantum well lasers grown by MBE," *Electronics Letters* **44**, 416 (2008)

Zhou W., Uesugi K., and Suemune I., "1.55-µm emission from GaInNAs with Indium-induced increase of N concentration," *Applied Physics Letters* **83**, 1992 (2003)